

THESIS FOR THE DEGREE OF DOCTOR OF PHILOSOPHY

On Control of Grid-connected Voltage Source Converters

Mitigation of Voltage Dips and Subsynchronous Resonances

MASSIMO BONGIORNO



Department of Energy and Environment
CHALMERS UNIVERSITY OF TECHNOLOGY
Göteborg, Sweden 2007

On Control of Grid-connected Voltage Source Converters
Mitigation of Voltage Dips and Subsynchronous Resonances
MASSIMO BONGIORNO
ISBN 978-91-7291-985-3

© MASSIMO BONGIORNO, 2007.

Doktorsavhandlingar vid Chalmers Tekniska Högskola
Ny serie nr. 2666
ISSN 0346-718X

Department of Energy and Environment
Chalmers University of Technology
SE-412 96 Göteborg
Sweden
Telephone +46 (0)31-772 1000

Chalmers Bibliotek, Reproservice
Göteborg, Sweden 2007

To Moghi

On Control of Grid-connected Voltage Source Converters
Mitigation of Voltage Dips and Subsynchronous Resonances
MASSIMO BONGIORNO
Department of Energy and Environment
Chalmers University of Technology

Abstract

Custom Power and Flexible AC Transmission Systems (FACTS) denote the application of power electronics in distribution and transmission networks, respectively.

Custom Power is the application of power electronics to improve the quality of power distribution for sensitive industrial plants. Power electronic converters connected in shunt or series with the grid and equipped with energy storage can provide protection of sensitive processes against voltage disturbances, like short interruptions and voltage dips. The first part of this thesis focuses on the control of Voltage Source Converter (VSC) connected in series or in shunt with the grid for mitigation of voltage dips. In both configurations, the core of the control system is the current controller. Here, the deadbeat current controller for grid-connected VSC is presented and analyzed in detail. The controller includes time delay compensation and reference voltage limitation with feedback, to improve the current control during overmodulation. Improvements for proper control of the current under unbalanced conditions of the grid voltage are investigated. For use in a series-connected VSC, the deadbeat current controller is completed with an outer voltage loop, thus realizing a cascade controller that is presented and analyzed in detail. Further, a similar cascade controller for voltage dip compensation using shunt-connected VSC is investigated. In both configurations, it is shown that control of the negative-sequence component of the injected voltage is needed for a proper mitigation of unbalanced voltage dips. FACTS is instead the application of power electronics at transmission level. In transmission systems, other control objectives are more important than voltage dip compensation. Controllable series compensation is used for e.g. power flow control, stability improvement, and damping of power oscillations. Traditional non-controllable series compensation based on series capacitors can create problems due to unwanted resonance with the rest of the power system. A specific problem that often arises in conjunction with series capacitors is subsynchronous resonance (SSR), which can lead to damage of generator shafts. In this case, a series-connected VSC, similar to the one used for the distribution system and here called Static Synchronous Series Compensator (SSSC), could be used as a dedicated device for SSR mitigation. In the second part of this thesis, a novel control strategy for the SSSC for SSR mitigation is investigated and analyzed. It is shown that, by injecting only a subsynchronous voltage into the power system, SSR mitigation is achieved by increasing the network damping only at those frequencies that are of danger for the generator-shaft system. This will allow to provide SSR damping with very low voltage injection, leading to a cost-effective alternative to the existing solutions.

Index Terms: Power Electronics, Voltage Source Converter (VSC), Power Quality, Current Controller, Voltage Dip (Sag), Subsynchronous Resonance (SSR).

Acknowledgements

My deepest gratitude goes to my supervisors, Dr. Jan Svensson and Prof. Lennart Ängquist, for their technical guidance, patience and support.

I would like to thank Prof. Gustaf Olsson, for being my examiner and for many fruitful discussions. Moreover, I would like to thank Prof. Jaap Daalder and Prof. Math Bollen, for being the examiners in the beginning of this project.

I would like to sincerely thank Dr. Ambra Sannino, for being my supervisor in the first part of this project and for her friendship and continuous help also during the second part of this work.

Many thanks go to Prof. Torbjörn Thiringer, for the support and help he has given me throughout my stay at Chalmers.

This work has been carried out within Elektra Project 3693 and has been funded by Energimyndigheten, ELFORSK, ABB Corporate Research, ABB Power Technologies FACTS, AREVA T&D and Banverket.

My acknowledgments go to the members of the reference group for the first part of this project: Evert Agneholm (Gothia Power), Per Halvarsson (ABB Power Technologies FACTS), Ricardo Tenorio (ABB Power Technologies FACTS), Helge Seljeseth (SINTEF Energy Research), for beneficial inputs and considerations.

Thanks to all employees of ABB Power Technologies FACTS, particularly Peter Lundberg, Åke Petersson and Falah Hosini, for the nice and friendly atmosphere during my staying at ABB.

Many thanks go to all my fellow Ph.D. students, who have assisted me in several and different ways. In particular, I want to thank Stefan Lundberg, Andreas Petersson, Rolf Ottersten and Oskar Wallmark, for all help and nice discussions.

I further would like to thank Prof. Lennart Harnefors, for interesting discussions and valuable suggestions.

I am grateful to Robert Karlsson for his help and patience when assisting me in the laboratory. Many thanks to Magnus Ellsén, Jan-Olov Lantto and Valborg Ekman.

Thanks to Dr. Remus Teodorescu from Aalborg University, for help with the DSpace system, and Dr. Paul Thøgersen from Danfoss for providing the converter used for the laboratory setup.

I would also like to thank my parents, Mario and Flora, and my sister Giuliana for their support.

Last, but surely not least, I would like to thank my wife Monica, for her love, encouragement and understanding.

Massimo Bongiorno
Gothenburg, Sweden
August, 2007

Contents

Abstract	v
Acknowledgements	vii
Contents	ix
1 Introduction	1
1.1 Background	1
1.1.1 Use of power electronics in distribution systems	1
1.1.2 Use of power electronics in transmission systems	2
1.2 Aim and outline of the thesis	3
1.3 Main contributions of the thesis	3
1.4 Scientific production	4
Part I - Control of VSC for Voltage Dip Mitigation	7
2 Voltage Dips and Mitigation Methods	9
2.1 Introduction	9
2.2 Voltage dips	9
2.3 Voltage dip mitigation	12
2.3.1 Power system improvement	12
2.3.2 Load immunity	13
2.3.3 Mitigation devices	14
2.4 Conclusions	20
3 Vector Current-controller for Grid-connected VSC	21
3.1 Introduction	21
3.2 Vector Current-controller (VCC)	21
3.2.1 Proportional controller	24
3.2.2 Proportional-integral controller	25
3.3 Vector Current-controller type 1 (VCC1)	26
3.3.1 One-sample delay compensation	27
3.3.2 Saturation and integrator anti-windup	29
3.4 Stability analysis	32
3.4.1 Accurate knowledge of model parameters	33

Contents

3.4.2	Inaccurate knowledge of model parameters	35
3.5	Experimental results	39
3.6	Conclusions	40
4	Control of Series-connected VSC for Voltage Dip Mitigation	41
4.1	Introduction	41
4.2	Layout of the SSC	41
4.3	Dual Vector-controller type 1 (DVC1)	43
4.3.1	Voltage controller	44
4.3.2	Stability analysis	47
4.4	Experimental results	50
4.5	Conclusions	53
5	Control of Shunt-connected VSC for Voltage Dip Mitigation	55
5.1	Introduction	55
5.2	Voltage dip mitigation using reactive power injection	56
5.3	Shunt-connected VSC using LCL-filter	57
5.4	Conclusions	61
	Part II - Control of VSC for Subsynchronous Resonance Mitigation	63
6	Analysis of Subsynchronous Resonance in Power Systems	65
6.1	Introduction	65
6.2	Definition and classification of SSR	66
6.3	Synchronous generator model	68
6.4	Transmission network model	71
6.5	Combined generator and network equations	72
6.6	Turbine-generator shaft model	73
6.6.1	Modal analysis	75
6.7	Combined mechanical-electrical equations	78
6.8	SSR due to torsional interaction effect	80
6.9	Frequency scanning analysis	84
6.10	Countermeasures to the SSR problem	88
6.10.1	Power system design improvements	88
6.10.2	Turbine-generator design improvements	89
6.10.3	Use of auxiliary devices	89
6.11	Conclusions	92
7	Control of Static Synchronous Series Compensator for SSR Mitigation	93
7.1	Introduction	93
7.2	Classical control of SSSC for SSR mitigation	93
7.3	Proposed control strategy for SSSC for SSR mitigation	95
7.4	Subsynchronous controller	96
7.4.1	Subsynchronous components Estimation Algorithm (EA)	96
7.4.2	Subsynchronous Current Controller (SSCC)	99

7.5	Stability analysis	101
7.6	Analysis of SSR due to TI effect	103
7.6.1	Eigenvalue analysis	103
7.6.2	Frequency scanning analysis	103
7.7	Evaluation of voltage requirements for SSSC for SSR mitigation	105
7.8	Dc-link voltage controller (DCVC)	108
7.9	SSSC control structure	110
7.10	Simulation results	111
7.11	Conclusions	117
8	Conclusions and Future Work	119
8.1	Conclusions	119
8.2	Future work	121
	References	123
A	Transformations for Three-phase Systems	131
A.1	Transformation of three-phase quantities into vectors	131
A.2	Transformation between fixed and rotating coordinate systems	132
A.3	Voltage vectors for unsymmetrical three-phase systems	133
B	Benchmark Models for SSR Studies	135
B.1	IEEE First Benchmark Model (FBM)	135
B.2	IEEE Second Benchmark Model (SBM)	135
C	Selected Publications	139

Contents

Chapter 1

Introduction

This chapter describes the background of the thesis. The aim and the outline as well as the fundamental scientific contributions of the thesis are presented. Finally, a list of the scientific production is given.

1.1 Background

During several decades, power electronic based solutions have been successfully applied both at the distribution and transmission levels to improve the utilization of the power system. The actual trend is to use power electronic converters connected both in series and shunt with the main grid. Although similar configurations are used both at the distribution and transmission levels, the applications and, thus, the adopted control strategies vary depending on the considered voltage level. The following is a brief description of possible applications of power electronic devices for distribution and transmission systems.

1.1.1 Use of power electronics in distribution systems

At distribution level, power electronic controllers, also called *Custom Power Devices*, have been introduced to improve the quality of power distribution in industrial plants [31], in response to growing demand from industries reporting production stops due to voltage disturbances, like short interruptions and voltage dips. These power quality phenomena are normally caused by clearing short-circuit faults in the power system and, despite their very short duration, can impact the operation of low-power electronic devices, motor contactors, and drive systems [18, 19, 46, 74]. Among the most sensitive industries are paper mills [15], semiconductor facilities [21] and other industries with fully automated production, where the sensitivity of electronic equipment to voltage disturbances can cause the stoppage of the whole facility. To solve this problem, several different custom power devices have been proposed, many of which have at their heart a Voltage Source Converter (VSC) connected to the grid. One way to mitigate voltage dips is to install a VSC connected to the grid in shunt. This device, also known under

the name of distribution STATCOM or D-STATCOM, injects a controllable current in the grid. By injecting a current in the point of connection, a shunt-connected VSC can boost the voltage in that point during a voltage dip. Alternatively, voltage dips can be mitigated by injecting a voltage into the grid with a series-connected VSC. The injected voltage adds up to the supply voltage during the dip in order to restore the load voltage to its pre-fault value. This device, known also with its commercial name of Dynamic Voltage Restorer (DVR), has been applied successfully in a number of facilities around the world, e.g. a yarn manufacture [80], semiconductor plants [20, 79], a food plant in Australia [78], and a large paper mill in Scotland [15]. Both in shunt and series configuration, the VSC must be controlled properly to inject the necessary current (in shunt connection) or voltage (in series connection) into the grid in order to compensate for a voltage dip. Since some sensitive loads can shut down because of a dip that lasts some hundreds of ms, the speed of response of the device is a decisive factor for successful compensation. Moreover, the majority of voltage dips are unbalanced, and therefore another requirement for successful dip compensation is a fast detection of the grid voltage unbalance and a high-performance control of the VSC.

1.1.2 Use of power electronics in transmission systems

At transmission level, instead, power electronic based devices are mainly applied for power flow control and to improve the stability of the power system. Interconnected transmission systems are complex and require careful planning, design and operation. The continuous growth of the electrical power system (especially, of large loads like industrial plants), resulting in growing electric power demand, has put greater emphasis on system operation and control. It is under this scenario that the use of *High Voltage Direct Current* (HVDC) and *Flexible AC Transmission Systems* (FACTS) devices represent both opportunities and challenges for optimum utilization of existing facilities [33, 66]. Furthermore, FACTS devices are used as a countermeasure to dynamical problems such as loss of synchronism, voltage collapse and low frequency power oscillations [33]. As an example, series compensation of long transmission lines can be used to increase the power transfer capability of long transmission lines by improving the angle stability in the system and thyristor controllers (like the Thyristor Controlled Series Capacitor (TCSC)) can provide damping of power oscillations by offering controllable series compensation [49]. However, implementing the series compensation using fixed capacitor banks in systems powered by thermal generating stations might cause a severe problem called subsynchronous resonance (SSR) [25]. This is a resonant condition where the generator-turbine shaft system exchanges energy with the electrical system. Self excitation of oscillations may cause serious stress on the shaft system and in the worst case may lead to breakdown. One way to avoid the risk of SSR is to (at least partially) replace the fixed series capacitor banks with a TCSC. By changing the total reactance of the network seen from the generator terminal at subsynchronous frequencies, the TCSC can provide appropriate damping at subsynchronous frequencies, thus presenting an economical solution to the SSR problem [1]. Alternatively, SSR damping can also be achieved by using a series-connected VSC, addressed to as Static Synchronous Series Compensator (SSSC) [33, 65], similar to the DVR utilized in the distribution network for voltage dip mitigation. The main limitation preventing a widespread application of VSC-based series

compensation is its high cost. However, if used for specific applications such as SSR damping, the rating of the device can be drastically reduced, thus making it cheaper and economically competitive with other existing mitigation devices.

1.2 Aim and outline of the thesis

The thesis is divided into two parts. The first part deals with the problem of voltage dips in the distribution system and possible solutions for their mitigation. The aim of the first part (Chapters 2 to 5) is to improve, analyze and test different control algorithms for VSC, which are suitable for mitigation of unbalanced voltage dips for both series- and shunt-connected configurations of the VSC. Chapter 2 of the thesis gives an overview of voltage dips, of their causes and effects, and of possible mitigation methods. Both in shunt and series configuration, the heart of the control system for the VSC is a current controller, which is presented and analyzed in detail in Chapter 3. The investigated algorithm includes time delay compensation and reference voltage limitation with feedback, to improve the current control during overmodulation. Stability analysis of the resulting control algorithm is included. Furthermore, improvements to the investigated control system to allow a proper control of the VSC current also in case of unbalanced condition of the grid voltage are discussed.

The current controller presented in Chapter 3 is completed with an outer voltage loop for the use in a series-connected configuration, thus realizing the cascade controller presented and analyzed in Chapter 4. Stability analysis of the investigated cascade controller is presented in this chapter.

In Chapter 5, the control system for voltage dip compensation using the shunt-connected VSC is presented and analyzed. A modified configuration including an LCL-filter between the VSC and grid is proposed to improve the system performance, particularly in the presence of a weak grid.

Furthermore, the second part of the thesis deals with the problem of mitigation of subsynchronous resonance in the transmission system. The aim of this part of the thesis is to derive, analyze and simulate a novel control strategy for a SSSC dedicated to SSR mitigation. Chapter 6 gives an overview of the problem of subsynchronous resonance in power systems. Definition and classification of different kinds of SSR are given. Furthermore, in this chapter conditions that might lead to SSR and possible mitigation methods are described. The proposed control strategy for the SSSC is described and analyzed in Chapter 7. Further, in this chapter the proposed approach is compared with the control strategy existing in the literature. Stability analysis together with time-domain simulation results are presented.

Finally, conclusions and suggestions for future work are given in Chapter 8.

1.3 Main contributions of the thesis

In order how they appear in the included papers, the list below summarizes what, in the opinion of the author, are the main contributions presented in this thesis:

Chapter 1. Introduction

- The well-known Delayed Signal Cancellation method for phase-sequence estimation of the measured voltage and current [40] is analyzed in Papers I and II. The influence of a non ideal sampling frequency and of harmonics in the measured signals is investigated. Methods for reduction of the estimation error are proposed.
- It is shown in Chapters 3 and 4 that often the heart of the control system, both for the shunt and the series-connected VSC, is a vector-current controller. In Papers III and IV the dynamic behaviors of three different vector-current controllers are investigated. Although not new, this analysis is meant to be a guideline for the reader to select the most suitable control strategy, depending on the application.
- Papers V and VI deal with the control of series- and shunt-connected VSC for voltage dip mitigation, respectively. Several publications on this topic can be found in the literature and, thus, this is hardly new. The main contributions in this thesis that relate to this topic involve a detailed analysis of the investigated controllers and suggestions to improve their transient performance, in particular in the case of unbalanced voltage dips, which represent the majority of the dips that can occur in the power systems.
- For the second part of this thesis, Paper VII proposes an estimation algorithm for the estimation of subsynchronous components in the measured voltages and currents. Apart from the control point of view, detection of subsynchronous voltages and currents in the power systems is of importance for a proper monitoring and for a timely operation of the protection system, in order to avoid damage in the generator shaft.
- Papers VIII to X show a new control strategy for subsynchronous resonance mitigation using an SSSC dedicated to SSR mitigation. The proposed control strategy is compared with the existing method, showing the advantage of the proposed approach. In particular, it is shown that with the adopted control strategy, SSR mitigation is achieved with very low voltage injection, leading to a reduced voltage rating for the device.

1.4 Scientific production

The publications originating from this Ph.D. project are:

- I. J. Svensson, M. Bongiorno and A. Sannino, "Practical Implementation of Delayed Signal Cancellation Method for Phase Sequence Separation," *IEEE Transactions on Power Delivery*, vol. 22, no. 1, pp. 18-26, Jan. 2007.
- II. M. Bongiorno, J. Svensson and A. Sannino, "Effect of Sampling Frequency and Harmonics on Delay-based Phase-sequence Estimation Method," submitted to *IEEE Transactions on Power Delivery*.

A similar version of this paper appeared in 2006 as:

1.4. Scientific production

J. Svensson, A. Sannino and M. Bongiorno, “Delayed Signal Cancellation Method for Sequence Detection - Effect of Sampling Frequency and Harmonics,” in *Proc. of IEEE Nordic Workshop on Power and Industrial Electronics (NorPIE’06)*.

III. M. Bongiorno, J. Svensson and A. Sannino, “Dynamic Performance of Current Controllers for Grid-connected Voltage Source Converter Under Unbalanced Voltage Conditions,” in *Proc. of IEEE Nordic Workshop on Power and Industrial Electronics (NorPIE’04)*.

IV. M. Bongiorno, J. Svensson and A. Sannino, “Dynamic Performance of Vector Current Controllers for Grid-connected VSC under Voltage Dips,” in *Proc. of 40th Annual IEEE Industry Applications Conference (IAS’05)*, vol. 2, Oct. 2005, pp. 904-909.

V. M. Bongiorno, J. Svensson and A. Sannino, “An Advanced Cascade Controller for Series-connected VSC for Voltage Dip Mitigation,” to appear in *IEEE Transactions on Industry Applications*.

A similar version of this paper appears in *Proc. of 40th Annual IEEE Industry Applications Conference (IAS’05)*, vol. 2, Oct. 2005, pp. 873-880 .

VI. M. Bongiorno and J. Svensson, “Voltage Dip Mitigation using Shunt-connected Voltage Source Converter,” to appear in *IEEE Transactions on Power Electronics*.

A similar version of this paper appears in *Proc. of 37th IEEE Power Electronics Specialists Conference (IEEE PESC’06)*, June 2006, pp.1-7.

VII. M. Bongiorno, J. Svensson and L. Ängquist, “Online Estimation of Subsynchronous Voltage Components in Power Systems,” to appear in *IEEE Transactions on Power Delivery*.

VIII. M. Bongiorno, L. Ängquist and J. Svensson, “A Novel Control Strategy for Subsynchronous Resonance Mitigation Using SSSC,” to appear in *IEEE Transactions on Power Delivery*.

IX. M. Bongiorno, J. Svensson and L. Ängquist, “On Control of Static Series Compensator for SSR Mitigation,” in *Proc. of 38th Annual IEEE Power Electronics Specialists Conference (IEEE PESC’07)*.

X. M. Bongiorno, J. Svensson and L. Ängquist, “Single-phase VSC Based SSSC for Subsynchronous Resonance Damping,” to appear in *IEEE Transactions on Power Delivery*.

The author has also contributed to the following publications (not included in this thesis):

1. M. Bongiorno, A. Sannino and L. Dusonchet, “Cost-Effective Power Quality Improvement for Industrial Plant,” in *Proc. of IEEE Bologna PowerTech 2003*.
2. C. Rong, M. Bongiorno and A. Sannino, “Control of D-STATCOM for Voltage Dip Mitigation,” in *Proc. of International Conference on Future Power Systems (FPS) 2005*.

Chapter 1. Introduction

Finally, the author has contributed to the patent application:

M. Bongiorno, L. Ängquist and J. Svensson, “An Apparatus and a Method for a Power Transmission System,” *PCT (WO) Application, Appl. nr. SE2006/001106*.

Part I - Control of VSC for Voltage Dip Mitigation

In this first part of the thesis, the use of power electronic based devices in the distribution system will be treated. As mentioned earlier in the introduction chapter, the focus will be on control of series- and shunt-connected voltage source converter for voltage dip mitigation.

Chapter 2

Voltage Dips and Mitigation Methods

This chapter presents an overview of the power quality problems and especially of voltage dips. Furthermore, different solutions for voltage dip mitigation, like power system improvements, improvement of the load immunity and installation of mitigation devices are treated.

2.1 Introduction

The utilities' aim is to continuously provide their customers with an ideal sinusoidal voltage waveform, i.e. a voltage with constant magnitude at the required level and with a constant frequency. In case of three-phase operation, the voltages should be symmetric.

Unfortunately, due to power system variations under normal operation and to unavoidable events like short-circuit faults, the supply voltage never complies with the above mentioned requirements. On the other hand, utilities require that the customers draw sinusoidal current from the main supply.

The term "power quality" has arisen trying to clarify duties of utilities and customers versus each other. The interest in power quality has increased in the latest years, especially due to the increased number of electronic devices in industrial plants.

Among the power quality phenomena, voltage dips are generally considered the most severe issue for electronic-based equipments [46]. Definition and classification of voltage dip will be given in the next section.

2.2 Voltage dips

According to IEEE Std.1159-1995 [35], a voltage dip is defined as a decrease between 0.1 to 0.9 pu in the RMS voltage at the power frequency with duration from 0.5 cycles to 1 minute. A voltage dip can be caused by different events that can occur in the power system, like transformer energizing, switching of capacitor banks, starting of large induction motors and short-circuit

faults in the transmission and distribution system. In this thesis, only voltage dips due to short-circuits will be considered.

To quantify the magnitude and the phase of a voltage dip in a radial system due to a three-phase fault, the simplified voltage divider model shown in Fig.2.1 can be used [12]. In this system, two impedances are connected to the point of common coupling (PCC): the grid impedance, denoted with \bar{Z}_g , which includes everything above the PCC, and the fault impedance \bar{Z}_f , which represents the impedance between the fault and the PCC. The load is connected to the PCC through a transformer and its voltage is denoted as \bar{E}_l . The source voltage is denoted by \bar{E}_s . The voltage \bar{E}_g at the PCC during the fault is given by [12]

$$\bar{E}_g = \frac{\bar{Z}_f}{\bar{Z}_f + \bar{Z}_g} \bar{E}_s \quad (2.1)$$

From (2.1) it is possible to observe that the voltage dip magnitude depends on the fault location (since the impedance \bar{Z}_f depends on the distance between the point in the power system where the fault occurs and the PCC) and the grid impedance. Observe that, in the ideal case of infinitely strong grid ($\bar{Z}_g = 0$), the voltage at the PCC will always be constant and independent on the fault location. The argument of the voltage vector \bar{E}_g during the voltage dip, called phase-angle jump, depends on the X/R ratio between the grid and the fault impedance and is given by

$$\psi = \arg(\bar{E}_g) = \arctan\left(\frac{X_f}{R_f}\right) - \arctan\left(\frac{X_g + X_f}{R_g + R_f}\right) \quad (2.2)$$

The duration of the dip is related to the tripping time of the protection device which controls the circuit breaker, denoted as CB in Fig.2.1. When the CB installed in the feeder where the fault occurs clears the fault, the voltage is restored for the rest of the system. This results in very short dips for faults in the transmission system (50-100 ms clearing time to avoid stability problems) and much longer ones for faults in the distribution system, where protections are delayed to ensure selectivity [12].

Often, it is preferable to characterize a voltage dip with the distance between the fault point and the PCC. In this case, the voltage \bar{E}_g during the fault can be expressed as

$$\bar{E}_g = \frac{\lambda e^{j\alpha}}{1 + \lambda e^{j\alpha}} \quad (2.3)$$

where λ denotes the “electrical distance” between the faulted point and the PCC and α , called

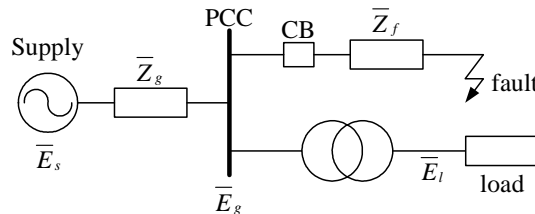


Fig. 2.1 Single-line diagram to display voltage division during voltage dips.

impedance angle, is the angle between grid and fault impedance

$$\alpha = \arctan\left(\frac{X_f}{R_f}\right) - \arctan\left(\frac{X_g}{R_g}\right) \quad (2.4)$$

Typically, the impedance angle α varies between 0° and -60° [12].

An extended analysis of voltage dips and their classification is carried out in [82]. Depending on the type of fault (three-phase, phase-to-phase with or without ground involved, single-phase to ground), the resulting voltage dip at the PCC can be one of six types displayed in Fig.2.2.

The load is usually supplied through a distribution transformer, connected in Δ/Y . The transformer swaps the phases and removes the zero-sequence component because of the delta connection, where no connection to ground exist. This results in a transformation of the dip characteristic as listed in Table.2.1 (right column). This dip classification is further extended in [81], where it is shown that type F is in fact a particular case of type C and D. It can be concluded that voltage dips that affect the load downstream a Δ/Y -transformer can only be of type A, C and D. The voltage dip type A is a drop in voltage in all three phases (balanced dip). The voltage dip type C is characterized by a drop in two phases with the third phase voltage almost undisturbed. Finally, the voltage dip type D is characterized by a larger drop in one phase and smaller drops in the other two phases. However, in some applications, such as control of VSC connected to the grid, it can be preferable to characterize the voltage dip in terms of the remaining positive-sequence voltage and the unbalance, expressed as magnitude of negative-sequence voltage in percentage of the pre-fault voltage [62].

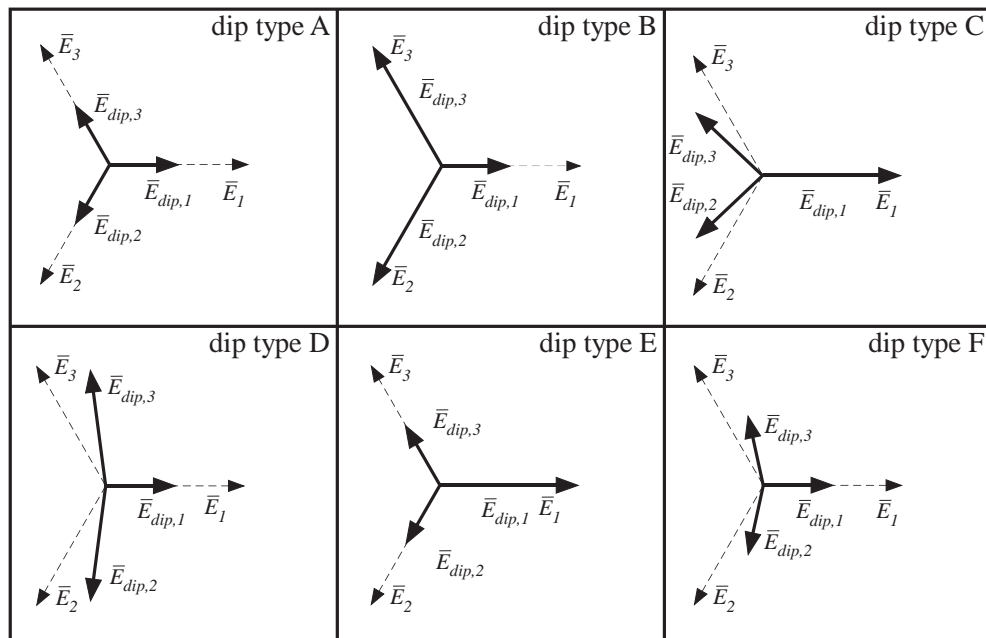


Fig. 2.2 Voltage dip classification “A” to “F”. Phasors of three-phase voltage before (dotted) and during fault (solid) are displayed (from [82]).

TABLE 2.1. VOLTAGE DIP CLASSIFICATION AND PROPAGATION THROUGH Δ/Y -TRANSFORMERS.

Fault	Dip seen at PCC	Dip seen by the load
3-phase fault	type A	type A
1-phase fault	type B	type C
2-phase to ground	type E	type F
phase-to-phase	type C	type D

2.3 Voltage dip mitigation

The main problem related to voltage dips is that they can cause tripping of sensitive industrial equipment, leading to relatively high economical losses. As shown in Fig.2.3, different ways to reduce the number of voltage dips experienced by the load can be adopted [12]. The possibilities are to improve the power system, improve the immunity to voltage deviations of the end-user equipment and finally to use a mitigation device at the user interface. In the following, a brief description of these solutions will be carried out.

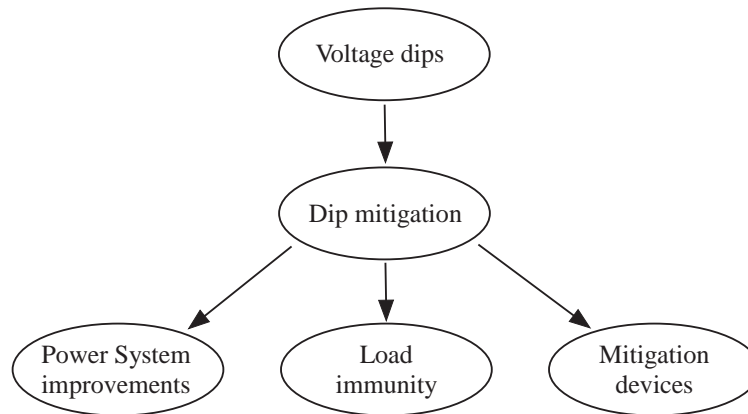


Fig. 2.3 Mitigation methods against voltage dips.

2.3.1 Power system improvement

A way to reduce the number of voltage dips experienced by the load is to improve the reliability of the power system. This can be done in three different ways:

- Improve the network design and operation;
- Reduce the number of faults per year;
- Use faster protection systems.

An extended analysis of these solutions is carried out in [12]; the following is a brief summary.

Improve network design and operation

By improving the power system design, the number and severity of the voltage quality phenomena experienced by the load can be drastically reduced. The mitigation method against short interruptions and voltage dips is mainly the installation of redundant components, like feeders, generators or more substations to feed the bus where the sensitive load is connected. The problem related to this solution is that the costs for these improvements, especially at the transmission level, can be very high and, thus, this solution is not often economically feasible.

Reduce number of faults

Since the majority of voltage dips experienced in the power system are related to short-circuit faults, an obvious way to deal with the problem is to reduce the number of faults. The problem is that, since a fault represents an economical loss not only for the customer but also for the utility (a fault can damage the utility equipment or plant), most of the utilities have already reduced the fault frequency to a minimum. Improvements that reduce the number of faults per year include replacing the overhead lines with underground cables, increasing the insulation level and increasing the maintenance.

Faster protection system

By reducing the fault clearing time, the number of voltage dips experienced by the load will not be affected, but the duration of the dip will be reduced. A possible solution to reduce the clearing time of the fault is to use current-limiting fuses or modern static circuit breakers, which are able to clear the fault within one half-cycle [12]. However, some caution has to be taken when applying these new protection devices in existing distribution systems. If only some of the protective devices are replaced with static breakers (on incoming transformer circuits or feeder circuits, for instance), due to their extremely fast operation it would not be possible to coordinate them with previously existing downstream protective devices. Therefore, if faster fault clearing time is required, the whole system has to be redesigned and all protective devices have to be replaced with faster ones. This would greatly reduce the fault-clearing time. The drawback, of course, of these modifications in the power system is that this will result in an increase of the costs.

2.3.2 Load immunity

An increase of the load immunity against voltage dips can appear as the most suitable solution to avoid load tripping. The tolerance of the equipment is intended as the capability of the device to work properly during voltage variations. In order to evaluate the compatibility between power system and equipment, the so-called voltage-tolerance curve has been introduced in IEEE Std.1346-1998 [36]. This curve, depicted in Fig.2.4, represents the maximum duration, expressed in seconds, for which a piece of equipment can withstand dips of any magnitude (denoted in the figure as $\max \Delta t$) and the maximum dip magnitude, expressed in per unit of the

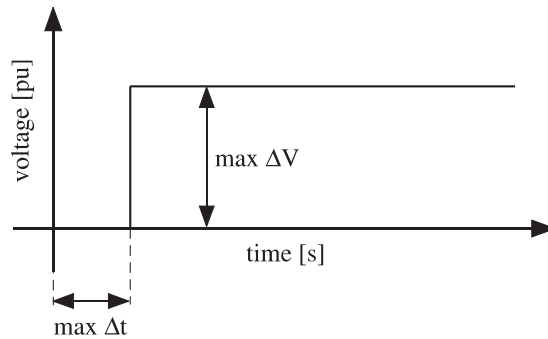


Fig. 2.4 Typical voltage-tolerance curve for sensitive equipment.

rated voltage, that the equipment can withstand regardless the duration of the dip (denoted as $\max \Delta V$). The knee of the curve is defined by the maximum duration and the minimum voltage and represents the tolerance of the equipment.

The main problem related to the immunity of the sensitive loads is that often the customer is not well aware of equipment sensitivity and will find out the problem only after the equipment has been installed. Moreover, since the customer is usually not in direct contact with the manufacturer, it is very hard to acquire information about the immunity of the device or to affect its specifications. Only for large industrial equipment, such as large drive systems, where usually the customer can require certain specification, the immunity of the equipment against power quality phenomena can be decided ad hoc.

2.3.3 Mitigation devices

The most commonly applied method for voltage dip mitigation is the installation of an additional device at the power system interface. The installation of these devices is getting more and more popular among industrial customers due to the fact that it is the only place where the customer has control over the situation. As explained in the previous section, both changes in the supply and changes in the characteristics of the equipment are outside the control of the end-user.

It is possible to divide the mitigation devices in two main groups:

- Passive mitigation devices, based on mature technology devices such as transformers or rotating machines;
- Active mitigation devices, based on power electronics.

Motor-generator sets

Motor-generator sets store energy in a flywheel, as shown in Fig.2.5 [63]. They consist of a motor (can be an induction or a synchronous machine) supplied by the plant power system, a synchronous generator feeding the sensitive load and a flywheel, all connected to a common

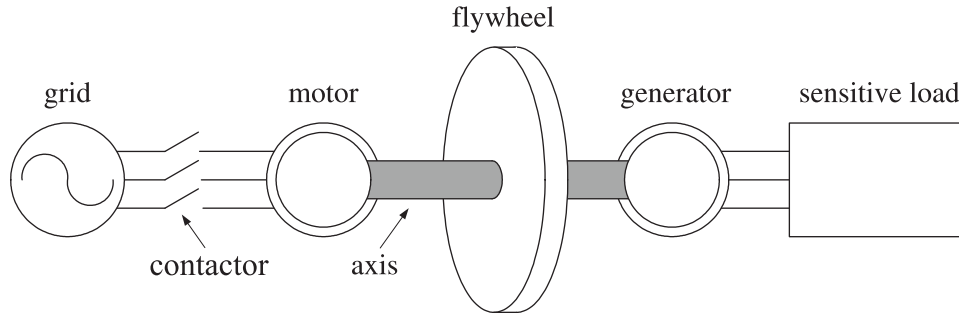


Fig. 2.5 Three-phase diagram of motor-generator set with flywheel for voltage dip mitigation.

mechanical axis. The rotational energy stored in the flywheel can be used to perform steady-state voltage regulation and to support the voltage during disturbances. In case of voltage dips, the system can be disconnected from the mains by opening the contactor located upstream the motor and the sensitive load can be supplied through the generator. The mitigation capability of this device is related to the inertia and to the rotational speed of the flywheel.

This system has high efficiency, low initial costs and enables long-duration ride through (up to several seconds), depending on the inertia of the flywheel. However, the motor-generator set can only be used in industrial environment, due to its size, noise and maintenance requirements.

Transformer-based mitigation devices

A constant voltage, or ferro-resonant, transformer works in a similar manner to a transformer with 1:1 turns ratio which is excited at a high point on its saturation curve, thus providing an output voltage that is not affected by input voltage variations. In the actual design, as shown in Fig.2.6, a capacitor, connected to the secondary winding, is needed to set the operating point above the knee of the saturation curve. This solution is suitable for low-power (less than 5 kVA [45]), constant loads: variable loads can cause problems, due to the presence of this tuned circuit on the output. Electronic tap changers (Fig.2.7) can be mounted on a dedicated transformer for the sensitive load, in order to change its turns ratio according to changes in the input voltage. They can be connected in series on the distribution feeder and be placed between the supply and the load. Part of the secondary winding supplying the load is divided into a number of sections, which are connected or disconnected by fast static switches, thus allowing regulation of the secondary voltage in steps. This should allow the output voltage to be brought back to a level above 90% of nominal value, even for severe voltage dips. If thyristor-based switches are used, they can only be turned on once per cycle and therefore the compensation is accomplished with a time delay of at least one half-cycle. An additional problem is that the current in the primary winding increases when the secondary voltage is increased to compensate for the dip in the grid voltage. Therefore, only small steps on the secondary side of the transformer are allowed. Furthermore, due to the use of thyristor-based static switches, when the supply voltage is restored to its pre-fault value the load will experience an overvoltage for at least one half-cycle.

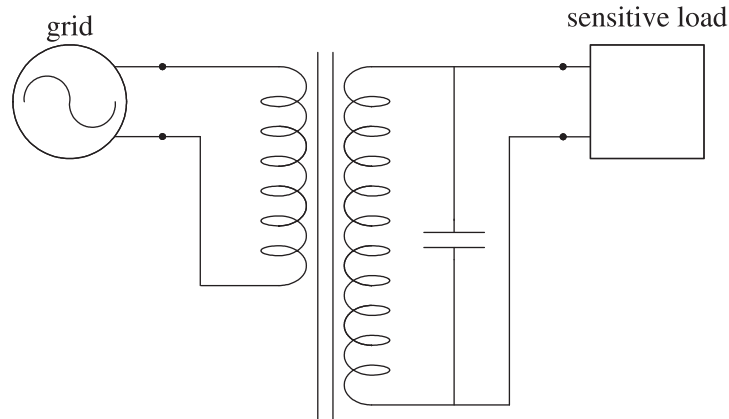


Fig. 2.6 Single-line diagram of ferro-resonant transformer.

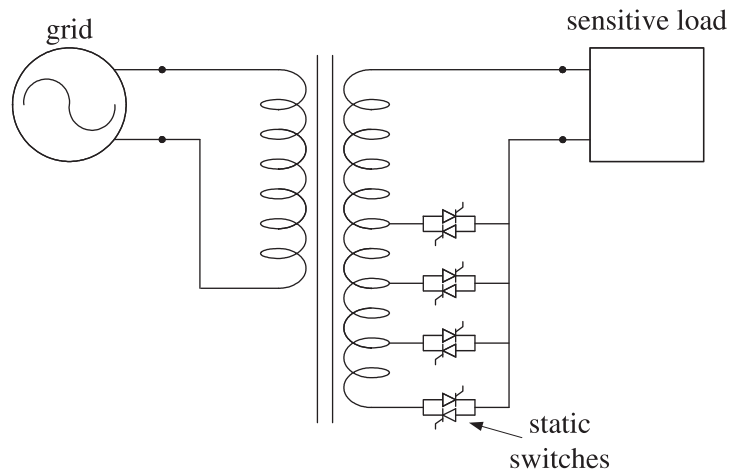


Fig. 2.7 Single-line diagram of transformer with electronic tap changers.

Static Transfer Switch

The Static Transfer Switch (STS) consists of two three-phase static switches, each constituted in turn of two antiparallel thyristors per phase, as shown in Fig.2.8, where the single-line diagram of an STS is displayed [64]. The aim of this device is to transfer the load from a primary source to a secondary one automatically and rapidly when reduced voltage is established in the primary source and while the secondary meets certain quality requirements. During normal operation, the primary source feeds the load through the thyristors of switch 1, while the secondary source is disconnected (switch 2 open). In case of voltage dips or interruptions in the primary source, the load will be transferred from the primary to the alternative source. Different control strategies in order to obtain instantaneous transfer of the load can be adopted. However, paralleling between the two sources during the transfer must be avoided. For this reason, since thyristor base switches are used, the transfer time can take up to one half-cycle [61]. This means that the load will still be affected by the dip, but its duration will be reduced to the time necessary to transfer the load from the primary to the secondary source. The shortcoming of the STS is that it cannot mitigate voltage dips originated by faults in the transmission system, since these

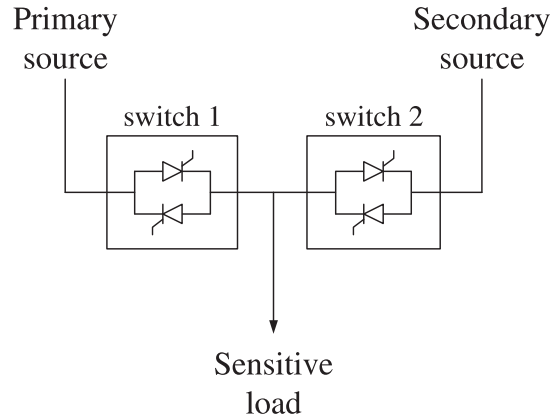


Fig. 2.8 Single-line diagram of Static Transfer Switch (STS).

type of dips usually affect both the primary and the secondary source. Moreover, it continuously conduct the load current, which leads to considerable conduction losses.

Uninterruptible Power Supply

An Uninterruptible Power Supply (UPS) consists of a back-to-back converter (typically a diode rectifier followed by an inverter) and an energy storage, as shown in Fig.2.9 [63]. The energy storage is usually a battery connected to the dc link. During normal operation, the power coming from the ac supply is rectified and then inverted to feed the load. The battery remains in standby mode and only keeps the dc-bus voltage constant. During a voltage dip or an interruption, the energy released by the battery keeps the voltage at the dc bus constant. Depending on the storage capacity of the battery, it can supply the load for minutes or even hours. Low cost, simple operation and control have made the UPS the standard solution for low-power, single phase equipment, like computers. For higher-power loads, the costs associated with losses due to the two conversions and maintenance of the batteries become too high and, therefore, a three-phase, high power UPS is not economically feasible.

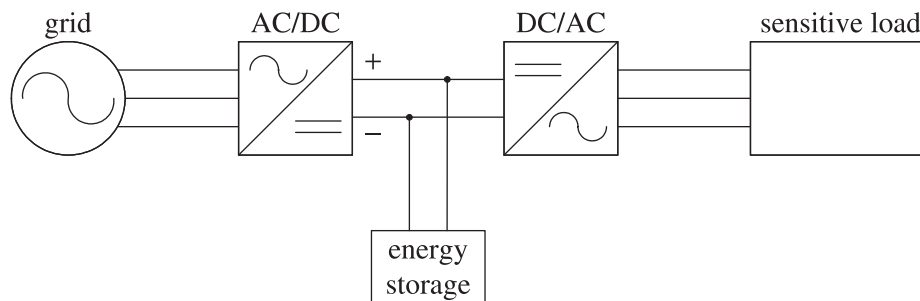


Fig. 2.9 Three-phase diagram of UPS.

Shunt-connected VSC

The basic idea of the shunt-connected VSC is to dynamically inject a current $\underline{i}_r(t)$ of desired amplitude, frequency and phase into the grid. The typical configuration of a shunt-connected VSC is shown in Fig.2.10. The device consists of a VSC, an injection transformer, an ac filter and a dc-link capacitor. An energy storage can also be mounted on the dc link to allow active power injection into the ac grid.

The line impedance has a resistance R_g and inductance L_g . The grid voltage and current are denoted by $\underline{e}_s(t)$ and $\underline{i}_g(t)$, respectively. The voltage at the point of common coupling (PCC), which is also equal to the load voltage, is denoted by $\underline{e}_g(t)$ and the load current by $\underline{i}_l(t)$. The inductance and resistance of the ac-filter reactor are denoted by R_r and L_r , respectively. Figure 2.11 shows a simplified single-line diagram, where the VSC is represented as a current source. Amplitude, frequency and phase of the current $\underline{i}_r(t)$ can be controlled.

By injecting a controllable current, the shunt-connected VSC can limit voltage fluctuation leading to flicker [70] and cancel harmonic currents absorbed by the load, thus operating as an active filter [2]. In both cases, the principle is to inject a current with same amplitude and opposite phase as the undesired frequency components in the load current, so that they are cancelled in the grid current. These mitigation actions can be accomplished by only injecting reactive power. A shunt-connected VSC can also be used for voltage dip mitigation. In this case, the device has to inject a fundamental current in the grid, resulting in an increased voltage amplitude at the PCC, as shown in the phasor diagram in Fig.2.12. The voltage phasor at PCC is denoted by \overline{E}_g , \overline{Z}_g is the line impedance, $\overline{E}_{s,dip}$ is the grid voltage phasor during the dip and ψ is the phase-angle jump of the dip. From the diagram it is possible to understand that when the shunt-connected VSC is used to mitigate voltage dips, it is necessary to provide an energy storage for injection of active power in order to avoid phase-angle jumps of the load voltage. If only reactive power is injected, it is possible to maintain the load voltage amplitude E_g to the pre-fault conditions but not its phase. Therefore, the voltage dip mitigation capability of a shunt-connected VSC depends on the rating of the energy storage and on the rating in current

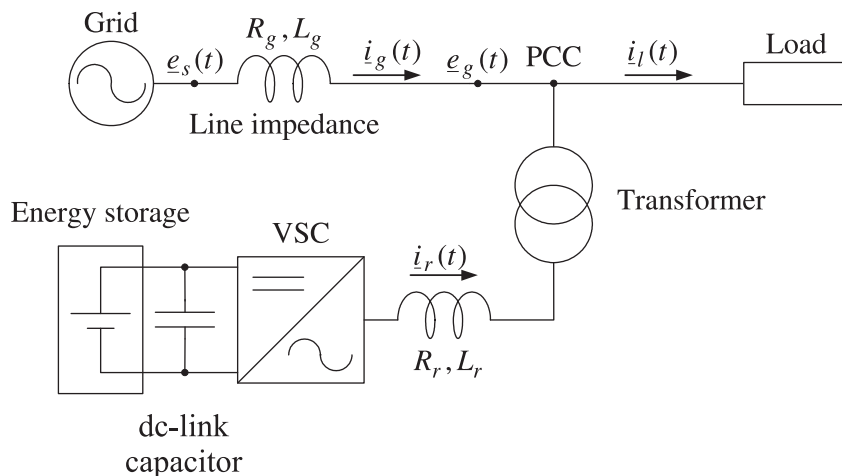


Fig. 2.10 Single-line diagram of shunt-connected VSC.

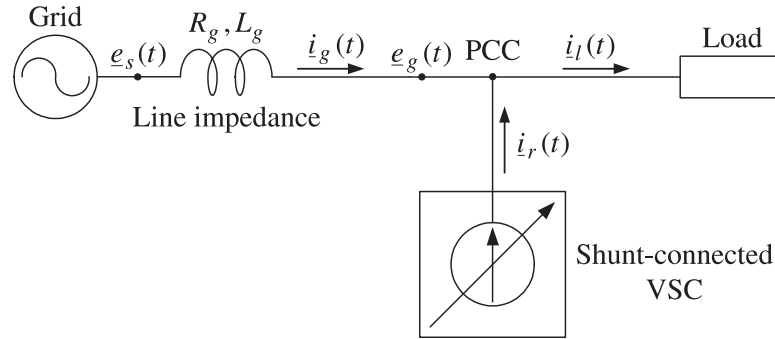


Fig. 2.11 Simplified single-line diagram of shunt-connected VSC.

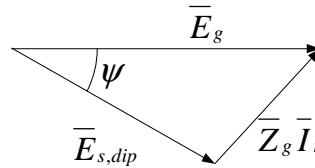


Fig. 2.12 Phasor diagram of voltage dip mitigation using shunt-connected VSC.

of the VSC.

Series-connected VSC

In this section, the principle of operation of the series-connected VSC (also called static series compensator, SSC) will be described. The basic idea is to inject a voltage $e_c(t)$ of desired amplitude, frequency and phase between the PCC and the load in series with the grid voltage. A typical configuration of the SSC is shown in Fig.2.13: the main components of the SSC are the VSC, the filter, the injection transformer and the energy storage. Figure 2.14 shows a simplified single-line diagram of the system with SSC. Differently from the shunt-connected VSC, the SSC can be represented as a voltage source with controllable amplitude, phase and frequency.

The SSC is mainly used for voltage dip mitigation. The device maintains the load voltage $e_l(t)$ to the pre-fault condition by injecting a fundamental voltage of appropriate amplitude and phase. Figure 2.15 shows the phasor diagram of the series injection principle during voltage dip mitigation, where \bar{E}_c is the phasor of the voltage injected by the compensator, \bar{I}_1 is the phasor of the load current and where φ is the angle displacement between load voltage and current.

As for the shunt-connected VSC described in the previous section, in order to be able to restore both magnitude and phase of the load voltage to the pre-fault conditions, the SSC has to inject both active and reactive power [13]. The voltage dip mitigation capability of this device depends on the rating of the energy storage and on the voltage ratings of the VSC and the injection transformer.

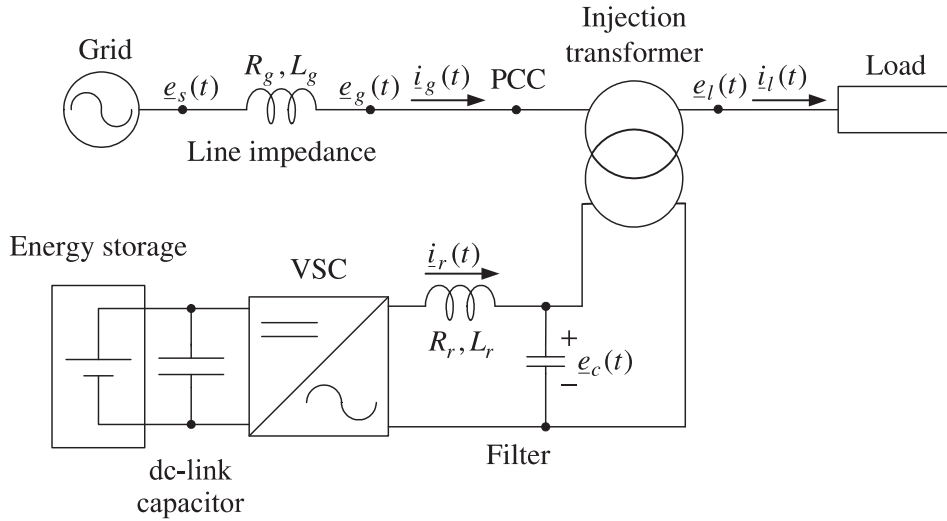


Fig. 2.13 Single-line diagram of SSC.

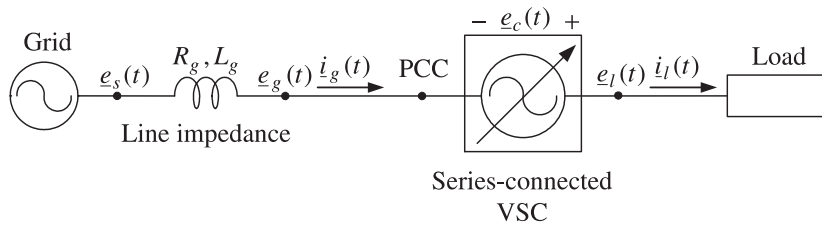


Fig. 2.14 Simplified single-line diagram of system with SSC.

2.4 Conclusions

In this chapter, a brief overview of voltage dips, with their origin and classification has been given. Different methods for voltage dip mitigation have been described. Among all methods, the installation of a mitigation device seems to be the only solution for customers to protect themselves from voltage dips. Different mitigation devices, based on passive devices and based on power electronics, have been described. Particular emphasis has been given to the shunt-connected VSC and to the Static Series Compensator (SSC), which are the core of this part of the thesis. In the next chapters, these two devices, and especially their control system, will be described in detail.

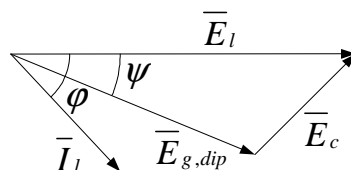


Fig. 2.15 Phasor-diagram of voltage dip mitigation using SSC.

Chapter 3

Vector Current-controller for Grid-connected VSC

This chapter deals with the derivation and the analysis of the deadbeat current controller for grid-connected VSCs. Improvements to the standard algorithm in order to control positive and negative sequences of the line-filter current (VSC terminal current) are further presented in Papers III and IV. In particular, Paper III shows simulation and experimental results of the investigated controllers under balanced and unbalanced conditions of the grid voltage. Further, in Paper IV the dynamic performance of the investigated controllers has been tested under symmetrical and unsymmetrical voltage dips.

3.1 Introduction

Grid-connected forced-commutated VSCs are becoming more and more common at distribution level for applications such as wind power plants, active front-end for adjustable speed drives and custom power devices. Also VSCs for transmission level are introduced in HVDCs and FACTS devices. Benefits of using VSCs are sinusoidal currents, high current bandwidth, controllable reactive power to regulate power factor or bus-voltage level and to minimize resonances between the grid and the converter, independent control of active and reactive power. These characteristics, which are highly desirable in grid-connected applications, can be obtained by using a high-performance current controller for the VSC. In the following, the deadbeat current controller will be derived and analyzed. An extended analysis of the control system, its problems and possible solutions will be carried out.

3.2 Vector Current-controller (VCC)

To obtain a high performance system, it is important to maximize the current bandwidth of the VSC. In a Vector Current-control (VCC) system, the active and reactive currents (as well as the active and reactive powers) can be controlled independently. As a result, a high-bandwidth

controller with a low cross-coupling between the reference currents and the line-filter currents can be achieved [16, 71].

The VSC is the most important element in the design of the investigated system. Figure 3.1 shows the main circuit scheme of a three-phase VSC. The VSC is connected to a symmetric three-phase load with impedance $R_l + j\omega L_l$ and back emfs $e_a(t)$, $e_b(t)$ and $e_c(t)$. The phase potential, phase voltages and the potential of the floating-star load are denoted by $v_a(t)$, $v_b(t)$, $v_c(t)$, $u_a(t)$, $u_b(t)$, $u_c(t)$ and $v_0(t)$ respectively. The load currents in the three phases are denoted by $i_{ra}(t)$, $i_{rb}(t)$, $i_{rc}(t)$ respectively. The valves in the phase-legs of the VSC (usually insulated gate bipolar transistors, IGBTs) are controlled by the switching signals $sw_a(t)$, $sw_b(t)$ and $sw_c(t)$. The dc-link voltage is denoted by $u_{dc}(t)$. The switching signal can be equal to ± 1 . When $sw_a(t)$ is equal to 1, the upper valve in the phase a is turned on while the lower valve in the same leg is off. Therefore, the potential $v_a(t)$ is equal to half of the dc-link voltage ($u_{dc}(t)/2$). Vice versa, when the switching signal is equal to -1 , the upper valve is off and the lower one is on and, thus, $v_a(t)$ is equal to $-u_{dc}(t)/2$. The potential $v_0(t)$ can be written as

$$v_0(t) = \frac{1}{3} [v_a(t) + v_b(t) + v_c(t)] \quad (3.1)$$

assuming that the load is symmetrical. The phase voltages become

$$u_a(t) = v_a(t) - v_0(t) \quad (3.2)$$

$$u_b(t) = v_b(t) - v_0(t) \quad (3.3)$$

$$u_c(t) = v_c(t) - v_0(t) \quad (3.4)$$

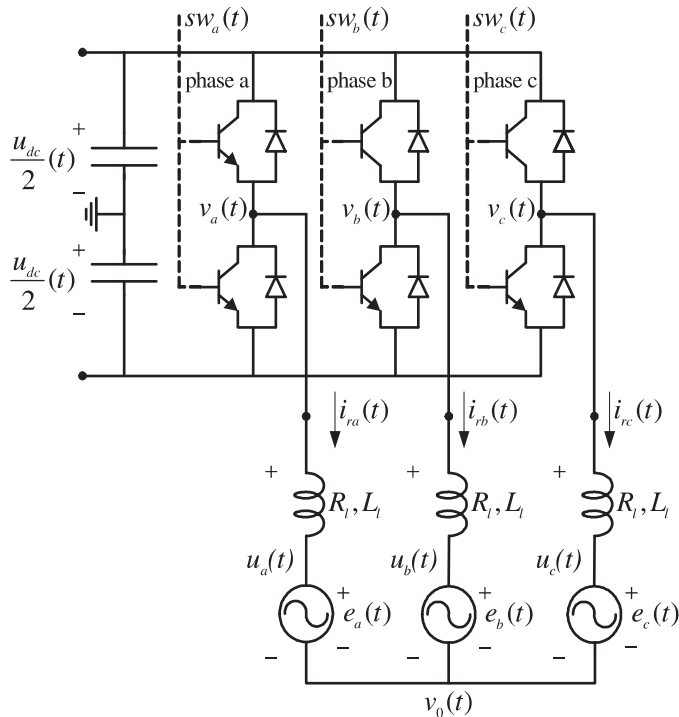


Fig. 3.1 Main circuit of three-phase VSC and load consisting of impedance and voltage sources.

3.2. Vector Current-controller (VCC)

To obtain the switching signals for the VSC, Pulse Width Modulation technique (PWM) has been adopted [34]. To avoid short-circuit of the VSC phase-legs, blanking time must be applied [47]. Assuming that the switching frequency is very high, during steady-state operation the VSC can be modelled as an ideal three-phase voltage source. Therefore, the output voltages of the VSC can be considered sinusoidal and equal to the reference voltages to the modulator, given by

$$u_a^*(t) = \sqrt{\frac{2}{3}}U^* \sin(\omega^*t + \phi^*) \quad (3.5)$$

$$u_b^*(t) = \sqrt{\frac{2}{3}}U^* \sin(\omega^*t + \phi^* - \frac{2}{3}\pi) \quad (3.6)$$

$$u_c^*(t) = \sqrt{\frac{2}{3}}U^* \sin(\omega^*t + \phi^* - \frac{4}{3}\pi) \quad (3.7)$$

where U^* , ω^* and ϕ^* are the reference value of the phase-to-phase RMS voltage, the reference angular frequency and the reference phase-shift respectively.

In the three-phase diagram of the VSC system displayed in Fig.3.2, the grid voltages at the PCC are denoted by $e_{g,a}(t)$, $e_{g,b}(t)$ and $e_{g,c}(t)$. The currents through the filter reactor are $i_{r,a}(t)$, $i_{r,b}(t)$ and $i_{r,c}(t)$ and the phase voltages out of the VSC are denoted by $u_a(t)$, $u_b(t)$ and $u_c(t)$. The resistance and the inductance of the filter reactor are denoted by R_r and L_r , respectively.

Applying Kirchhoff's voltage law (KVL), the following differential equations for the three phases can be obtained

$$u_a(t) - e_{g,a}(t) - R_r i_{r,a}(t) - L_r \frac{d}{dt} i_{r,a}(t) = 0 \quad (3.8)$$

$$u_b(t) - e_{g,b}(t) - R_r i_{r,b}(t) - L_r \frac{d}{dt} i_{r,b}(t) = 0 \quad (3.9)$$

$$u_c(t) - e_{g,c}(t) - R_r i_{r,c}(t) - L_r \frac{d}{dt} i_{r,c}(t) = 0 \quad (3.10)$$

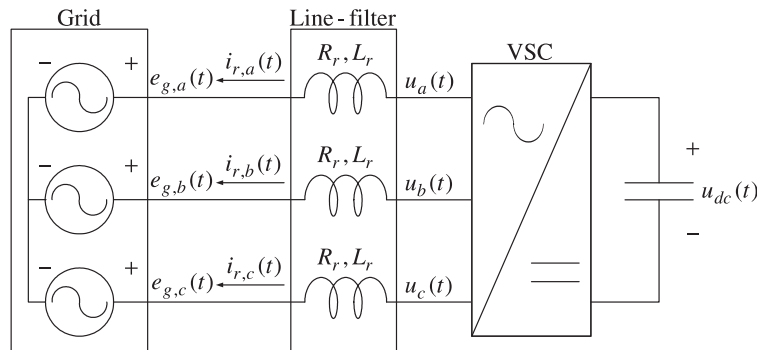


Fig. 3.2 Three-phase diagram of grid-connected VSC system.

Chapter 3. Vector Current-controller for Grid-connected VSC

By applying Clarke's transformation, (3.8) to (3.10) can be written in the fixed $\alpha\beta$ -coordinate system as

$$\underline{u}^{(\alpha\beta)}(t) - \underline{e}_g^{(\alpha\beta)}(t) - R_r \underline{i}_r^{(\alpha\beta)}(t) - L_r \frac{d}{dt} \underline{i}_r^{(\alpha\beta)}(t) = 0 \quad (3.11)$$

The $\alpha\beta$ - to dq -transformation (in Appendix A) is applied. The phase-locked loop (PLL) [17,30] is synchronized with the grid voltage vector $\underline{e}_g^{(\alpha\beta)}$ and the transformation angle is denoted by θ , equal to the grid voltage angle in steady state. The VSC voltage vector in the rotating dq -coordinate system is equal to

$$\underline{u}^{(dq)}(t) = e^{-j\theta(t)} \underline{u}^{(\alpha\beta)}(t) = e^{-j\omega t} \underline{u}^{(\alpha\beta)}(t) \quad (3.12)$$

with ω the system frequency. Similar transformation can be applied to the grid voltage and to the filter current. Thus, (3.11) can be rewritten in the rotating dq -frame as

$$\underline{u}^{(dq)}(t) - \underline{e}_g^{(dq)}(t) - R_r \underline{i}_r^{(dq)}(t) - L_r \frac{d}{dt} \underline{i}_r^{(dq)}(t) - j\omega L_r \underline{i}_r^{(dq)}(t) = 0 \quad (3.13)$$

With the chosen PLL [30] (see also Paper II), the voltage vector is aligned with the direction of the d -axis during steady state. The grid voltage component in the d -direction is equal to its RMS-value (when using power-invariant transformation, Appendix A) and the q -component of the grid voltage is equal to zero. Thus, the d -component of the current vector (in steady state parallel to the grid voltage vector) becomes the active current component (d -current) and the q -component of the current vector becomes the reactive current component (q -current). Observe that, in agreement with the signals reference in Fig.3.2, positive current (power) means current injected by the VSC into the grid.

3.2.1 Proportional controller

In this section, the proportional controller will be derived for the VCC.

Considering that the control system has to be implemented in a digital controller and that it will operate in discrete time, it is necessary to discretize (3.13). By integrating this equation over one sample period T_s (from time kT_s to time $(k+1)T_s$) and then dividing by the sample time T_s , the following equation can be obtained

$$\begin{aligned} \underline{u}^{(dq)}(k, k+1) &= \underline{e}_g^{(dq)}(k, k+1) + R_r \underline{i}_r^{(dq)}(k, k+1) + j\omega L_r \underline{i}_r^{(dq)}(k, k+1) + \\ &+ \frac{L_r}{T_s} [\underline{i}_r^{(dq)}(k+1) - \underline{i}_r^{(dq)}(k)] \end{aligned} \quad (3.14)$$

where $\underline{u}^{(dq)}(k, k+1)$ denotes the average value of the voltage vector $\underline{u}^{(dq)}$ from sample k to sample $k+1$ (and analogously for the other quantities) [69]. If a proportional regulator with deadbeat gain is used, the controller will track the reference currents with one sample delay [3]. Thus, the current reference value at the sample instant k must be equal to the current value at the sample $k+1$, i.e.

$$\underline{i}_r^{(dq)}(k+1) = \underline{i}_r^{(dq)*}(k) \quad (3.15)$$

The following assumptions can be made in order to derive the controller:

3.2. Vector Current-controller (VCC)

- The grid voltage changes slowly and can be considered constant over one sample period

$$\underline{e}_g^{(dq)}(k, k+1) = \underline{e}_g^{(dq)}(k) \quad (3.16)$$

- The current variations are linear

$$\underline{i}_r^{(dq)}(k, k+1) = \frac{1}{2} [\underline{i}_r^{(dq)}(k) + \underline{i}_r^{(dq)}(k+1)] = \frac{1}{2} [\underline{i}_r^{(dq)}(k) + \underline{i}_r^{(dq)*}(k)] \quad (3.17)$$

- The average value of the VSC voltage over a sample period is equal to the reference value

$$\underline{u}^{(dq)}(k, k+1) = \underline{u}^{(dq)*}(k) \quad (3.18)$$

Under these assumptions, the proportional controller can be rewritten as follows [72]

$$\begin{aligned} \underline{u}^{(dq)*}(k) &= \underline{e}_g^{(dq)}(k) + R_r \underline{i}_r^{(dq)}(k) + \mathbf{j} \frac{\omega L_r}{2} [\underline{i}_r^{(dq)}(k) + \underline{i}_r^{(dq)*}(k)] + \\ &+ \left(\frac{L_r}{T_s} + \frac{R_r}{2} \right) [\underline{i}_r^{(dq)*}(k) - \underline{i}_r^{(dq)}(k)] = \underline{u}_{ff}^{(dq)}(k) + k_p [\underline{i}_r^{(dq)*}(k) - \underline{i}_r^{(dq)}(k)] \end{aligned} \quad (3.19)$$

where $\underline{u}_{ff}^{(dq)}$ is the feed-forward voltage term for at sample k , while

$$k_p = \frac{L_r}{T_s} + \frac{R_r}{2} \quad (3.20)$$

is the proportional gain of the controller to obtain deadbeat.

3.2.2 Proportional-integral controller

In order to remove static errors caused by non-linearities, noise in the measurements and non-ideal components, an integral part is introduced in the controller [60]. The controller using PI-regulator can be formulated in discrete time as

$$\underline{u}^{(dq)*}(k) = \underline{u}_{ff}^{(dq)}(k) + k_p [\underline{i}_r^{(dq)*}(k) - \underline{i}_r^{(dq)}(k)] + \Delta \underline{u}_i^{(dq)}(k) \quad (3.21)$$

where $\Delta \underline{u}_i^{(dq)}(k)$ is the integral term at sample k , given by

$$\Delta \underline{u}_i^{(dq)}(k) = \Delta \underline{u}_i^{(dq)}(k-1) + k_i [\underline{i}_r^{(dq)*}(k-1) - \underline{i}_r^{(dq)}(k-1)] \quad (3.22)$$

where the integral gain k_i can be written as

$$k_i = k_p \frac{T_s}{T_i} \quad (3.23)$$

with T_i the integration time constant. After some algebraic manipulation of (3.21) [3], the latter is found as

$$T_i = \frac{L_r}{R_r} + \frac{T_s}{2} \approx \frac{L_r}{R_r} \quad (3.24)$$

to obtain deadbeat. From (3.20) and (3.24) it is possible to notice that the parameters of the PI-controller are directly related to the filter parameters R_r and L_r . This represents a useful tool when analyzing the sensitivity of the control system to system variations.

In Fig.3.3, the block scheme of the vector current-controller is displayed. The algorithm of the vector current-controller can be summarized as follows:

1. Measure grid voltages and filter currents and sample them with sampling frequency f_s ;
2. Transform all quantities from the three-phase coordinate system to the fixed $\alpha\beta$ -coordinate system and then to the rotating dq -coordinate system, using the transformation angle $\theta(k)$, obtained from the PLL;
3. Calculate the reference voltage $\underline{u}^{(dq)*}(k)$;
4. Convert the reference voltage from the rotating dq -coordinate system to the three-phase coordinate system by using the transformation angle $\theta(k) + \Delta\theta$, where $\Delta\theta = 0.5\omega T_s$ is a compensation angle to take into account the delay introduced by the discretization of the measured quantities [72];
5. Calculate the duty-cycles [47] in the PWM block and send the switching pulses to the VSC valves.

3.3 Vector Current-controller type 1 (VCC1)

In the previous section, the VCC has been derived in ideal conditions, i.e. under the assumption that the VSC is an ideal controllable voltage source. However, in practical applications, it is

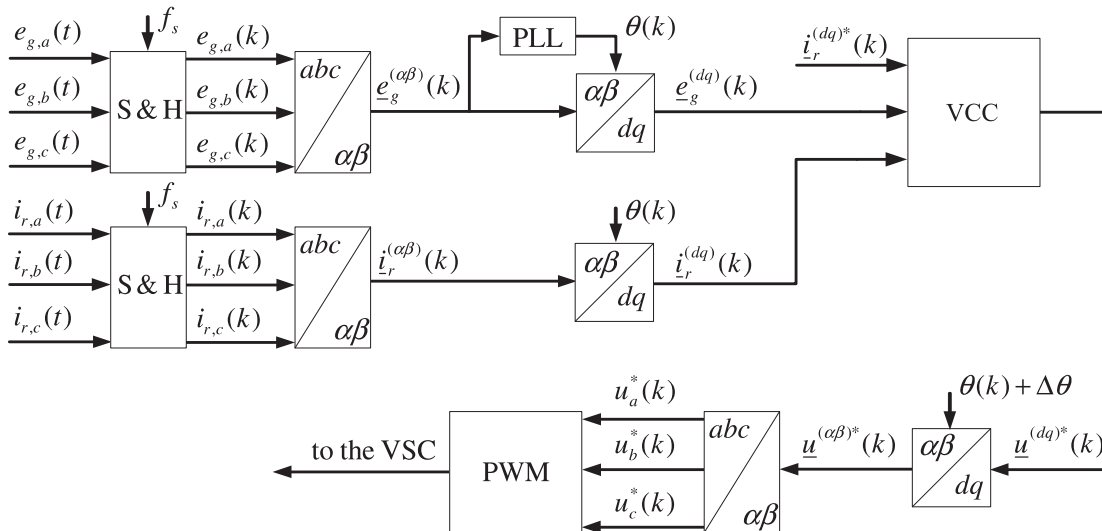


Fig. 3.3 Block scheme of implemented vector current-controller.

3.3. Vector Current-controller type 1 (VCC1)

necessary to improve the control system in order to take into account some problems that occur in a real system. In particular, it is important to consider that the amplitude of the output voltage of the VSC is not infinite, but limited and proportional to the dc-link voltage level. Moreover, all calculations are affected by the delay due to the computational time of the control computer. For this reason, some improvements have been made to the described current controller:

- Smith predictor using a state observer for the computational time delay compensation [51, 68];
- Limitation of the reference voltage vector and anti-windup function to prevent integrator windup [51, 68].

3.3.1 One-sample delay compensation

In a real system, the reference voltage used in the PWM modulator $\underline{u}^{(dq)*}(k)$ is delayed one sampling period due to the computational time in the control computer. If a high bandwidth control system is used, this delay will affect the performance of the system and large oscillations in the output current can be experienced [10]. To avoid this problem and be able to use a fast controller, it is necessary compensate for this delay.

In this thesis, a Smith predictor has been used for this purpose [57]. The main advantage by using a Smith predictor is that the current controller can be treated as in the ideal case without any time delay. The basic idea of the Smith predictor is to predict the output current one sample ahead by using a state observer and feed the predicted current back into the current controller. Thus, the delay of one sample has been eliminated. In order to feedback the real current to the current controller, the predicted current one sample delayed is subtracted from the feedback signal. The block scheme of the current controller with the computational time delay, the Smith predictor and the process (equal to the VSC system shown in Fig.3.2) is displayed in Fig.3.4. The output of the Smith predictor is the difference between the estimated filter current at sample k , denoted in the figure as $\hat{\underline{i}}_r^{(dq)}(k)$, and the same signal at sample $k - 1$. If at sample k a step in the reference current is applied, at sample $k + 1$ the reference voltage $\underline{u}^{(dq)*}$ output of the current controller will vary. As a result, the output signal of the Smith predictor will not be equal to zero and will adjust the current error. At sample $k + 2$ the difference between the predicted current and the delayed one will be zero again. Thus, the Smith predictor will not affect the current error. Therefore, the Smith predictor will affect the performance of the controller only during transients, but not during steady state.

For a correct estimation of the grid current, the state observer has to be designed in order to reproduce the process. Applying KVL to the circuit shown in Fig.3.5, the following equation in the $\alpha\beta$ -coordinate system can be written

$$\underline{u}^{(\alpha\beta)}(t) - \underline{e}_g^{(\alpha\beta)}(t) = R_r \hat{\underline{i}}_r^{(\alpha\beta)}(t) + L_r \frac{d}{dt} \hat{\underline{i}}_r^{(\alpha\beta)}(t) \quad (3.25)$$

Chapter 3. Vector Current-controller for Grid-connected VSC

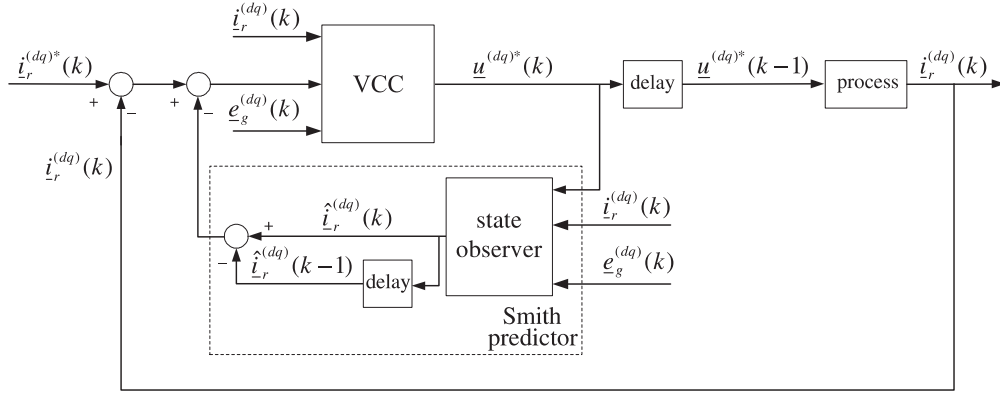


Fig. 3.4 Block scheme of vector current-controller with Smith predictor and process.

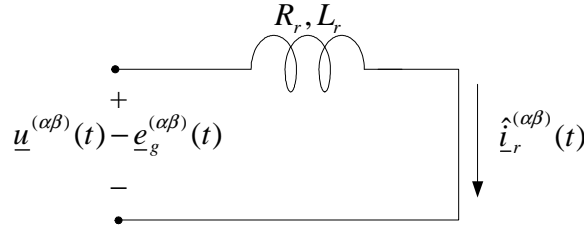


Fig. 3.5 Single-line diagram of circuit representation of state observer.

In the dq -coordinate system, (3.25) becomes

$$\underline{u}^{(dq)}(t) - \underline{e}_g^{(dq)}(t) = R_r \hat{\underline{i}}_r^{(dq)}(t) + j\omega L_r \hat{\underline{i}}_r^{(dq)}(t) + L_r \frac{d}{dt} \hat{\underline{i}}_r^{(dq)}(t) \quad (3.26)$$

which can be discretized using the forward Euler method. Assuming that the average values of the VSC voltages over one sample period are equal to the reference values, (3.26) can be rewritten in the discrete time domain as

$$\hat{\underline{i}}_r^{(dq)}(k+1) = \left(1 - \frac{R_r T_s}{L_r} - j\omega T_s \right) \hat{\underline{i}}_r^{(dq)}(k) + \frac{T_s}{L_r} [\underline{u}^{(dq)*}(k) - \underline{e}_g^{(dq)}(k)] \quad (3.27)$$

The measured current $\underline{i}_r^{(dq)}(k)$ and the predicted current $\hat{\underline{i}}_r^{(dq)}(k)$ are equal in an ideal system, but in a real system, due to nonlinearities and noise in the measurements, this relation is no longer valid. Therefore, an additional term is included to take into account this error in the estimation, giving the final equation for the state observer as

$$\begin{aligned} \hat{\underline{i}}_r^{(dq)}(k+1) = & \left(1 - \frac{R_r T_s}{L_r} - j\omega T_s \right) \hat{\underline{i}}_r^{(dq)}(k) + \frac{T_s}{L_r} [\underline{u}^{(dq)*}(k) - \underline{e}_g^{(dq)}(k)] + \\ & + k_{\text{psp}} [\underline{i}_r^{(dq)}(k) - \hat{\underline{i}}_r^{(dq)}(k)] \end{aligned} \quad (3.28)$$

where k_{psp} denotes the observer gain. Thus, if k_{psp} is large, the observer does not trust the process model (measurements and estimated system parameters). If k_{psp} is small, the observer believes in the process model.

3.3. Vector Current-controller type 1 (VCC1)

To obtain the reference phase voltages, the reference voltage vector $\underline{u}^{(dq)*}$ in the dq -coordinate system is transformed in the fixed $\alpha\beta$ -coordinate system, as shown earlier in Fig.3.3. The one-sample delay due to the computational time affects also the compensation angle $\Delta\theta$. For a correct transformation, the reference voltage vector in the $\alpha\beta$ -plane is given by

$$\underline{u}^{(\alpha\beta)*} = \underline{u}^{(dq)*} e^{j(\theta+\Delta\theta)} = \underline{u}^{(dq)*} e^{j(\theta+\frac{3}{2}\omega T_s)} \quad (3.29)$$

3.3.2 Saturation and integrator anti-windup

In this section, the problem with saturation of the VSC and different solutions (stopping the integration during saturation and use of back-calculation) to avoid integrator windup will be treated.

In Section 3.2, the principle of operation of the VSC has been treated. As explained in [41], the three switching signals sw_a , sw_b and sw_c can be combined in eight ways. The resulting voltage vectors for these combinations draw a hexagon in the fixed $\alpha\beta$ -coordinate system. Figure 3.6 shows the eight realizable voltage vectors, their switching combinations and the relative sectors for the two-level VSC. A vector $\underline{u}(sw_a, sw_b, sw_c)$ with switching states $sw_a = 1$, $sw_b = -1$ and $sw_c = 1$ is represented as $\underline{u}(1, -1, 1)$.

The VSC is capable to deliver voltages within this hexagon. Linear modulation is possible up to the radius of the maximum circle that can be inscribed inside the hexagon. This is equal to $u_{dc}/\sqrt{2}$ if power-invariant transformation is used. During transients, it is also possible to control the PWM voltage outside this circle but within the hexagon, in order to improve the dynamic performance of the control system.

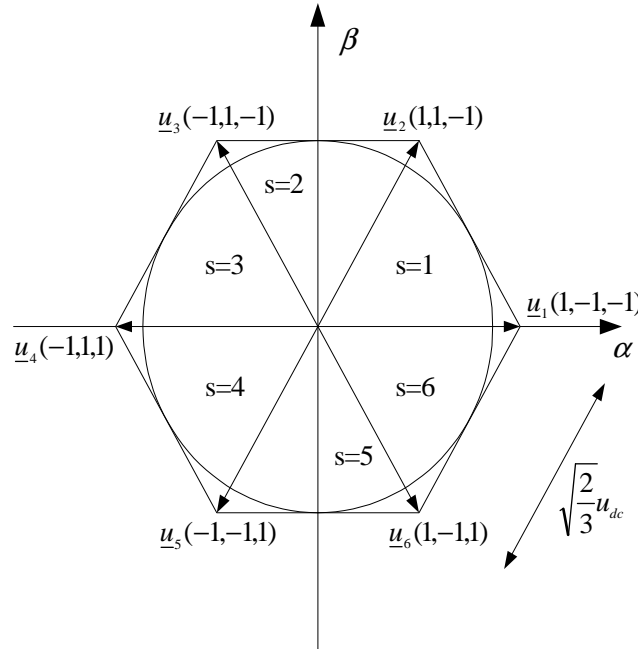


Fig. 3.6 Hexagon including the eight realizable voltage vectors for VSC.

If saturation occurs (i.e. if the reference voltage vector exceeds the boundary of the hexagon), the VSC will not be able to deliver the demanded voltage and reduced performance of the system will be obtained. For this reason, in case of saturation it is necessary to reduce the demanded voltage within the boundary of the hexagon.

In [51], an extended description of the saturation problem and possible solutions for the limitation of the reference voltages for the PWM modulator are reported. Here, the method used is the Minimum Amplitude Error limitation method (MAE). According to MAE, the limited voltage vector $\underline{u}_r^{(\alpha\beta)*}$ is chosen on the hexagon boundary nearest the original reference vector $\underline{u}^{(\alpha\beta)*}$. Thus, MAE minimizes the voltage amplitude error. As shown in Fig.3.7, using the auxiliary xy -coordinate system, the components of the limited reference voltage vector become

$$u_{rx}^* = \frac{u_{dc}}{\sqrt{2}} \quad (3.30)$$

$$u_{ry}^* = \begin{cases} u_y^* & |u_y^*| \leq u_{dc}/\sqrt{6} \\ \text{sgn}(u_y^*) \frac{u_{dc}}{\sqrt{6}} & |u_y^*| > u_{dc}/\sqrt{6} \end{cases} \quad (3.31)$$

The transformation angle θ_{xy} is the angle between the α -axis and the x -axis and is defined as

$$\theta_{xy} = [1 + 2(s - 1)] \pi/6 \quad (3.32)$$

where s is the hexagon sector where the voltage vector $\underline{u}^{(\alpha\beta)*}$ is located.

If saturation occurs, the output voltage of the current controller will be limited to the boundary of the hexagon and the output voltage will be smaller compared with the demanded one. In this case, if a controller with an integral part is used, the current error will be integrated and, as a consequence, the integration term can become very large because the output voltage cannot be increased, thus reducing the current error. This phenomenon is called “integrator windup”

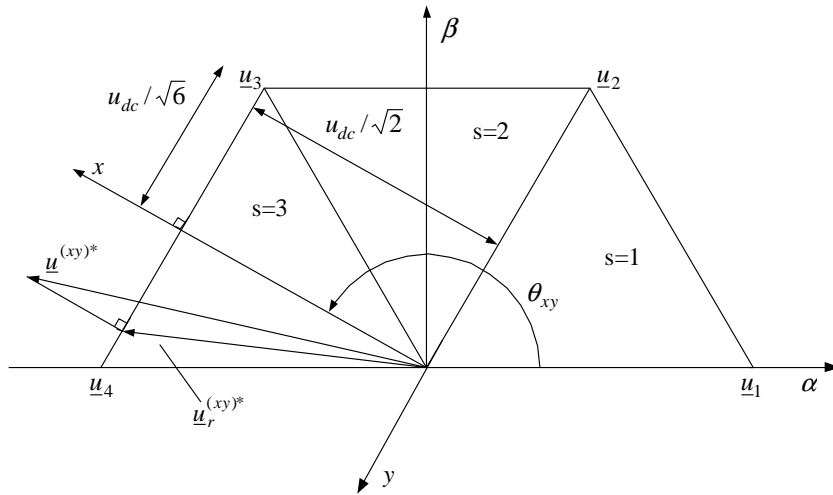


Fig. 3.7 Principle of MAE method to limit reference voltage vector to hexagon boundary.

3.3. Vector Current-controller type 1 (VCC1)

[68]. Figure 3.8 shows the dynamic performance of the deadbeat vector current-controller with VSC voltage limitation and with no integrator anti-windup. At time $t = 0.1$ s a step in the d -component of the reference current from -0.5 pu to 1 pu has been applied. The q -component of the reference current (not shown for clarity) is constant to 0 pu. The signal “sat” indicates VSC saturation. As shown, the transient behavior of the control system is rather sluggish and after the step, the actual current is affected by a steady-state error that decreases slowly down to zero. The sluggish behavior of the error is caused by windup of the integrator.

A countermeasure to avoid integrator windup is to inhibit the integration, by setting the integrator gain k_i equal to zero, whenever the output of the VSC saturates. Another solution is to use a back-calculation of the current error in order to limit the demanded current during saturation [3, 28, 68]. In this case, if saturation occurs, the integrated current error will be modified in order to take into account the limited VSC control voltage. The back-calculated error is given by [28]

$$\dot{i}_{er}^{(dq)}(k) = \frac{1}{k_p} [\underline{u}_r^{(dq)*}(k) - \underline{u}_{ff}^{(dq)}(k) - \Delta \underline{u}_i^{(dq)}(k)] \quad (3.33)$$

where $\underline{u}_r^{(dq)*}$ is the limited reference voltage vector, while all other terms have the same meaning given in Section 3.2.

Figures 3.9 and 3.10 show the step response of the deadbeat vector current-controller with integrator stop and back-calculation, respectively. The two methods are practically equivalent: the advantage of using back-calculation is that if saturation occurs the integrator is not frozen, but is dynamically adjusted. Due to the presence of the integral part in the controller even during saturation, the back-calculation results slightly faster as compared with the integrator stop. Therefore, this solutions has been here adopted.

The complete block scheme of the VCC with all modifications mentioned is shown in Fig.3.11. From this point on, this will be referred to as Vector Current-controller type 1, VCC1.

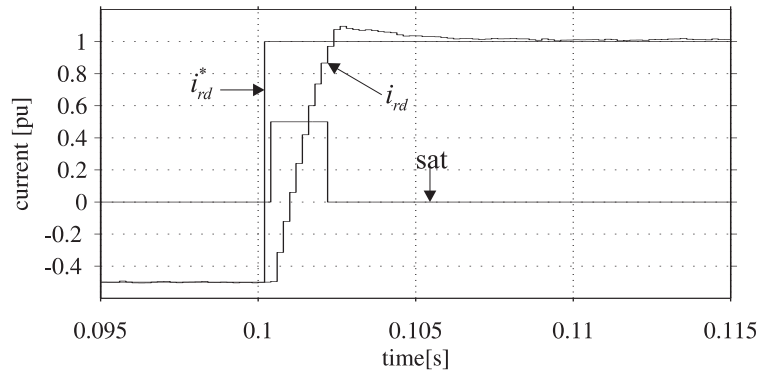


Fig. 3.8 Simulated active current response to reference active current step during VSC saturation for deadbeat current controller with no integrator anti-windup.

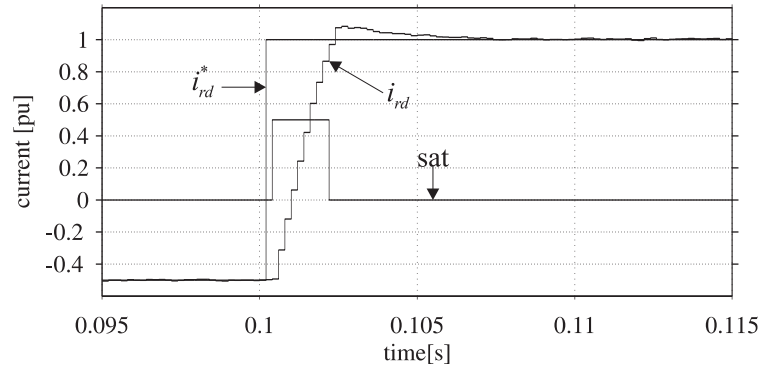


Fig. 3.9 Simulated active current response to reference active current step during VSC saturation for deadbeat current controller with integrator stop.

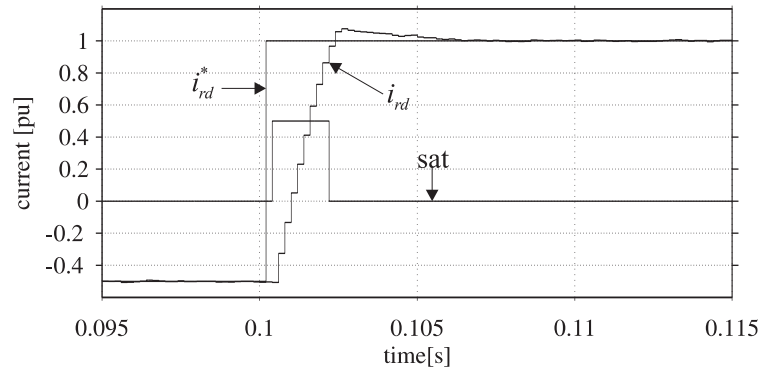


Fig. 3.10 Simulated active current response to reference active current step during VSC saturation for deadbeat current controller with back-calculation.

3.4 Stability analysis

The performance of the entire system depends on the setting of the controller parameters. Therefore, a stability analysis is important to determine the stability margin and, of course, the performance.

To ensure stability and a good damping of the system, the poles of the closed-loop system should be located in the gray area shown in Fig.3.12(a) in the continuous time domain. For a discrete system, they should be located within the gray region inside a unit circle, as shown in Fig.3.12(b) [69].

In this section, the analysis of VCC1 in case of accurate knowledge of the system parameters will be carried out. The pole location for the deadbeat VCC1 when varying the observer gain k_{psp} will be analyzed. The step response of the closed-loop system for different values of the observer gain will be shown. Furthermore, the case of inaccurate knowledge of the model parameters will be considered. The effect of an inaccurate estimation of the system parameters (and especially of the filter inductance L_r) on the dynamic performance of the closed-loop system will be investigated.

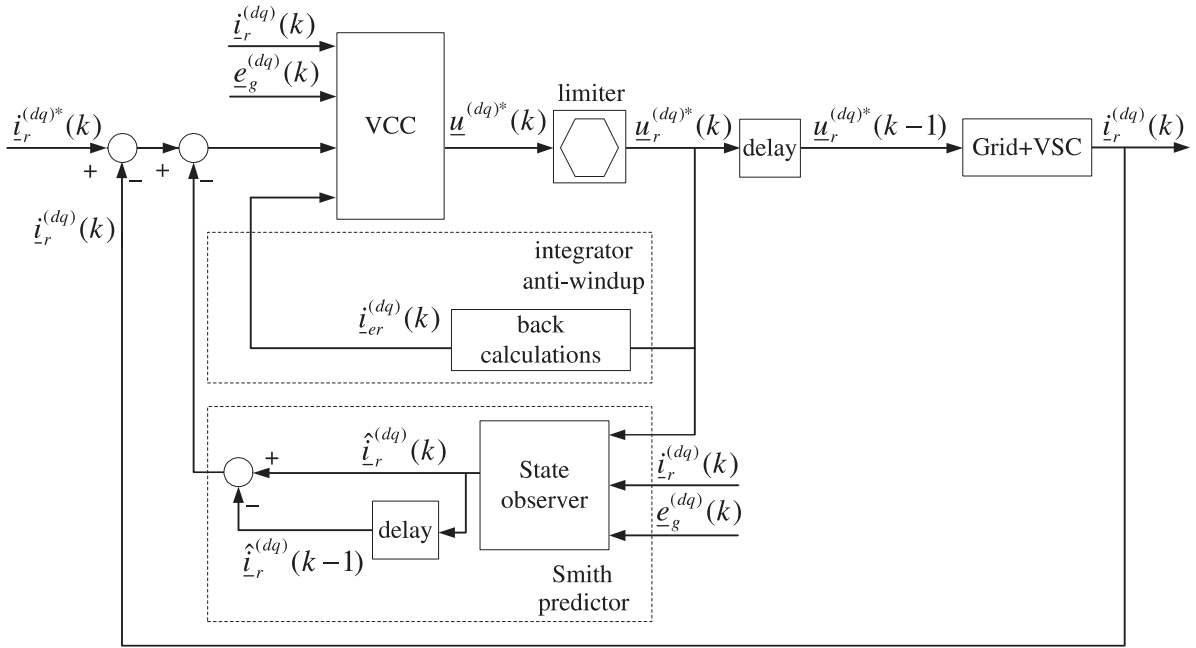


Fig. 3.11 Block scheme VCC with Smith predictor, reference voltage limitation and back-calculation.

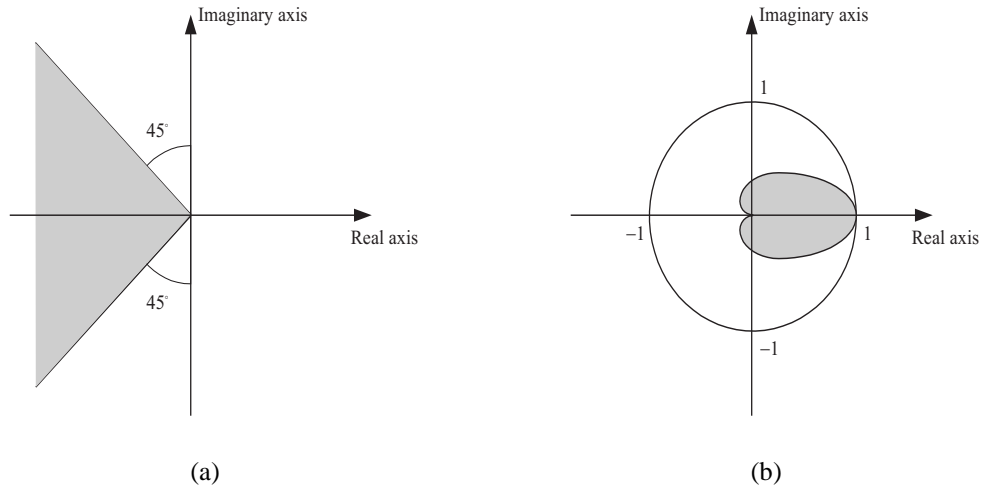


Fig. 3.12 Desired poles locus in continuous time domain, plot (a), and in discrete time domain, plot (b).

3.4.1 Accurate knowledge of model parameters

When the model parameters are known exactly, the current controller in (3.21) contains the exact values for the filter parameters and the state observer in (3.28) is the exact reproduction of the system. The measured current $i_r(k)$ and the estimated current $\hat{i}_r(k)$ should then be equal and the observer gain k_{psp} can be equal to zero. However, in a real system, due to nonlinearities and noise in the measurements, the above mentioned relation will not be true and for this reason it is necessary to introduce a non-zero gain in the state observer. Of course, this will affect the

stability and the performance of the closed-loop system.

Figure 3.13 shows the pole placement of the investigated two-sample delayed system when k_{psp} varies from 0 to 0.5, under the assumption that the vector current-controller is operating at deadbeat. As shown, when increasing the observer gain, the poles move far from the origo and the imaginary part of two complex-conjugate poles increases. For an observer gain equal to zero, two poles have a real part slightly bigger than 1 and therefore are located outside the circle boundary. If the observer gain is set equal to 0.1, the control system is stable and the poles are well damped, while for 0.3 the system is still stable, but the poles are not well damped. Finally, if the state observer gain is set to 0.5 the system gets unstable.

Figures 3.14(a) to 3.14(d) show the step response of the analyzed two-sample deadbeat current controller for $k_{\text{psp}} = 0$, $k_{\text{psp}} = 0.1$, $k_{\text{psp}} = 0.3$, and $k_{\text{psp}} = 0.5$, respectively. A unity step in the d -component of the reference current has been applied at $t = 0$ and the response of the transfer function from reference d -current to actual d -current is shown. The sampling time is $T_s = 0.2$ ms. As expected, when the observer gain is set to 0 and 0.5 the closed-loop system is unstable while for $k_{\text{psp}} = 0.1$ and $k_{\text{psp}} = 0.3$ the system is stable. As shown in Fig.3.14(a), when $k_{\text{psp}} = 0$, since two poles are located outside (but very close to) the unit circle, the oscillation is slowly increasing. If the observer gain is instead set to 0.5 (Fig.3.14(d)), two poles are located outside the unit circle and farther from the circle boundary compared with the previous case, therefore the transfer function quickly goes into instability. For $k_{\text{psp}} = 0.1$ (Fig.3.14(b)) it can be seen that at $t = 0.4$ ms, after two samples, the actual current tracks the reference, as expected for a two-sample deadbeat controller. However, the actual current is affected by a 0.1 pu overshoot, due to the cross-coupling term in the controller. If the observer gain is set to 0.3 (Fig.3.14(c)), two couples of complex and conjugate poles are outside the shadowed area

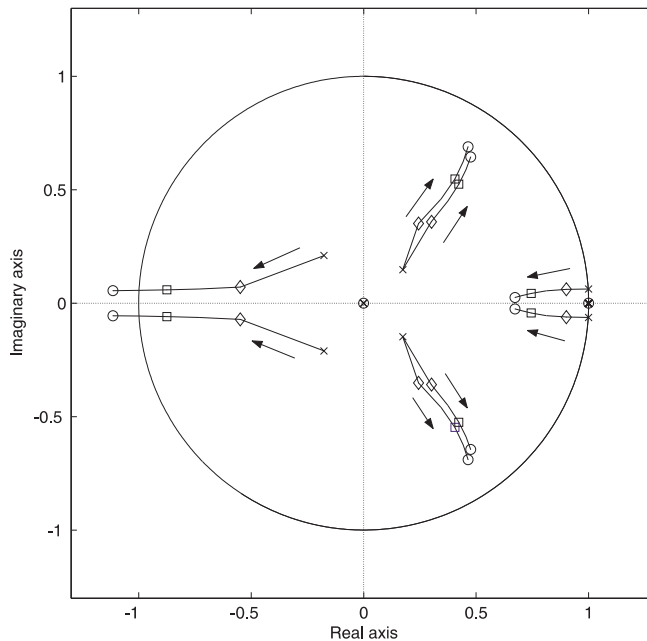


Fig. 3.13 Pole placement for accurate knowledge of system parameters at variation of observer gain. Marker “x” denotes $k_{\text{psp}} = 0$, marker “◊” denotes $k_{\text{psp}} = 0.1$, marker “□” denotes $k_{\text{psp}} = 0.3$, marker “○” denotes $k_{\text{psp}} = 0.5$.

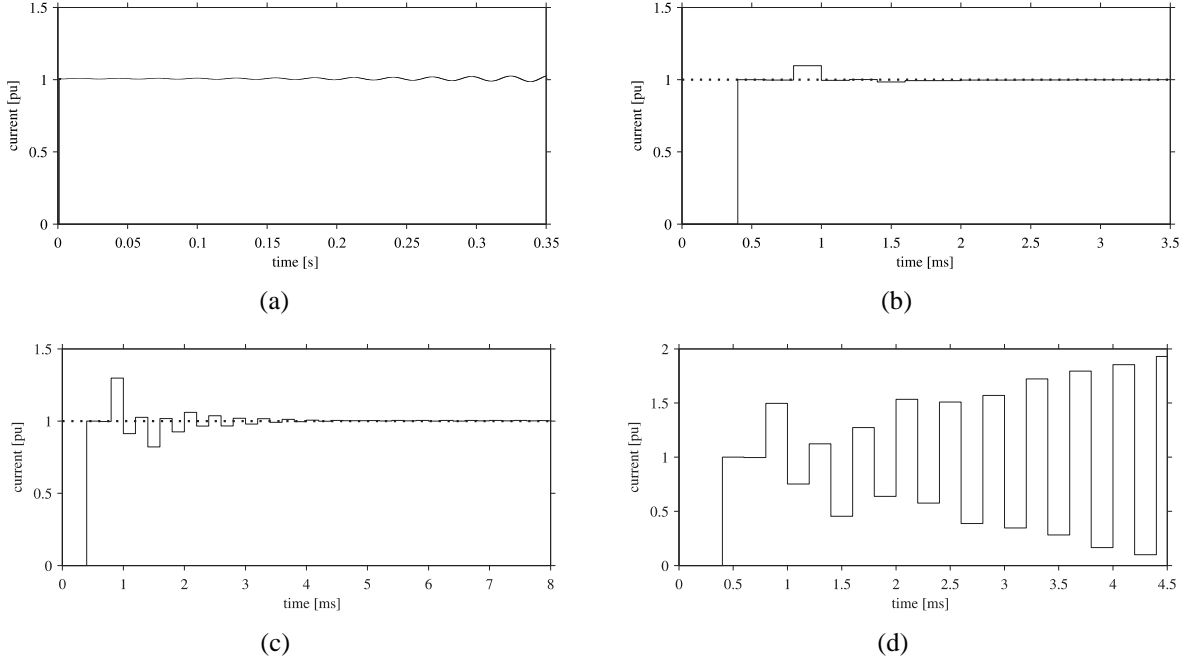


Fig. 3.14 Simulated active current step response of the VCC1 for accurate knowledge of system parameters for $k_{\text{psp}} = 0$, plot (a), $k_{\text{psp}} = 0.1$, plot (b), $k_{\text{psp}} = 0.3$, plot (c), $k_{\text{psp}} = 0.5$, plot (d).

shown in Fig.3.12(b), and the closed-loop system presents a stable oscillatory response with an overshoot of 0.3 pu.

3.4.2 Inaccurate knowledge of model parameters

For a real system, the values of the parameters are not known exactly. Moreover, some of the parameter values change during operation, due to aging or to temperature changes. Therefore, both the equation of the current controller and the equation of the state observer can be re-written considering the estimated values of the filter parameters and of the grid frequency, denoted by the superscript $\hat{\cdot}$. Calling $\hat{\varepsilon}_i^{(dq)}$ the current error, given by

$$\hat{\varepsilon}_i^{(dq)}(k) = \hat{i}_r^{(dq)*}(k) - \hat{i}_r^{(dq)}(k) - \hat{\omega}_r \hat{L}_r(k) + \hat{\omega}_r \hat{L}_r(k-1) \quad (3.34)$$

the equations for the current controller and for the state observer become

$$\begin{aligned} \hat{\underline{u}}^{(dq)*}(k) = & \hat{\underline{e}}_g^{(dq)*}(k) + \hat{R}_r \hat{i}_r^{(dq)}(k) + \mathbf{j} \frac{\hat{\omega}_r \hat{L}_r}{2} [\hat{i}_r^{(dq)*}(k) + \hat{i}_r^{(dq)}(k)] + \\ & + k_p \hat{\varepsilon}_i^{(dq)}(k) + \sum_{n=1}^k k_i \hat{\varepsilon}_i^{(dq)}(n-1) \end{aligned} \quad (3.35)$$

Chapter 3. Vector Current-controller for Grid-connected VSC

$$\begin{aligned} \hat{i}_r^{(dq)}(k+1) &= \left(1 - \frac{\hat{R}_r T_s}{\hat{L}_r} - j\hat{\omega} T_s\right) \hat{i}_r^{(dq)}(k) + \frac{T_s}{\hat{L}_r} [\underline{u}^{(dq)*}(k) - \underline{e}_g^{(dq)}(k)] + \\ &+ k_{\text{psp}} \left[\hat{i}_r^{(dq)}(k) - \hat{i}_r^{(dq)}(k) \right] \end{aligned} \quad (3.36)$$

where the proportional and the integral gain of the current controller are now equal to

$$k_p = \frac{\hat{L}_r}{T_s} + \frac{\hat{R}_r}{2}, \quad k_i = k_p \frac{T_s}{T_i} = k_p \frac{T_s \hat{R}_r}{\hat{L}_r} \quad (3.37)$$

From the results obtained in the previous analysis, an observer gain equal to 0.1 has been chosen.

Since the filter resistance is usually negligible compared with its reactance, the response of the closed-loop system is insensitive to its variation. The system is instead sensitive to variations of the filter inductance. Figures 3.15(a) to 3.15(c) show the pole placement of the closed-loop system when the estimated filter inductance \hat{L}_r varies from 60% to 140% of the actual filter inductance L_r , for $k_{\text{psp}} = 0.1$. The trajectory of some poles has been plotted separately for clarity. From this figure, it is possible to observe that an underestimation of L_r results in a well-damped closed-loop system, while when the estimated inductance increases, the poles move far from the real axis. Therefore, it can be concluded that, in order to obtain a well-damped system, it is better to underestimate the filter inductance \hat{L}_r . According with the analysis carried out, the inductance has to be underestimated by 90% ($\hat{L}_r = 0.1 L_r$) for the system to go into instability, which in practice means that it will never happen.

To validate these results, the step response of VCC when $\hat{L}_r = 0.6 L_r$ and when $\hat{L}_r = 1.4 L_r$ has been analyzed and is shown in Figs.3.16(a) and 3.16(b), respectively. As expected, when the filter inductance is underestimated the system is well damped, while the overestimated filter inductance provides an oscillatory step response with an initial overshoot of 0.4 pu.

Finally, the sensitivity of the closed-loop system to variations of the grid frequency has been investigated. The estimated grid frequency has been varied by $\pm 20\%$ of the nominal frequency (50 Hz). The pole locus of the deadbeat VCC1 for $k_{\text{psp}} = 0.1$, shown in Fig.3.17, when the estimated grid frequency \hat{f} is varied, shows that the system can be considered insensitive to normal variations of the grid frequency. This is due to the fact that the estimated frequency affects only the cross-coupling term of the current controller (see (3.35)).

3.4. Stability analysis

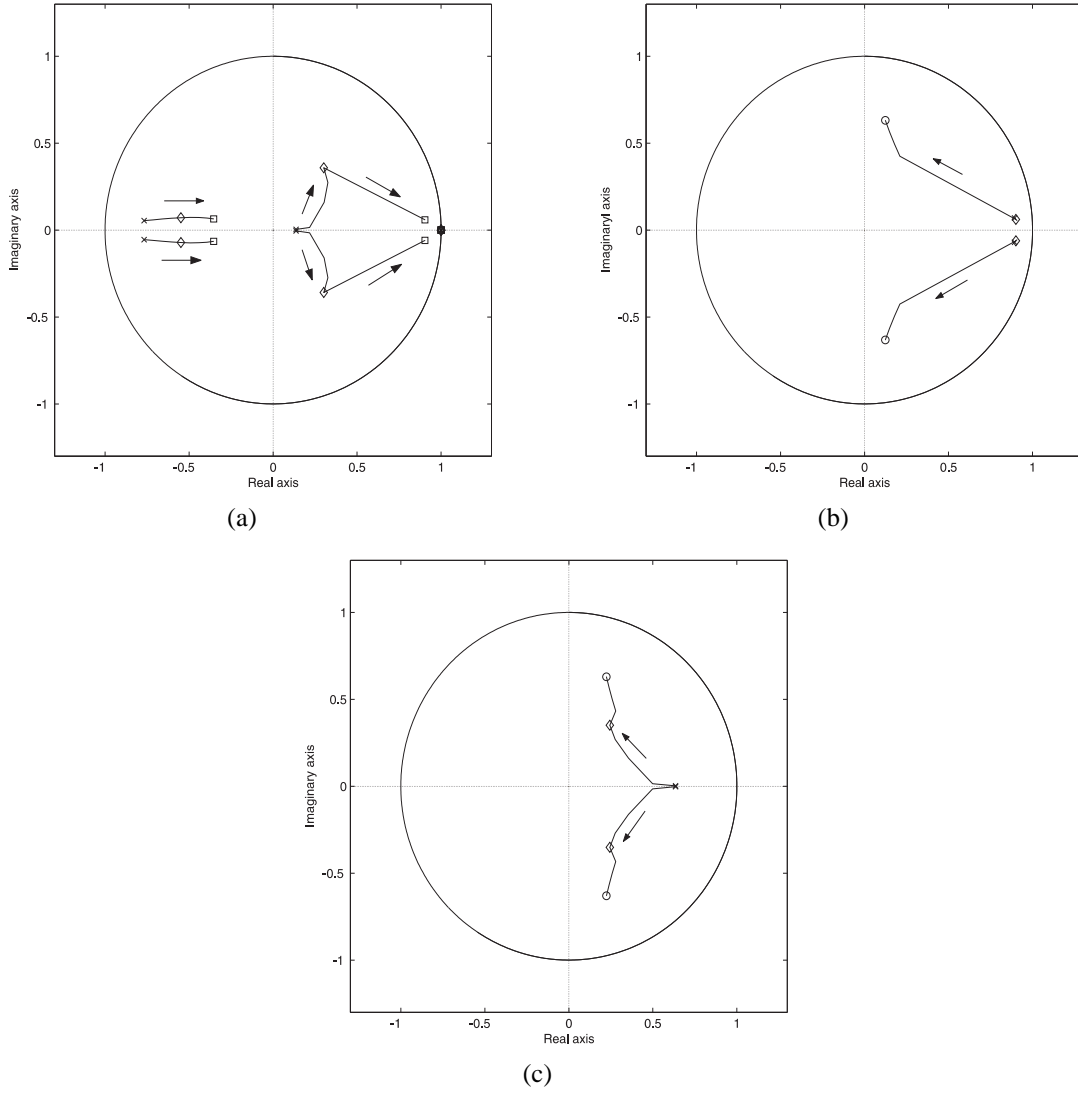


Fig. 3.15 Pole placement for inaccurate knowledge of the system parameters for $k_{\text{psp}} = 0.1$ at the variation of the estimated filter inductance. Marker “ \times ” denotes $\hat{L}_r = 0.6L_r$, marker “ \diamond ” denotes $\hat{L}_r = L_r$, marker “ \circ ” denotes $\hat{L}_r = 1.4L_r$. Plots (a), (b) and (c) are part of the same plot.

Chapter 3. Vector Current-controller for Grid-connected VSC

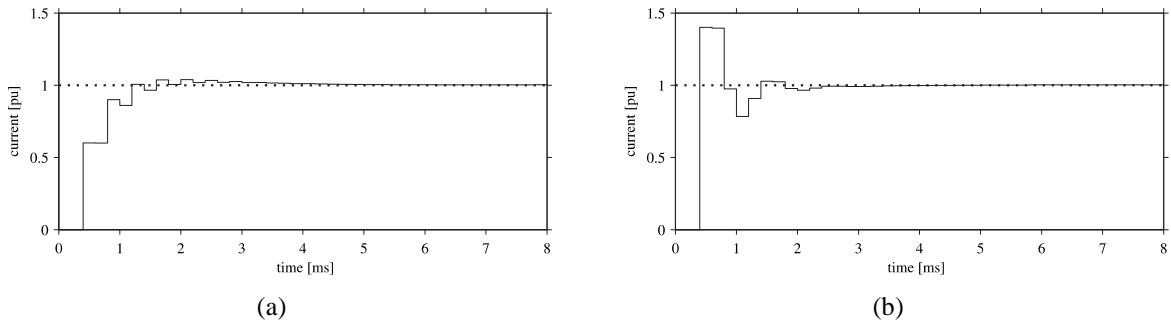


Fig. 3.16 Simulated active current step response of the VCC1 for $k_{\text{psp}} = 0.1$ and for $\hat{L}_r = 0.6L_r$, plot (a), and $\hat{L}_r = 1.4L_r$, plot (b).

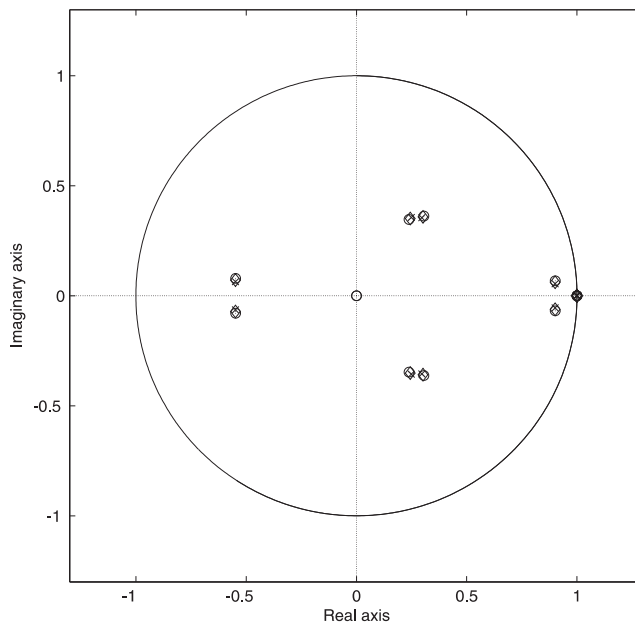


Fig. 3.17 Pole placement for inaccurate knowledge of the system parameters for $k_{\text{psp}} = 0.1$ at the variation of the estimated grid frequency. Marker “ \times ” denotes $\hat{f} = 40\text{Hz}$, marker “ \diamond ” denotes $\hat{f} = 50\text{Hz}$, marker “ \circ ” denotes $\hat{f} = 60\text{Hz}$.

3.5 Experimental results

The investigated deadbeat VCC1 has been tested both via simulations, using the simulation program PSCAD/EMTDC, and experimentally on a VSC system that has been built in the Power Systems Laboratory at the Department of Energy and Environment at Chalmers University. In Paper III, the dynamic performance of the VCC1 under balanced and unbalanced conditions of the grid voltage is shown. Furthermore, in Paper IV, the dynamic performance of the VCC1 under symmetrical and unsymmetrical voltage dips is reported.

As an example, Fig.3.18 shows the current response of the VCC1 to a reactive current step under balanced (left) and unbalanced (right) conditions of the grid voltage. From the figure it is possible to observe that when the grid voltage is balanced, the VCC1 works properly and the actual current follows the reference one in two samples. On the contrary, the controller presents unsatisfactory performance under unbalanced conditions. As shown in the figure, in case of unbalanced conditions of the grid voltage, the filter current will exhibit an oscillatory response having characteristic frequency equal to double the power frequency. These oscillations are due to the presence of a negative-sequence component in the PCC voltage due to the unbalanced conditions.

To cope with unbalanced conditions, the VCC has been further improved. Using a delay-based estimation algorithm (denoted as delayed signal cancellation, see [40] and Papers I and II), positive- and negative-sequence components of the measured voltage and current are estimated and used in the control algorithm. By feeding the VCC1 controller only with the positive-sequence component of the grid voltage, the response is improved and the filter current follows the reference with almost no delay. This control strategy is addressed to as Vector Current-controller type 2 (VCC2).

The controller can be further improved to be able to control also the negative-sequence component of the filter current. Positive- and negative-sequence components of voltage and current are sent to two separate current controllers. The resulting control algorithm is addressed to as Dual Vector Current-controller (DVCC). In this case, it is shown that the current presents a

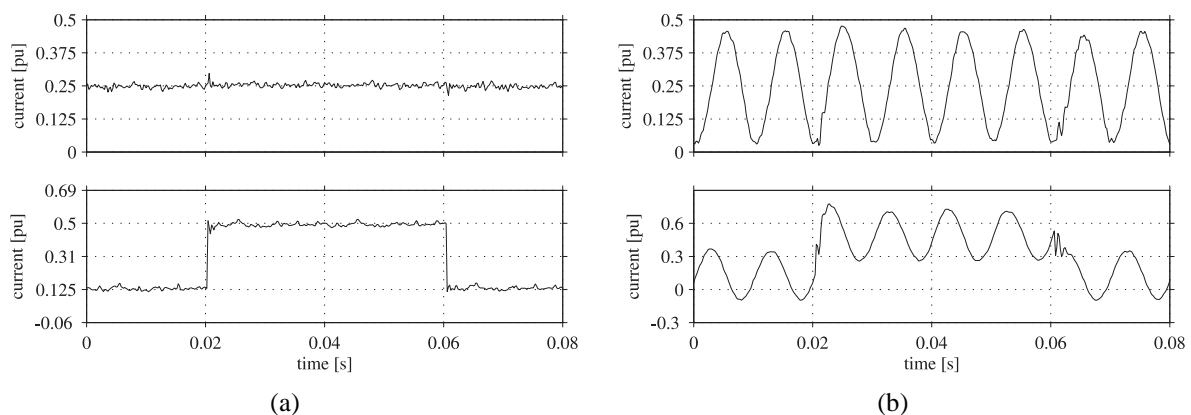


Fig. 3.18 Measured current response to reference reactive current step. Plot (a): balanced grid voltage; plot (b): unbalanced grid voltage.

more sluggish response as compared with the VCC2, mostly due to the delay introduced by the sequence separation.

3.6 Conclusions

In this chapter, a deadbeat vector current-controller for grid-connected VSCs has been derived. To take into account the one sample delay due to the computational time and the voltage ratings of the VSC, the controller has been improved by using a Smith predictor. Furthermore, reference voltage limitation and anti-windup function to prevent integrator windup has been added in the control algorithm. Stability analysis in case of accurate and in the realistic case of inaccurate knowledge of the system parameters has been carried out. Finally, experimental results of the investigated controller under balanced and unbalanced conditions of the grid voltage have been presented. With a constant dc-link voltage, steps in the reference currents have been applied in order to test the dynamic performance of the system. It has been demonstrated that, using Vector Current-controller type 1 (VCC1), designed by only considering positive-sequence components, the dq -currents under unbalanced grid voltage are affected by an oscillation at double the power frequency. Better transient performance can be obtained by feeding the same controller only the positive-sequence component of the grid voltage in the Vector Current-controller type 2 (VCC2). The Dual Vector Current-controller (DVCC), where both voltages and currents are separated into their sequence components and two separate current controllers are used, showed a slower response compared with VCC2 response, due to the time required for the phase sequences estimation. Since it presents a fast response and can operate properly both under balanced and unbalanced conditions of the grid voltage, the VCC2 seems to be the most suitable option for control of shunt-connected VSC. Nevertheless, as it will be discussed in the next chapter, in some applications where the current controller is used as inner loop of a cascade controller, control of both positive and negative sequences of the filter current might be needed, thus DVCC has to be used.

Chapter 4

Control of Series-connected VSC for Voltage Dip Mitigation

In this chapter, the controller for the series-connected VSC for voltage dips mitigation will be presented. Improvements to the derived control system to be able to mitigate unbalanced voltage dips will be described. Experimental results are reported in Paper V.

4.1 Introduction

In Chapter 2, the principle and typical configuration of the series-connected VSC, or SSC, have been reviewed. This chapter deals with the control of the SSC for voltage dip mitigation. The control of the SSC for mitigation of voltage dips has been treated, among others, in [50] and [8]. Reference [50] presents the design and control of a full-size series compensator for medium voltage applications. With the configuration adopted, based on three H-bridges sharing the same dc link, individual control of each phase is possible, which is advantageous for compensation of unbalanced dips. The drawback is that double the amount of valves are required compared to a VSC. Reference [8] develops a cascade controller, based on an inner current controller and an outer voltage controller. However, in [8] the problem of saturation of the VSC current controller due to limited dc-link voltage is not investigated.

In this chapter, the derivation of a cascade controller to control the SSC to mitigate voltage dips will be presented. An extended analysis of the control system will be carried out. Experimental results of the SSC using the proposed cascade controller under balanced and unbalanced voltage dips will be presented.

4.2 Layout of the SSC

The three-phase diagram of a grid with SSC is displayed in Fig.4.1. The three-phase voltages of the grid are denoted by $e_{s,a}(t)$, $e_{s,b}(t)$ and $e_{s,c}(t)$, while the grid voltages at the PCC and the

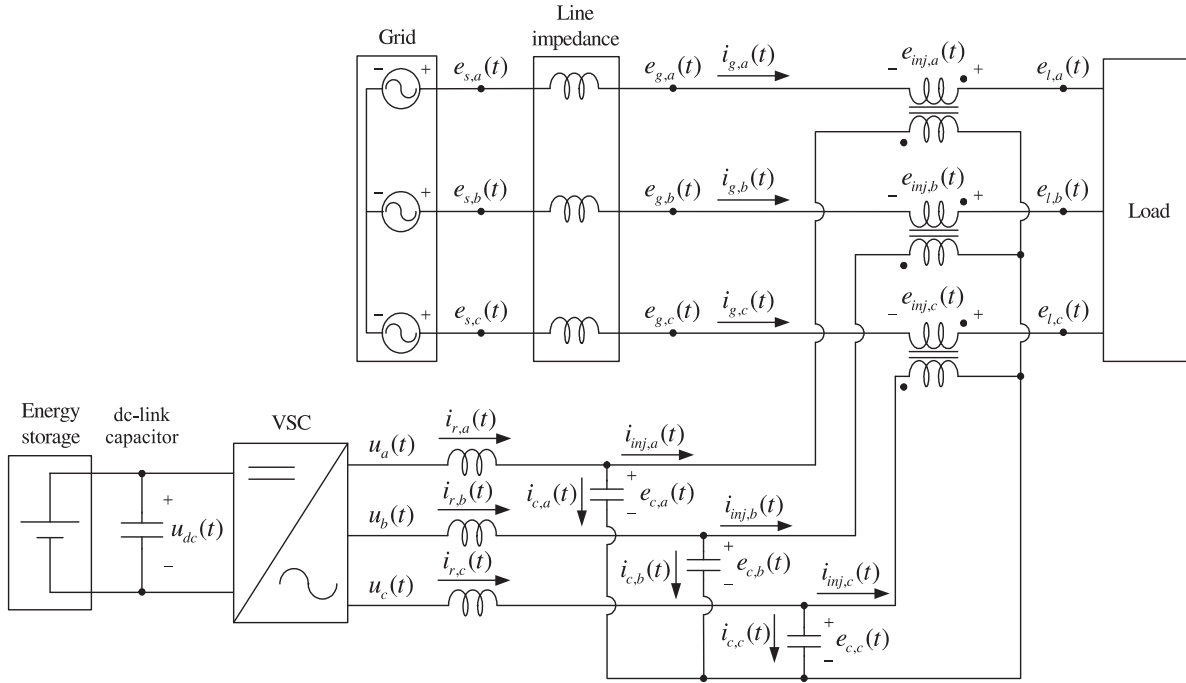


Fig. 4.1 Three-line diagram of grid with SSC.

grid currents are denoted by $e_{g,a}(t)$, $e_{g,b}(t)$, $e_{g,c}(t)$ and $i_{g,a}(t)$, $i_{g,b}(t)$ and $i_{g,c}(t)$, respectively. The three-phase voltages and currents of the VSC are denoted by $u_a(t)$, $u_b(t)$, $u_c(t)$ and $i_{r,a}(t)$, $i_{r,b}(t)$ and $i_{r,c}(t)$, respectively. The filter capacitor voltages and currents are denoted by $e_{c,a}(t)$, $e_{c,b}(t)$, $e_{c,c}(t)$ and $i_{c,a}(t)$, $i_{c,b}(t)$ and $i_{c,c}(t)$, respectively. The voltages and currents injected by the SSC are denoted by $e_{inj,a}(t)$, $e_{inj,b}(t)$, $e_{inj,c}(t)$ and $i_{inj,a}(t)$, $i_{inj,b}(t)$ and $i_{inj,c}(t)$, respectively. The dc-link voltage is denoted by $u_{dc}(t)$. Finally, the load voltages are denoted by $e_{l,a}(t)$, $e_{l,b}(t)$ and $e_{l,c}(t)$.

It can be noticed that, as a difference compared with the shunt-connected VSC, the SSC is equipped with an LC-filter, placed at the output of the VSC. This filter is installed in order to remove both current and voltage harmonics, thus reducing the harmonic pollution in the injected voltage. Moreover, this reduces the ripple present in the voltage applied to the windings of the injection transformer, which in turn lengthens the transformer lifetime. As for the L-filter used for the shunt-connected VSC, the inductance smoothes the current output of the VSC, thus reducing the current ripple and therefore the stress on the valves of the VSC.

The cut-off frequency of the filter determines the amount of harmonics injected in the grid by the SSC and thereby the harmonic content of the load voltage. This should be considered if the load is particularly sensitive. A basic rule in the design of the filter is that its cut-off frequency should be much lower than the switching frequency of the VSC, thus eliminating the switching ripple in the output voltage. However, the filter should not affect the fundamental component of the injected voltage. Here, the cut-off frequency of the LC-filter has been set to 460 Hz.

The SSC injects the required missing load voltage into the grid through three single-phase transformers. The rated power of the injection transformers is dictated by the rated current of the load, which continuously flows in the winding that is connected to the feeder, and by the

4.3. Dual Vector-controller type 1 (DVC1)

TABLE 4.1. SYSTEM PARAMETERS FOR SSC.

Grid parameters			
Grid voltage	E	400 V	1 pu
Grid current	I	40 A	1 pu
Grid frequency	f	50 Hz	
Load resistance	R_l	10 Ω	1 pu
Load inductance	L_l	23.9 mH	0.75 pu
dc-link voltage	U_{dc}	600 V	1.5 pu
Filter parameters			
Filter resistance	R_r	24.8 m Ω	0.0025 pu
Filter inductance	L_r	2 mH	0.063 pu
Filter capacitor	C	60 μ F	0.18 pu
Transformer parameters			
Rated power	S_n	10 kVA	1.08 pu
Rated voltage	V_n	230 V	1 pu
Short-circuit power	P_{cc}	141 W	0.015 pu
Short-circuit voltage	V_{cc}	5.3 V	0.023 pu

maximum voltage to be injected. Here, the injection transformers are designed for full-voltage injection.

System parameters, reported in Table 4.1, are those of a SSC prototype built in the Power System Laboratory of the Department of Energy and Environment at Chalmers University.

4.3 Dual Vector-controller type 1 (DVC1)

The control system of the SSC investigated for this thesis is constituted by two closed-loop controllers connected in cascade: an outer loop that controls the voltage across the filter capacitor $e_c(t)$ and an inner controller that controls the current through the filter reactor $i_r(t)$ [9]. The basic assumption behind the investigated control strategy is that the injected voltage is equal to the voltage across the capacitors. This is equivalent of assuming that the injection transformer is ideal with a 1:1 turn ratio, meaning that

$$e_{inj,a}(t) = e_{c,a}(t) \quad (4.1)$$

$$i_{inj,a}(t) = i_{g,a}(t) \quad (4.2)$$

and analogously for the other two phases. Under these assumptions, applying the Kirchhoff's current law to the LC-filter, the following differential equations for the three phases can be written

$$i_{r,a}(t) = i_{c,a}(t) + i_{g,a}(t) = C \frac{d}{dt} e_{c,a}(t) + i_{g,a}(t) \quad (4.3)$$

$$i_{r,b}(t) = i_{c,b}(t) + i_{g,b}(t) = C \frac{d}{dt} e_{c,b}(t) + i_{g,b}(t) \quad (4.4)$$

$$i_{r,c}(t) = i_{c,c}(t) + i_{g,c}(t) = C \frac{d}{dt} e_{c,c}(t) + i_{g,c}(t) \quad (4.5)$$

By applying Clarke's transformation, (4.3) to (4.5) can be written in the $\alpha\beta$ -coordinate system as

$$\frac{d}{dt} \underline{e}_c^{(\alpha\beta)}(t) = \frac{1}{C} \underline{i}_r^{(\alpha\beta)}(t) - \frac{1}{C} \underline{i}_g^{(\alpha\beta)}(t) \quad (4.6)$$

which, by using $\alpha\beta$ - to dq -transformation with a PLL synchronized with the grid voltage vector, becomes

$$\frac{d}{dt} \underline{e}_c^{(dq)}(t) = \frac{1}{C} \underline{i}_r^{(dq)}(t) - \frac{1}{C} \underline{i}_g^{(dq)}(t) - j\omega \underline{e}_c^{(dq)}(t) \quad (4.7)$$

4.3.1 Voltage controller

As for the VCC described in Section 3.2, the voltage controller is meant to be implemented in a digital controller. Thus, it is necessary to discretize (4.7). Again, this is done by integrating the equation over one sample period T_s and then dividing by T_s , thus obtaining

$$\begin{aligned} \frac{1}{T_s} [\underline{e}_c^{(dq)}(k+1) - \underline{e}_c^{(dq)}(k)] &= \frac{1}{C} \underline{i}_r^{(dq)}(k, k+1) - \frac{1}{C} \underline{i}_g^{(dq)}(k, k+1) + \\ &\quad - j\omega \underline{e}_c^{(dq)}(k, k+1) \end{aligned} \quad (4.8)$$

where $\underline{e}_c^{(dq)}(k, k+1)$ denotes the average value of $\underline{e}_c^{(dq)}(t)$ between sample k and sample $k+1$.

If a proportional controller with deadbeat gain is used, the controller will track the reference voltage with one sample delay, yielding

$$\underline{e}_c^{(dq)}(k+1) = \underline{e}_c^{(dq)*}(k) \quad (4.9)$$

The reference capacitor voltage is the voltage to be injected in the grid to restore the load voltage to the desired value

$$\underline{e}_c^{(dq)}(k) = \underline{e}_l^{(dq)*}(k) - \underline{e}_g^{(dq)}(k) \quad (4.10)$$

where $\underline{e}_l^{(dq)*}$ denotes the load reference voltage in the dq -coordinate system.

The following assumptions are made in order to formulate the voltage controller:

- The grid current components change slowly and are considered constant over one sample period

$$\underline{i}_g^{(dq)}(k, k+1) = \underline{i}_g^{(dq)}(k) \quad (4.11)$$

4.3. Dual Vector-controller type 1 (DVC1)

- The filter capacitor voltage changes linearly during one sample period

$$\underline{e}_c^{(dq)}(k, k+1) = \frac{1}{2} \left[\underline{e}_c^{(dq)}(k) + \underline{e}_c^{(dq)}(k+1) \right] = \frac{1}{2} \left[\underline{e}_c^{(dq)}(k) + \underline{e}_c^{(dq)*}(k) \right] \quad (4.12)$$

- The average value of the filter current over one sample period is equal to the reference

$$\underline{i}_r^{(dq)}(k, k+1) = \underline{i}_r^{(dq)*}(k) \quad (4.13)$$

The proportional voltage controller can now be formulated as

$$\begin{aligned} \underline{i}_r^{(dq)*}(k) &= \underline{i}_g^{(dq)}(k) + j \frac{\omega C}{2} \left[\underline{e}_c^{(dq)*}(k) + \underline{e}_c^{(dq)}(k) \right] + \\ &+ \frac{C}{T_s} \left[\underline{e}_c^{(dq)*}(k) - \underline{e}_c^{(dq)}(k) \right] = \underline{i}_{ff}^{(dq)}(k) + k_{p,vc} \left[\underline{e}_c^{*(dq)}(k) - \underline{e}_c^{(dq)}(k) \right] \end{aligned} \quad (4.14)$$

where $\underline{i}_{ff}^{(dq)}(k)$ is the feed-forward term, while $k_{p,vc}$ is the proportional gain of the voltage controller to obtain deadbeat and is equal to

$$k_{p,vc} = \frac{C}{T_s} \quad (4.15)$$

Observe that here the filter capacitor is assumed ideal, i.e. the current flowing into the capacitor will not produce power losses (capacitor's resistance equal to zero). Under this assumption, the deadbeat equations will lead to a proportional controller only. However, in order to remove the steady state error due to unavoidable mismatch between the actual and the modelled system, it is convenient to add a small integral term in the control law. Thus, the PI-controller can be formulated as

$$\underline{i}_r^{*(dq)}(k) = \underline{i}_{ff}^{(dq)}(k) + k_{p,vc} \left[\underline{e}_c^{*(dq)}(k) - \underline{e}_c^{(dq)}(k) \right] + \Delta \underline{i}_i^{(dq)}(k) \quad (4.16)$$

with $\Delta \underline{i}_i^{(dq)}(k)$ the integral term at sample k , given by

$$\Delta \underline{i}_i^{(dq)}(k) = \Delta \underline{i}_i^{(dq)}(k-1) + k_{i,vc} \left[\underline{e}_c^{*(dq)}(k-1) - \underline{e}_c^{(dq)}(k-1) \right] \quad (4.17)$$

where, calling $T_{i,vc}$ the integration time constant, the integral gain of the voltage controller $k_{i,vc}$ is given by

$$k_{i,vc} = k_{p,vc} \frac{T_s}{T_{i,vc}} \quad (4.18)$$

The output of the voltage controller is the reference current $\underline{i}_r^{(dq)*}$, which will be the input to the current controller in order to control the current through the filter reactor $\underline{i}_r^{(dq)}$. The current controller used is VCC1, described in Section 3.3. Figure 4.2 shows the block scheme of the implemented cascade controller, constituted by the described voltage controller (denoted in the figure by VC) in series with VCC1. The algorithm of the implemented control system can be summarized as:

Chapter 4. Control of Series-connected VSC for Voltage Dip Mitigation

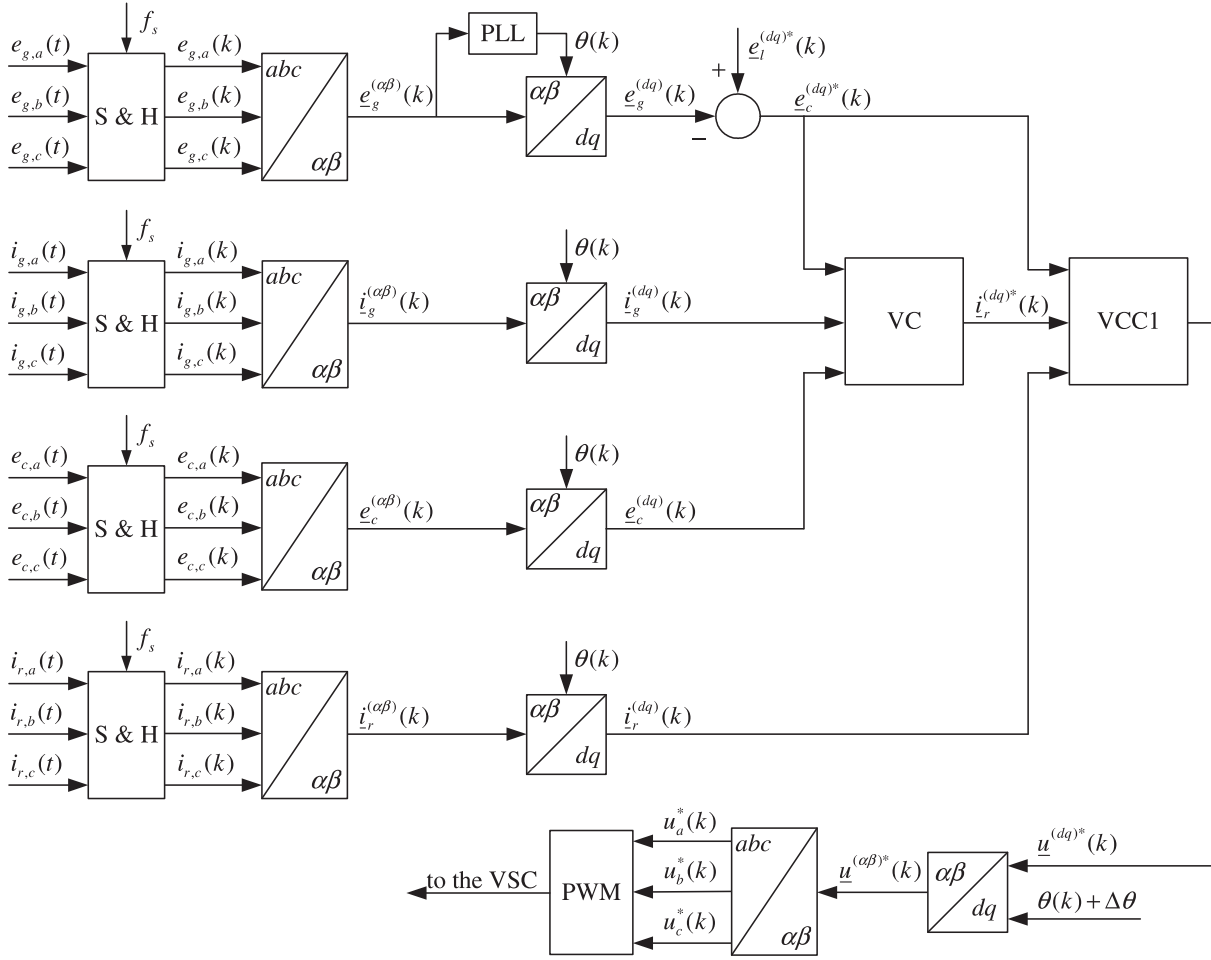


Fig. 4.2 Block-scheme of implemented cascade controller for voltage dip mitigation using SSC.

1. Measure and sample the grid voltages, grid currents, filter currents and capacitor voltages with sampling frequency f_s ;
2. Transform all three-phase quantities to the $\alpha\beta$ -coordinate system and then to the rotating dq -coordinate system, using the transformation angle θ , obtained from the PLL;
3. Calculation of the reference filter current $i_r^{(dq)*}(k)$ using the VC block;
4. Calculation of the reference voltage $u^{(dq)*}(k)$ using the VCC1 block;
5. Convert the reference voltages from the dq -coordinate system into three-phase voltages using the transformation angle $\theta(k) + \Delta\theta$, where $\Delta\theta = 3/2 \omega T_s$, as explained in Section 3.3.1;
6. Calculate the duty-cycles in the PWM block and send the switching signals to the VSC valves.

4.3.2 Stability analysis

In this section, the stability analysis of the entire system using DVC1 (= DVCC + VCC1) will be presented. The dynamic performance of the two closed-loop systems in both cases of accurate and inaccurate knowledge of the filter parameters will be investigated. System parameters are displayed in Table 4.1. A block diagram of the complete closed-loop system used for this investigation is depicted in Fig.4.3, where the VSC has been considered as an ideal amplifier. Note that the load dynamics are included in the scheme. Here, an RL-load has been considered. Thus, the load current will change when the load voltage changes.

Accurate knowledge of filter parameters

In case of accurate knowledge of the filter parameters, both the equations of the VC and of the VCC1 contain the exact values of the parameters. In this case, it is of interest to investigate the interaction between the two controllers. When a cascade controller is used, it is important to carefully select the bandwidth of the two controllers in order to ensure the stability of the entire system. Figure 4.4 shows the closed-loop poles placement of the SSC with DVC1 for different values of the voltage controller gain (denoted as α_{vc} and expressed in per unit of the deadbeat gain of the voltage controller, C/T_s). The inner current controller is set to deadbeat. When increasing the gain of the outer controller, the poles move out from the real axis. It can be observed that, for α_{vc} equal to 0.1 and 0.3, the closed-loop system is stable, while for α_{vc} equal to 1 (i.e. both voltage controller and current controller at deadbeat) the closed-loop system is unstable. When the outer controller gain α_{vc} is set to 0.57 of deadbeat the system is at the stability limit.

From this analysis it is possible to understand one of the basic rules for selecting the parameters of a cascade controller: the inner loop should be much faster than the outer one. Typically, the ratio between the bandwidth of the inner controller and that of the outer controller should be at least 5 [68].

Inaccurate knowledge of filter parameters

When the filter parameters are not known with accuracy, estimated values for the filter reactor (\widehat{R}_r and \widehat{L}_r) and filter capacitor (\widehat{C}) are used in the equations of the VCC1 and of the VC. The

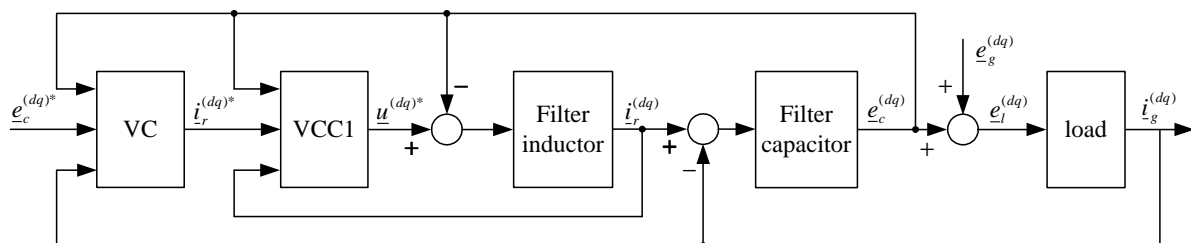


Fig. 4.3 Block diagram of closed-loop system constituted by DVC1, filter and load.

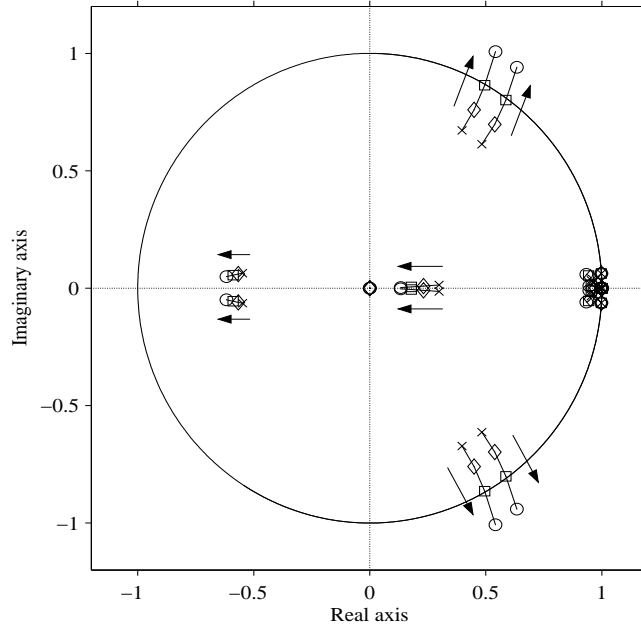


Fig. 4.4 Pole placement for accurate knowledge of filter parameters when varying voltage controller gain α_{vc} . Marker “x” denotes $\alpha_{vc} = 0.1$ pu deadbeat, marker “o” denotes $\alpha_{vc} = 0.3$ pu deadbeat, marker “□” denotes $\alpha_{vc} = 0.57$ pu deadbeat, marker “o” denotes $\alpha_{vc} =$ deadbeat.

VCC1 is still set to deadbeat, while, according with the results obtained in the previous analysis, α_{vc} has been set to 30% of deadbeat.

The reactor resistance is usually negligible compared with its reactance, therefore the response of the system can be considered insensitive to its variation. Figure 4.5 shows the closed-loop poles of the SSC with DVC1 when the estimated filter inductance \hat{L}_r varies from 60% to 180% of the actual filter inductance L_r . From this figure it is possible to observe that an underestimation of the filter inductance \hat{L}_r results in a well damped system. When increasing \hat{L}_r , some poles move far from the real axis and for \hat{L}_r equal to 180% of L_r the system gets unstable. Therefore, similarly to what was found in Section 3.4, it can be concluded that it is better to underestimate the filter inductance from the stability point of view.

Figure 4.6 shows the closed-loop poles of the control system when the estimated filter capacitor \hat{C} varies from 60% to 180% of the actual filter capacitor C . As shown, the poles slowly move far from the real axis when increasing \hat{C} , but always remain inside the unit circle. Therefore, it can be concluded that, when the filter capacitor is underestimated, the control system results more damped than in case of overestimation, but in general it is less sensitive to variations of the filter capacitor C compared with variations of the filter inductor L_r . This is not surprising, since the filter capacitor appears in the equations of the VC only, which has reduced bandwidth as compared with the VCC1.

4.3. Dual Vector-controller type 1 (DVC1)

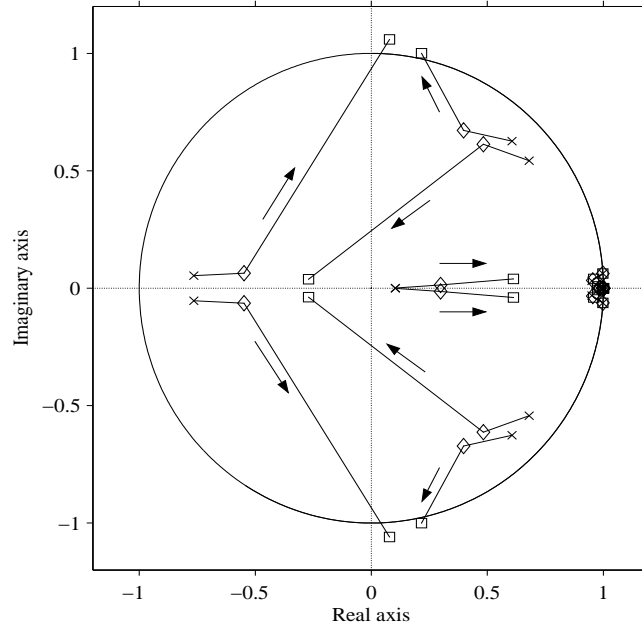


Fig. 4.5 Pole placement for inaccurate knowledge of filter parameters for $\alpha_{vc} = 0.3$ when varying estimated filter inductance. Marker “x” denotes $\hat{L}_r = 0.6L_r$, marker “◇” denotes $\hat{L}_r = L_r$, marker “□” denotes $\hat{L}_r = 1.8L_r$.

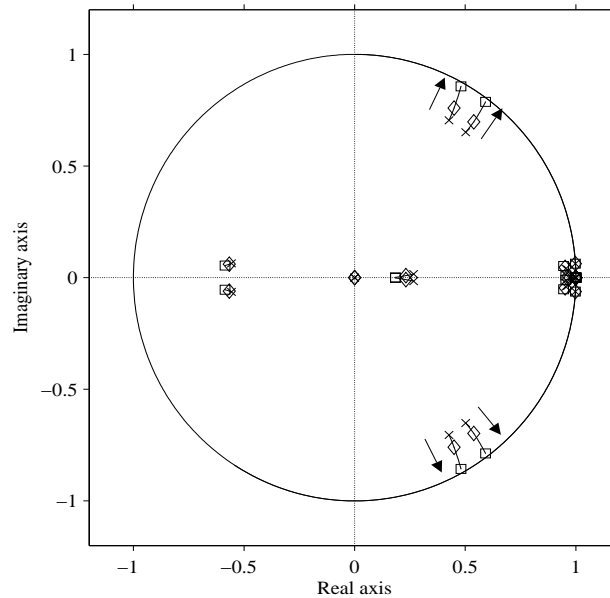


Fig. 4.6 Pole placement for inaccurate knowledge of filter parameters for $\alpha_{vc} = 0.3$ at variation of estimated filter capacitor. Marker “x” denotes $\hat{C} = 0.6C$, marker “◇” denotes $\hat{C} = C$, marker “□” denotes $\hat{C} = 1.8C$.

4.4 Experimental results

In this section, experimental results of the SSC with DVC1 will be presented. The laboratory setup used for these experiments is described in Paper V. Here, a short summary of the obtained results will be given.

A first set of tests has been carried out when the grid voltage is affected by a balanced voltage dip. The three-phase grid voltages are depicted in Fig.4.7. As shown, a symmetrical voltage dip with 71% remaining voltage occurs at $t = 0.03$ s and lasts for 300 ms. From the grid voltage in dq -coordinates in Fig.4.8, it can be noticed that the q -component is affected by a transient at the beginning and at the end of the dip. This is due to the phase-angle jump associate to the dip and to the response time of the PLL, which takes about 0.03 s to lock into the new angle of the voltage vector. After these transients, the q -voltage is constant at zero.

When the dip occurs, the VSC reacts to the voltage variation to keep the load voltage at its rated value. As a results, the SSC mitigates the voltage dip and keeps the load voltage at the pre-fault value, as shown by the three-phase load voltages in Fig.4.9 and by the dq -components of the load voltage shown in Fig.4.10. Only a small transient at the beginning and at the end of the dip can be noticed.

The same controller has also been tested under the unbalanced voltage dip in Fig.4.11. In this case, the network is affected by a voltage dip with 85% remaining positive-sequence voltage and negative-sequence unbalance of 10.9%, starting at $t = 0.03$ s and with duration of 300 ms. Due to the unbalance, the dq -voltages of the grid, shown in Fig.4.12, are affected by a 100 Hz oscillation with an amplitude of 0.2 pu (peak-to-peak). The system reacts to the dip trying to inject the missing voltage into the grid. However, it can be seen from the three-phase voltages in Fig.4.13 that the load voltage is not perfectly restored to the pre-fault value. Some unbalance is still present. This is confirmed by the corresponding dq -components shown in Fig.4.14, which oscillate slightly with the frequency of 100 Hz.

As for the experimental results obtained for the VCC1 shown in the previous chapter, this is due to the fact that the control system is implemented in a dq -frame, or synchronous reference frame (SRF), that is synchronized with the positive-sequence component of the grid voltage, without

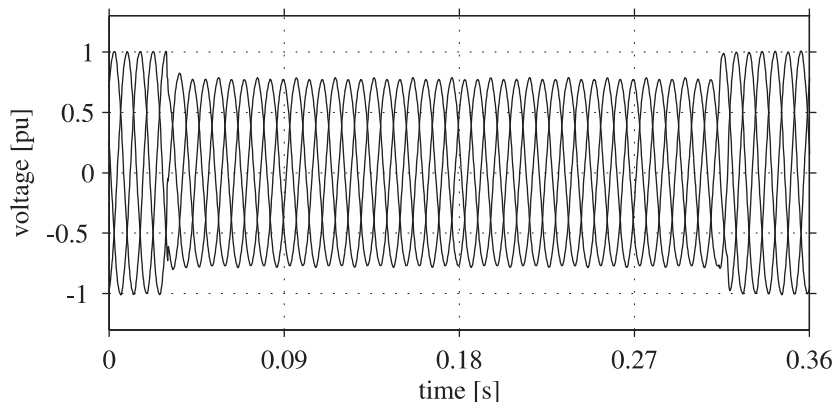


Fig. 4.7 Measured three-phase grid voltages during 70% balanced voltage dip.

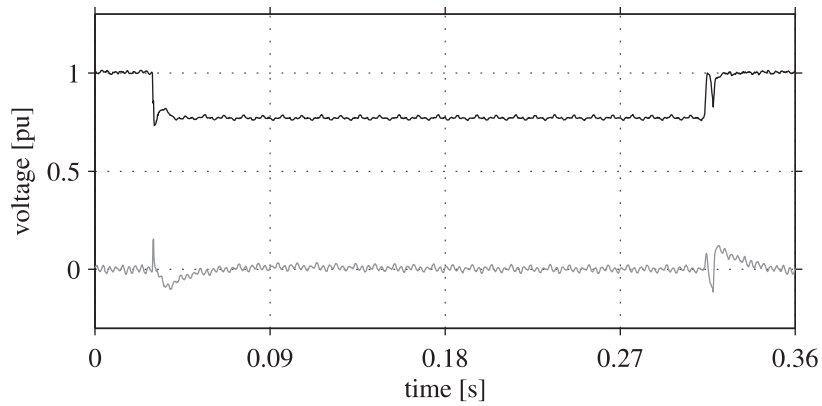


Fig. 4.8 Measured grid voltage in dq -frame during 70% balanced voltage dip. Black curve: d -component; gray curve: q -component.

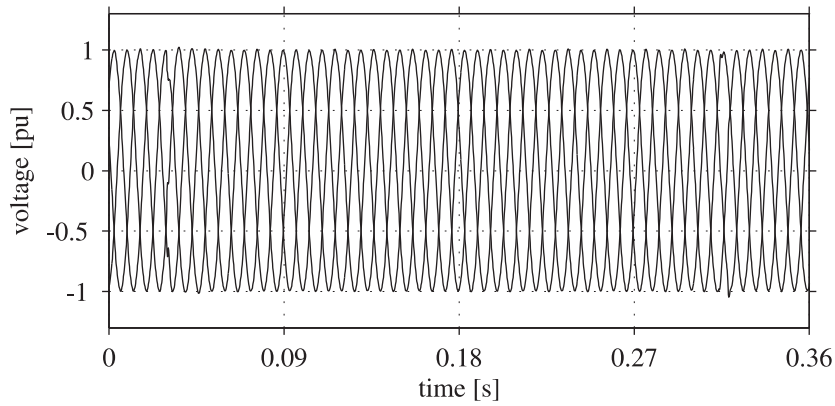


Fig. 4.9 Measured three-phase load voltages during balanced voltage dip. DVC is used.

specifically considering unbalanced conditions. The performance of the DVC1 can be improved by feeding to the same controller only the positive-sequence components of the capacitor vol-

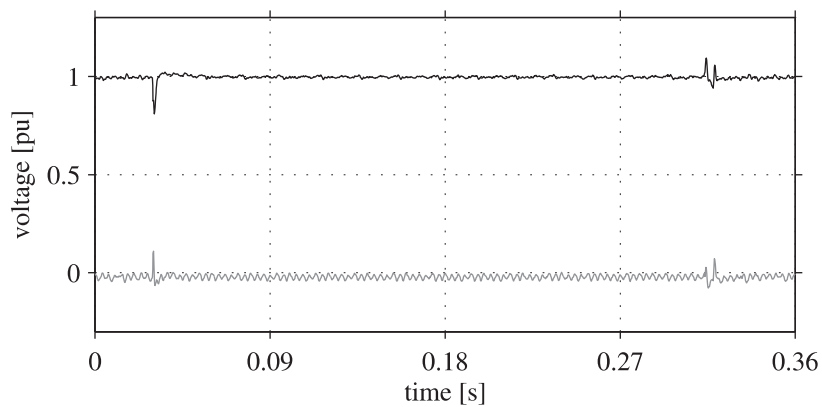


Fig. 4.10 Measured load voltage in dq -frame during balanced voltage dip. DVC is used. Black curve: d -component; gray curve: q -component.

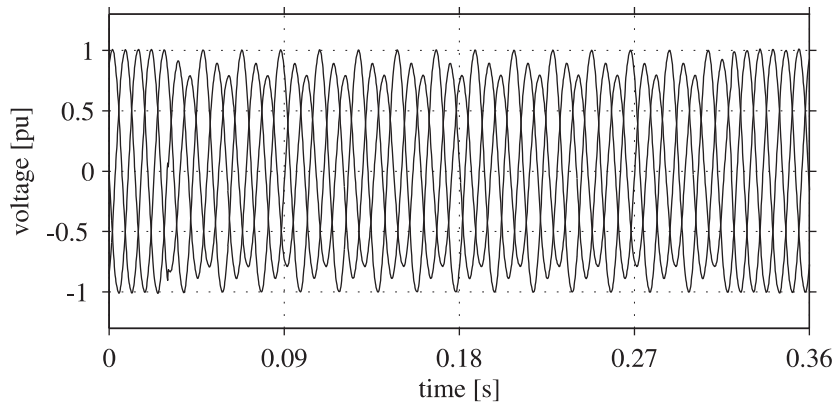


Fig. 4.11 Measured three-phase grid voltages during 85% voltage dip with 11% unbalance.

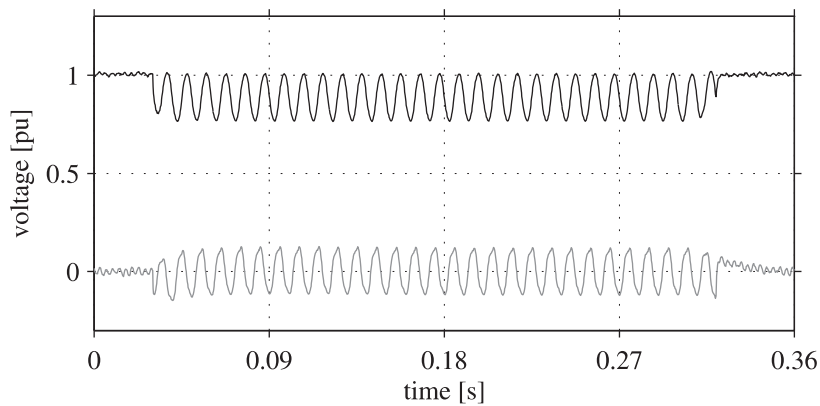


Fig. 4.12 Measured grid voltage in dq -frame during 85% voltage dip with 11% unbalance. Black curve: d -component; gray curve: q -component.

tage and of the reference voltage, while the negative reference voltage is directly added to the voltage output of the current controller. It is shown in [14] that by using this control system the SSC is able to mitigate also unbalanced voltage dips. However, the performance of the con-

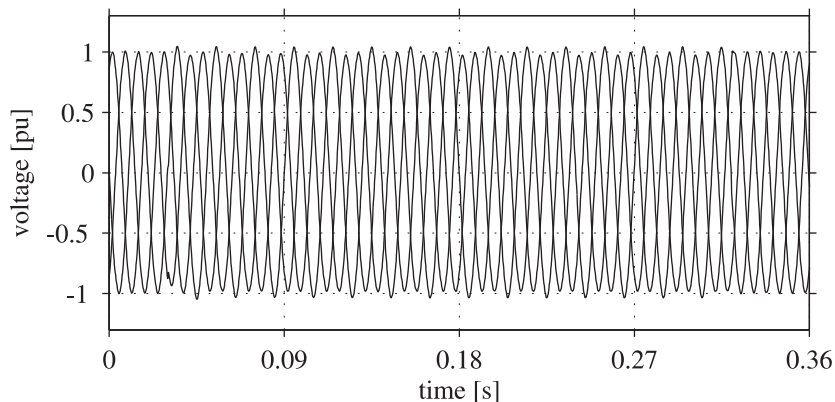


Fig. 4.13 Measured three-phase load voltages during unbalanced voltage dip. DVC is used.

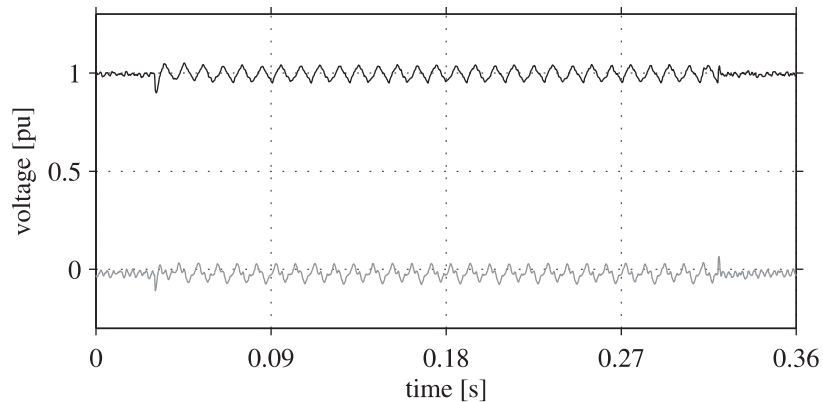


Fig. 4.14 Measured load voltage in dq -frame during unbalanced voltage dip. DVC is used. Black curve: d -component; gray curve: q -component.

troller is related to the size of the filter capacitor and to the percentage of unbalance during the dip [14].

An option to better cope with unbalanced voltage dips is to estimate the phase sequence components of the measured voltages and currents and to modify the DVC1 in order to control positive- and negative-sequence components of the injected voltage separately. This will result in two independent cascade controllers, one implemented in the positively rotating SRF and one implemented in the negative SRF. Experimental verification of the modified control system (addressed to as Positive Negative DVC, PN-DVC) is reported in Paper V. In the paper it is shown that, with PN-DVC, the load voltage is successfully restored to its pre-fault value also in case of unbalanced voltage dips. Furthermore, in [14] the transient performance of the investigated PN-DVC when mitigating unbalanced voltage dips for different types of load is shown. Again, successful restoration of the load voltage is obtained.

4.5 Conclusions

In this chapter, a cascade controller for SSC to mitigate voltage dips has been derived. The cascade controller is constituted by an inner current controller, dedicated to the control of the current output of the VSC, and an outer voltage controller, used to control the filter capacitor voltage. The current controller, described in Section 3.3, takes into account the delay time introduced by the computational time of the control computer and the problem of the saturation of the VSC. An extended analysis of the control system and the interaction between the inner controller and the outer controller has been carried out. It has been shown through experimental results that with the presented control system (here called Dual Vector Controller type 1, DVC1), designed by only considering the positive-sequence components of the measured signals, the SSC is able to mitigate only balanced voltage dips. However, under unbalanced voltage dips, the controller is able to mitigate the dip but the load voltage results unbalanced.

To ensure a proper power quality of the protected load also in case of unbalanced voltage dips, it is suggested to control both the positive and the negative sequences of the filter current and

Chapter 4. Control of Series-connected VSC for Voltage Dip Mitigation

of the capacitor voltage. Although slower, due to the inherited delay introduced by the phase sequence estimation algorithm, the modified DVC (here called Positive Negative DVC, PN-DVC) ensures a satisfactory performance of the SSC when mitigating balanced and unbalanced voltage dips.

Chapter 5

Control of Shunt-connected VSC for Voltage Dip Mitigation

This chapter deals with the control of the shunt-connected VSC for voltage dip mitigation. Two different configurations of the shunt-connected VSC will be considered and compared. Simulation results are reported in Paper VI. Unfortunately, experimental tests could not be carried out, due to practical limitations in the laboratory setup.

5.1 Introduction

In the previous chapter, the control of the SSC for voltage dip mitigation has been described and analyzed. This type of compensator has been successfully applied in a number of applications around the world [80]. However, drawbacks of the SSC are the high cost and the complicated protection system [48]. Furthermore, being a series device, the SSC cannot be used to mitigate interruptions. As already mentioned in Section 2.3.3, an alternative is to use a shunt-connected VSC, shown in Fig.2.10, known also as D-STATCOM or SVC Light [26, 76]. The potential of the shunt-connected VSC to improve the power quality of the voltage has been widely investigated in the literature [6, 77]. However, normally the device has been considered connected to a stiff ac grid, which makes it straightforward to design the controller. On the other hand, this is not realistic since the amount of current needed to boost the PCC voltage is high if the grid is strong. When connected to weak grid, the proposed control strategies have shown slow response, thus making the device not suitable for compensation of short events such as a voltage dip.

In this chapter, the control algorithm for the shunt-connected VSC for dip mitigation is presented. Two different configurations for the VSC system will be considered and compared.

5.2 Voltage dip mitigation using reactive power injection

The principle of voltage dip mitigation using shunt-connected VSC is to inject a current into the PCC in order to keep the load voltage at its rated value. This can be obtained by only injecting reactive current without the aid of an energy storage on the dc side of the VSC. The resulting scheme of the system, shown in Fig.5.1, is thus the same as the one in Fig.2.10, except for the absence of the energy storage device connected to the dc link of the VSC. A dc-link capacitor is still necessary for proper commutation and to provide temporary energy storage.

It is of importance to observe that, as already mentioned in Chapter 2, by injecting only reactive current into the grid, the magnitude of the voltage can be restored, but not its phase angle. As shown in Fig.5.2, where the block scheme of the implemented control system is displayed, the voltage magnitude error, given by the difference between the magnitude of the measured voltage at PCC and its reference, is passed through an ac-voltage controller constituted by a PI-regulator. The output of the ac-voltage controller is the reference reactive current, which is fed to the current controller, explained in Section 3.2. The reference active current is, instead, set to zero.

In a voltage-oriented system, the PLL sets the q -component of the grid voltage in the dq -coordinate system to zero. Thus, the capacitive reactive power injected by the VSC is given by

$$Q = e_{gq}i_{rd} - e_{gd}i_{rq} = -e_{gd}i_{rq} \quad (5.1)$$

Therefore, if the grid voltage is too low, capacitive reactive power should be injected and the current i_{rq} should be negative. The discrete PI-regulator is given by

$$i_{rq}^*(k) = -k_{pQ} [|\underline{e}_g^{(dq)*}(k)| - |\underline{e}_g^{(dq)}(k)|] - \sum_{n=1}^k k_{iQ} [|\underline{e}_g^{(dq)*}(n-1)| - |\underline{e}_g^{(dq)}(n-1)|] \quad (5.2)$$

Simulation results for the shunt-connected VSC for voltage dip mitigation are reported in Paper VI. The obtained results prove that it is possible to mitigate voltage dips with the proposed controller, provided that the size of the VSC is such that it can handle the amount of reactive power needed. One disadvantage that has been pointed out in [75] is that the controller must be

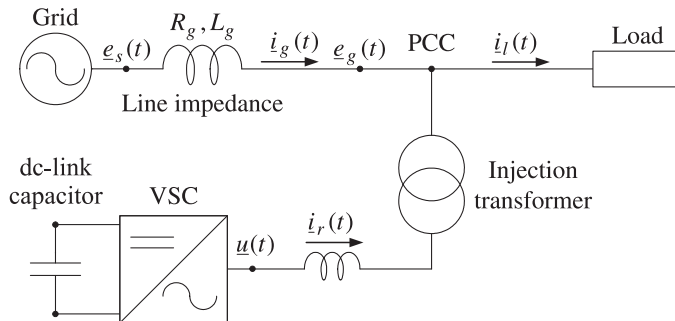


Fig. 5.1 Single-line diagram of shunt-connected VSC designed for reactive power injection only.

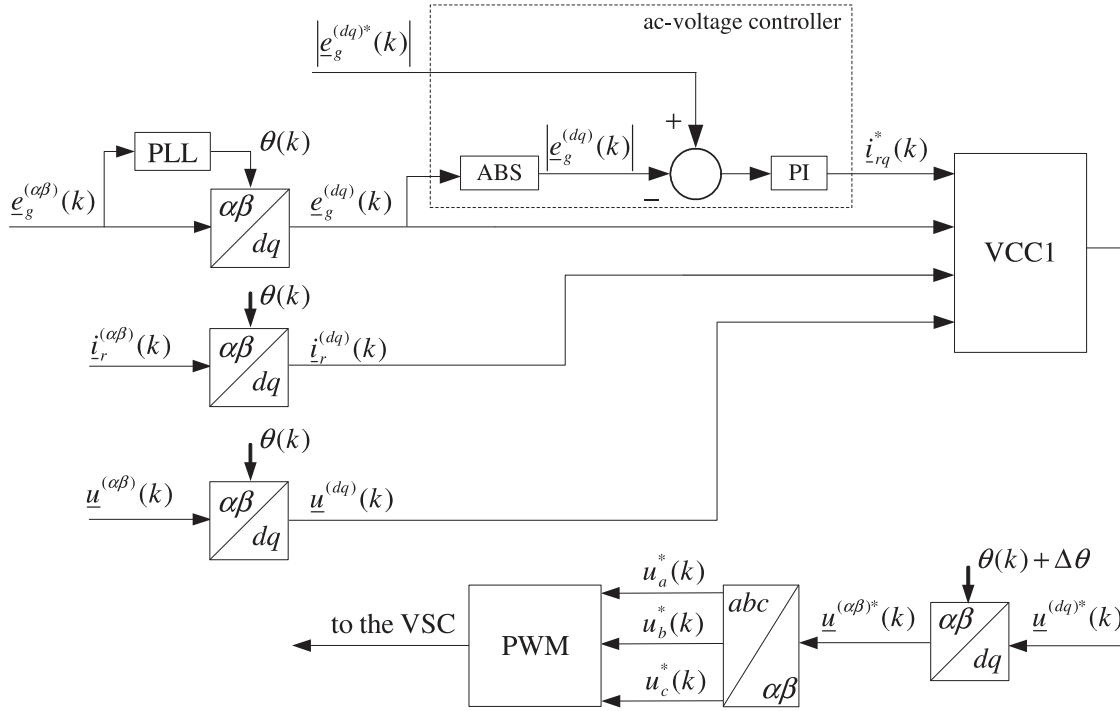


Fig. 5.2 Block scheme of reactive power control using shunt-connected VSC.

tuned for a specific value of the grid and load impedances, and it is very likely that the controller becomes unstable when either of the two parameters change. In Paper VI, stability analysis of the closed-loop system has shown that an overestimation of 2% in the grid impedance will lead to instability. Furthermore, simulation results have proven that the system is also sensitive to variations in the load impedance. The grid and load parameters can increase without resulting in instability by slowing down the controller, but in most cases it will not be fast enough to compensate for voltage dips. Stable operation can be obtained for compensation of slower phenomena, such as voltage fluctuations leading to flicker [7, 73] or voltage stability improvements [67]. However, if the grid configuration and the load are known and expected not to change, this controller can easily be implemented to add voltage dip compensation capability to existing or new shunt-connected VSC installations used for other purpose, such as STATCOM or active filters. To obtain high performance and a more robust controller, modifications of the VSC system are necessary. These modifications will be explained in the next section.

5.3 Shunt-connected VSC using LCL-filter

The modified configuration of the shunt-connected VSC for voltage dip mitigation is shown in Fig.5.3. A capacitor is added in between the filter inductor at the VSC output and the transformer, with the twofold purpose of making the voltage at the PCC more stable and filtering the harmonic voltage components in the VSC output voltage. As a result, the VSC is then connected to the grid by an LCL-filter, where the grid-side inductor is obtained by the leakage reactance of

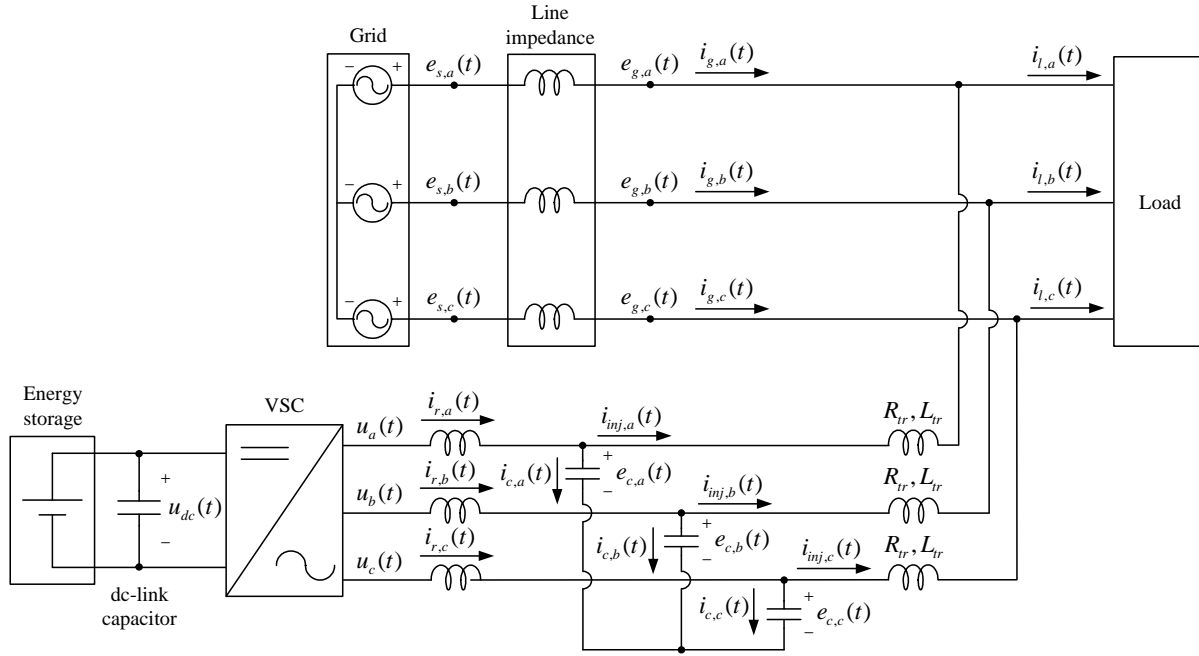


Fig. 5.3 Scheme of shunt-connected VSC using LCL-filter.

the transformer. The leakage inductance and the series resistance of the transformer are denoted in the figure as L_{tr} and R_{tr} , respectively.

The control objective is to maintain the voltage across the filter capacitor, and thereby the PCC voltage, constant. This only holds if the voltage drop over the transformer is negligible. Otherwise, compensation of this voltage drop might be required. A cascade controller, shown in Fig.5.4, that is similar to the one developed for the SSC (derived in Section 4.3), can be used for this purpose. The main differences compared to the series-connected VSC are that the grid current cannot be considered constant and that the reference value of the capacitor voltage is known and not calculated from the measured grid voltage. Observe that the PCC voltage is only measured and used as input to the PLL, in order to achieve proper control of the active and reactive power injected in the grid. Since only the PLL will use the PCC voltage, an inexpensive and simple voltage measurement can be used.

One problem by using the LCL-filter is that unwanted resonances can arise between the filter components. As an example, Fig.5.5 shows the dynamics of the filter current during mitigation of the 71% balanced voltage dip depicted in Fig.4.9. The oscillations in the currents are clearly visible. This phenomenon can be avoided by adding a resistor in series with the filter capacitor, as proposed in [42]. However, the resistor causes losses in all operating conditions and increases the amount of active power needed during voltage dip mitigation. An alternative method [11,58] is to add a fictitious resistance R_d in the inner current controller that, calling $\underline{\varepsilon}_i^{(dq)}$ the current

5.3. Shunt-connected VSC using LCL-filter

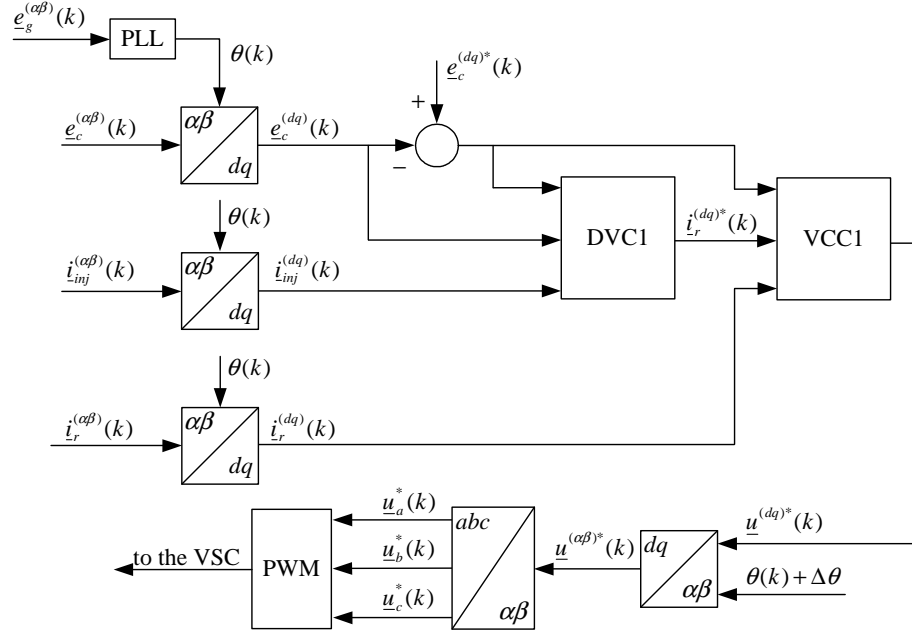


Fig. 5.4 Block scheme of control system for voltage dip mitigation using shunt-connected VSC and LCL-filter.

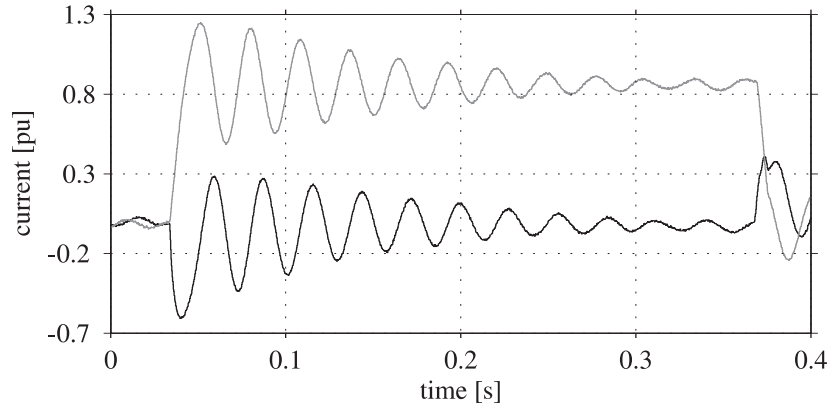


Fig. 5.5 Simulated response of d - and q -component of filter current to balanced voltage dip. VSC with LCL-filter is used. Black curve: d component; gray curve: q component.

error as in (3.34), becomes

$$\begin{aligned} \underline{u}^{(dq)*}(k) = & \underline{e}_g^{(dq)}(k) + R_r \underline{i}_r^{(dq)}(k) + j \frac{\omega L_r}{2} [\underline{i}_r^{(dq)*}(k) + \underline{i}_r^{(dq)}(k)] + \\ & + k_p \underline{\varepsilon}_i^{(dq)}(k) + \sum_{n=1}^k k_i \underline{\varepsilon}_i^{(dq)}(n-1) - R_d \underline{i}_r^{(dq)}(k) \end{aligned} \quad (5.3)$$

This is simplified to

$$\begin{aligned} \underline{u}^{(dq)*}(k) = & \underline{e}_g^{(dq)}(k) - (R_d - R_r)i_r^{(dq)}(k) + j\frac{\omega L_r}{2} [i_r^{(dq)*}(k) + i_r^{(dq)}(k)] + \\ & + k_p \underline{\varepsilon}_i^{(dq)}(k) + \sum_{n=1}^k k_i \underline{\varepsilon}_i^{(dq)}(n-1) \end{aligned} \quad (5.4)$$

This modification is effective in damping the oscillations, but it results in a slightly slower response of the controller. In general, the size of the damping term R_d is a trade-off between the desired damping and the desired speed of response [11]. Here, the value of the damping term R_d , which has been determined by trial and error, is set to 0.5Ω . Therefore, the resistive voltage drop in the current controller is negative.

For the same voltage dip, the dq -currents using the proposed cascade controller and active damping in the inner loop are shown in Fig.5.6. As shown, the current is still affected by oscillation, but with a smaller amplitude and higher damping.

Stability analysis and simulation results obtained for the LCL-filter based shunt-connected VSC are reported in Paper VI. A first important result is that with this configuration, thanks to the presence of the filter capacitor and to the slope introduced by the injection transformer during mitigation, the control system remains stable even for large overestimation of the grid impedance. From the simulation results, it is possible to observe that, although reduced as compared with the L-filter case, still high amount of reactive power is needed to mitigate a shallow dip. This is the main drawback with this configuration, since the power needed is a function of the grid impedance. One interesting result is that the steady state active current during the dip mitigation is zero (see also Fig.5.6). However, at the beginning and at the end of the dip, active current transients occur. These transients are due to the oscillations in the LCL-filter and to the required time for the PLL to track the new phase angle. Therefore, if the dc-link capacitor is big enough to handle the transients, no extra energy storage is needed.

Observe that, as for the control of the SSC, the controller earlier described is implemented in

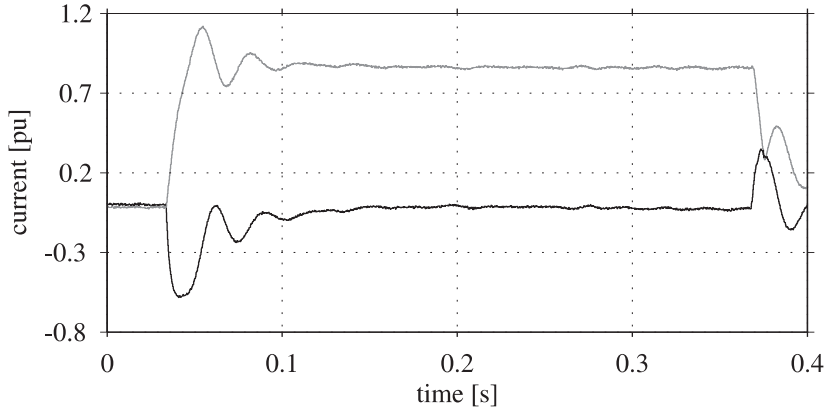


Fig. 5.6 Simulated response of d - and q -component of filter current to balanced voltage dip. VSC with LCL-filter is used. Controller has active damping. Black curve: d component; gray curve: q component.

the positively rotating SRF, thus is not suitable to mitigate unbalanced voltage dips. Again, to be able to cope with unbalanced conditions of the system, it is suggested to control the positive and the negative sequences separately by implementing two separate controllers in the positive and negative SRFs, respectively.

5.4 Conclusions

This chapter has shown that the shunt-connected VSC can be used for voltage dip compensation. A control system that compensates for voltage dips without injecting active power has been presented. It has been shown that successful restoration of the amplitude of the voltage at PCC can be achieved. However, the phase angle of the grid voltage at PCC is affected by phase deviation during dip mitigation. It has been pointed out that this type of control system is very sensitive to system parameter variations. Therefore, to obtain a more robust controller, lower gains in the reactive-power controller must be used. This will lead to a reduced bandwidth of the control system, thus, in most cases the controller will not be fast enough to compensate for voltage dips.

To obtain a high performance and more robust controller, a configuration of shunt-connected VSC with LCL-filter has been proposed. The transient performance of the modified system with the same cascade controller derived in Section 4.3, has been tested under balanced voltage dips. It has been shown that, due to resonance problems between the filter components, oscillations in the current at the output of the VSC can be experienced. To overcome this problem, an active damping term in the inner current controller has been added. By using this modification, satisfactory mitigation of balanced voltage dips can be obtained. However, as expected for the analysis carried out in the previous chapters, modifications in the cascade controller in order to control positive- and negative-sequence components of the controlled variables, are needed for mitigation of an unbalanced voltage dip. With the proposed modification, satisfactory performance of the system also under unbalanced voltage dips can be achieved. However, also when using a shunt-connected VSC with LCL-filter, large amount of current has to be injected into the mains. The VSC must then be designed such that it can handle the amount of reactive power needed.

Chapter 5. Control of Shunt-connected VSC for Voltage Dip Mitigation

Part II - Control of VSC for Subsynchronous Resonance Mitigation

In the first part of this thesis, the use of power electronics based devices at the distribution level (Custom Power Devices) has been discussed. In particular, the focus has been on use of power electronics solutions for voltage dips mitigation. This second part deals with the application of power electronics at the transmission level. Flexible AC Transmission System (FACTS) is a concept introduced by Hingorani in 1991. As already mentioned in Chapter 1, this involves the use of high power electronics controllers in ac transmission networks for a fast and reliable control of power flows and voltages. In their standard application, FACTS devices are used for: power flow regulation, secure loading of transmission lines close to their thermal limits, prevention of cascade outages, power oscillations damping and subsynchronous resonance. Although a lot of research has been carried out in this field, resulting in a number of publications and books, the world of FACTS devices is in continuous mutation. New devices are coming and new applications and control strategies are investigated to improve the existing devices and make them more cost-effective.

The focus of this second part of the thesis is on the use of series-connected VSC for subsynchronous resonance (SSR) mitigation. First, in Chapter 6 a detailed analysis of the SSR problem in power systems will be carried out. The complete mathematical model of a turbine generator connected to a series-compensated transmission line will be derived and analyzed. Further, in this chapter a simplified model for the investigated system for SSR studies will be described and analyzed. Thus, in Chapter 7 a novel control system for a series-connected VSC dedicated to SSR mitigation will be presented. Main differences between the proposed control system and the standard approach proposed in the literature will be discussed.

Chapter 6

Analysis of Subsynchronous Resonance in Power Systems

This chapter presents an overview of the problem of SSR in power systems. Definition and classification of different types of SSR will be given. For a better understanding of the SSR problem, a linearized model of a synchronous generator connected to a radial series-compensated transmission line will be derived. Finally, different countermeasures to the SSR problem will be described.

6.1 Introduction

As mentioned in Chapter 1, series compensation of long transmission lines is a cost-effective solution to enhance the power transfer and improve system stability. It was generally believed until 1971 that series compensation up to 70% of the total inductive reactance of the transmission line could be applied with little concern [5]. Usually, only problems related to protection and thermal issues were taken into account. However, it was in 1971 that system designers learned that the use of series compensation can lead to adverse phenomena on turbine-generator units connected to a series-compensated transmission line. These phenomena are related to a resonant condition leading to an energy exchange between the generation unit and the transmission line. As a result, oscillations having a characteristic frequency below the fundamental frequency of the power system (synchronous frequency) can be experienced. Therefore, this resonance condition has been named subsynchronous resonance (SSR) [25].

The SSR phenomenon was first recognized in the Mohave Project in 1970 [27]. The Mohave Project consisted of a 750 MVA cross-compound generation unit located in southern Nevada. Figure 6.1 shows the single-line diagram of the power system in the Mohave area at that time. In 1970, a shaft damage was experienced when opening the circuit breaker indicated in the figure; thus, when the Mohave generation unit became radially connected to the southern California Lugo bus. At that time, the power system operators did not recognize the problem and the generation unit was placed back in operation after a few months. Thus, a nearly identical incident occurred one year later, in 1971. For each event, the unit was shut down manually by the site

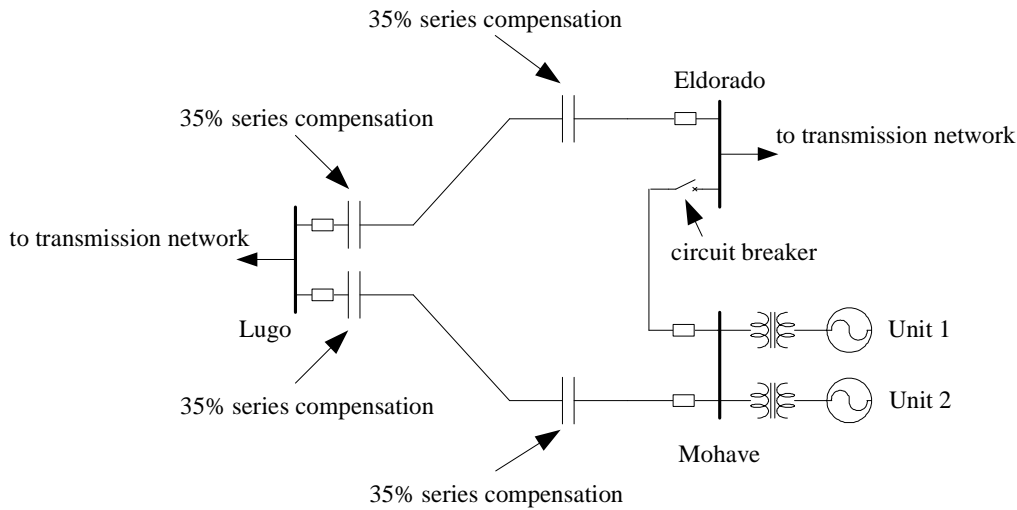


Fig. 6.1 Single-line diagram of power system in Mohave area in 1970.

operators. The operators observed flickering lights in the control room, vibration of the control room floor, excessive field current and alarm of excessive vibrations in the generator-shaft system, which continued for a few minutes. It was found that the shaft section in the slip rings area of the high-pressure turbine experienced extreme heating due to cycling torsional stress. Due to the excessive heat, the insulation in the slip rings area of the generator failed, resulting in an electric arc to ground of the generator field lead. Furthermore, a metallurgical analysis showed that the shaft material had experienced high stress, leading to plasticity of the material.

After a subsequent analysis of the phenomenon, it was found that the event experienced in the Mohave Project was due to an energy exchange between the series-compensated line and the mechanical system of the Mohave power plant. These oscillations, due to the new power system condition when the circuit breaker was open, built up from a steady-state condition and led to growing shaft torque oscillations at one of the natural frequencies of the generator shaft.

After the two incidents in the Mohave Project, great effort has been directed from the research community and power system utilities to avoid the risk of SSR during system operation. Furthermore, the IEEE instituted a working group to define and classify the different types of SSR that can occur in a power system.

6.2 Definition and classification of SSR

According with the IEEE definition, SSR is “an electric power systems condition where the electric network exchanges energy with a turbine generator at one or more of the natural frequencies of the combined system below the synchronous frequency of the system,” [25]. SSR is typically classified into two main groups: steady-state SSR (induction generator effect, IGE, and torsional interaction effect, TI) and transient torques (also known under the name of torque amplification, TA). In particular:

6.2. Definition and classification of SSR

- **Induction generator effect (IGE).** IGE is a pure electrical phenomenon taking place at frequencies very close to the rated network frequency and in power systems having high degree of series compensation. In particular, IGE is caused by self excitation of the electrical system and does not involve the mechanical system of the generation unit. The resistance of the rotor to subsynchronous currents, viewed from the armature terminals, is negative [5]. For the same currents, the network presents a positive resistance. If the negative resistance of the generator is greater in magnitude than the resistance of the network, sustained subsynchronous currents will be induced. In principle, IGE may occur in all kind of power generating plants, even for hydro-generator units. Although of academic interest, this form of SSR is rarely encountered in actual power systems. For this reason, SSR due to IGE will not be considered in this thesis.
- **Torsional interaction effect (TI).** TI is an unstable condition that denotes an energy exchange between the electric power systems and the generator shaft. In particular, TI occurs when the induced subsynchronous torque in the generator is electrically close to one of the natural frequencies of the generator shaft. When this happens, generator rotor oscillations will build up and this motion will induce armature voltage components at both subsynchronous (having frequency $f_0 - f_m$, where f_0 and f_m are the system frequency and the natural frequency of the generator shaft, respectively) and supersynchronous ($f_0 + f_m$) frequencies. If the resulting subsynchronous torque equals or exceeds the inherent mechanical damping of the rotor, the system will become self-excited. This kind of SSR does not occur in hydro-power stations, since the inertia of the hydro turbine is much smaller than the inertia of the generator (in the range of 5%). Therefore, when a torsional oscillation occurs in the shaft, the speed variation will almost totally be encountered on the hydro turbine, while the speed of the generator will remain approximately unaffected by the oscillation. As a result, the oscillation will not be recognized by the transmission system. SSR due to TI effect can instead occur in thermal power plants, where the inertia of the turbine is in the same order of magnitude of the inertia of the generator. It is important to mention that SSR due to TI effect can also be experienced in case of large converters connected to a turbine generator. Typical examples are HVDC converter stations using both thyristor converters and transistor converters. However, this condition is out of the scope of this thesis and will not be treated.
- **Torque amplification (TA).** TA is the phenomenon that results from system disturbances. Each disturbance results in a sudden change in the current that will tend to oscillate. In case of non series-compensated lines, this will result in a dc offset that will decay with the subtransient and transient time constants of the generator. In a series-compensated line, instead, oscillations having a frequency corresponding to the resonance frequency of the network will be experienced. If the frequency of these oscillations coincides with one of the natural frequencies of the generator shaft, large torques will be experienced. SSR due to TA can cause severe mechanical torsional oscillations in the shaft system connecting the generator and the turbines in thermal power plants.

Of the three types of interaction described above, the first two may be considered as small disturbance conditions (at least, initially). The third one, instead, is definitely not a small dis-

turbance and in this case non-linearities of the power system must be taken into account in the analysis. From the system analysis point of view, it is important to observe that the induction generator effect and torsional interaction effects can be analyzed using linear models, while the mathematical analysis of the torque amplification effect is complex and cumbersome and is typically approached using simulation programs.

In the following, a model for a synchronous generator connected to a series-compensated transmission line will be derived. Thus, the problem of SSR due to TI will be investigated.

6.3 Synchronous generator model

In this section, the mathematical model for the synchronous generator will be derived. A synchronous machine is characterized by both short and long time constants. Due to the long time constants, steady-state equations can only be used in case of slow variations. For a better understanding of the SSR phenomenon, it is of interest to adopt a detailed model of the machine, including stator and rotor windings (field and damping windings).

Figure 6.2(a) presents a schematic model of a three-phase model of a salient pole synchronous machine. A detail of the generator rotor model is shown separately in Fig.6.2(b) for clarity. From the figure it is possible to understand that the reluctance of the air-gap depends on the rotor position. To simplify the modeling of the machine, it is common practice to identify two different values in two principal directions, i.e. in the direction of the rotor flux (denoted as d -axis in the figure) and in its perpendicular direction (q -axis)¹. Therefore, in this set of coor-

¹Note: in this chapter, and in this chapter only, the dq -coordinate system is a flux-oriented system synchronized with the rotor position. This choice has been made since it is commonly accepted notation. In the previous and in the following chapters, instead, the dq -frame is synchronized with the grid voltage vector.

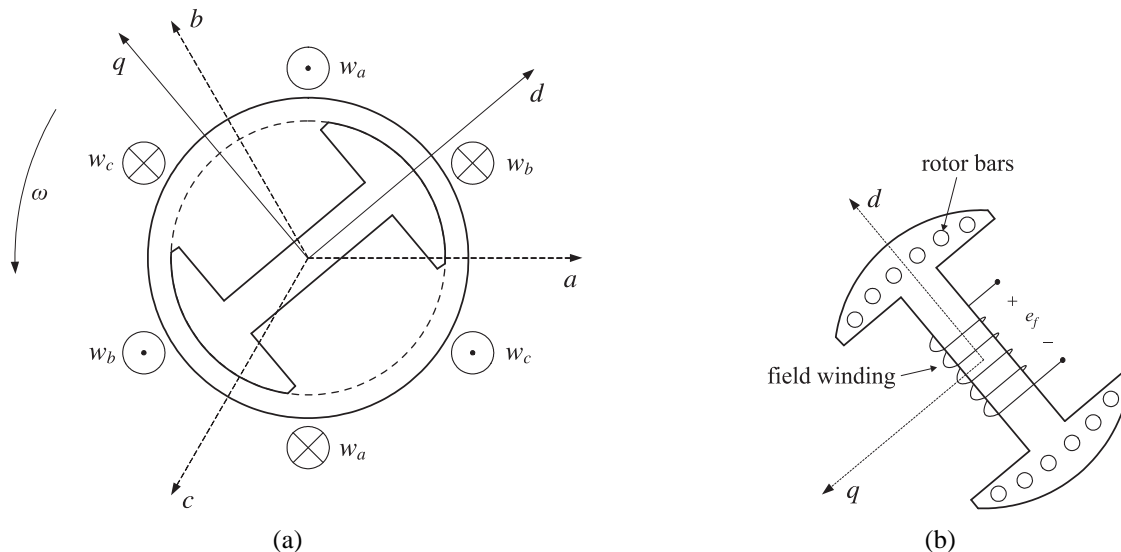


Fig. 6.2 Model of synchronous machine (a) and detail of generator rotor (b).

6.3. Synchronous generator model

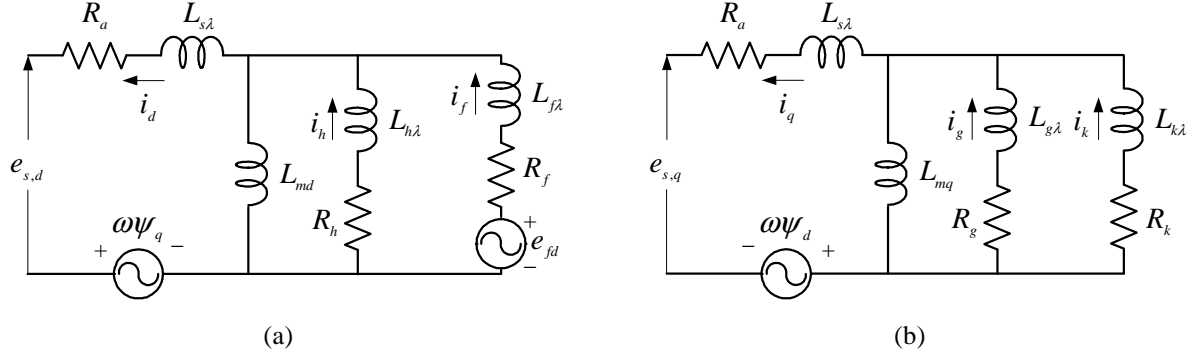


Fig. 6.3 Synchronous machine model in rotating dq -reference frame. Plot a: equivalent circuit in d -direction; plot b: equivalent circuit in q -direction.

ordinates, the d -axis is aligned with the direction of the rotor flux. In this way, the coefficients of the flux linkage equations are constant and independent of the rotor position, as long as the flux can be considered constant.

Figure 6.3 shows the equivalent dq -model of the synchronous machine in the rotating dq -coordinate system. The model consists of the stator windings (denoted in the figure with the subscript s) and the field winding (subscript f). The rotor bars can be represented by a set of windings in the d - and q -direction. To represent the effect of the rotor bars, it is common to use three windings: one damping winding in the d -axis (winding h), and two damping windings in the direction of the q -axis (g and k).

With the signal reference given in Fig.6.3, the voltage equations for the stator and the rotor can be expressed in per-unit as [39]

$$\begin{aligned}
 e_{s,d} &= \frac{1}{\omega_B} \frac{d\psi_d}{dt} - \frac{\omega}{\omega_B} \psi_q - R_a i_d \\
 e_{s,q} &= \frac{1}{\omega_B} \frac{d\psi_q}{dt} + \frac{\omega}{\omega_B} \psi_d - R_a i_q \\
 e_{f,d} &= \frac{1}{\omega_B} \frac{d\psi_f}{dt} + R_f i_f \\
 0 &= \frac{1}{\omega_B} \frac{d\psi_h}{dt} + R_h i_h \\
 0 &= \frac{1}{\omega_B} \frac{d\psi_g}{dt} + R_g i_g \\
 0 &= \frac{1}{\omega_B} \frac{d\psi_k}{dt} + R_k i_k
 \end{aligned} \tag{6.1}$$

where $e_{s,d}$ and $e_{s,q}$ are the stator voltage components in the d - and q -direction, respectively, and ω_B is the base angular frequency (see Fig.6.3 for other parameters definition). Under the assumption that the magnetizing inductances between the stator windings, the damper windings and the field winding are identical, the flux linkage in the rotor reference frame can be expressed

as follows

$$\begin{aligned}
 \psi_d &= -L_{sd}i_d + L_{md}i_f + L_{md}i_h \\
 \psi_q &= -L_{sq}i_q + L_{mq}i_g + L_{mq}i_k \\
 \psi_f &= -L_{md}i_d + L_f i_f + L_{md}i_h \\
 \psi_h &= -L_{md}i_d + L_{md}i_f + L_h i_h \\
 \psi_g &= -L_{mq}i_q + L_g i_g + L_{mq}i_k \\
 \psi_k &= -L_{mq}i_q + L_{mq}i_g + L_k i_k
 \end{aligned} \tag{6.2}$$

where

$$\begin{aligned}
 L_{sd} &= L_{md} + L_{s\lambda} \\
 L_{sq} &= L_{mq} + L_{s\lambda} \\
 L_f &= L_{md} + L_{f\lambda} \\
 L_h &= L_{md} + L_{h\lambda} \\
 L_g &= L_{mq} + L_{g\lambda} \\
 L_k &= L_{mq} + L_{k\lambda}
 \end{aligned}$$

From (6.2), the currents can be expressed as a function of the fluxes as

$$\boldsymbol{\psi} = \mathbf{L}\mathbf{i} \tag{6.3}$$

where $\boldsymbol{\psi} = [\psi_d \ \psi_q \ \psi_f \ \psi_h \ \psi_g \ \psi_k]^T$, $\mathbf{i} = [i_d \ i_q \ i_f \ i_h \ i_g \ i_k]^T$ and the inductance matrix \mathbf{L} is given by

$$\mathbf{L} = \begin{bmatrix} -L_{sd} & 0 & L_{md} & L_{md} & 0 & 0 \\ 0 & -L_{sq} & 0 & 0 & L_{mq} & L_{mq} \\ -L_{md} & 0 & L_f & L_{md} & 0 & 0 \\ -L_{md} & 0 & L_{md} & L_h & 0 & 0 \\ 0 & -L_{mq} & 0 & 0 & L_g & L_{mq} \\ 0 & -L_{mq} & 0 & 0 & L_{mq} & L_k \end{bmatrix} \tag{6.4}$$

The voltage equations can thus be expressed in state space form as

$$\begin{aligned}
 \dot{\boldsymbol{\psi}} &= \underbrace{-(\mathbf{L}^{-1}\mathbf{R} + \mathbf{W})}_{\mathbf{A}_G} \boldsymbol{\psi} + \mathbf{B}_{G1}e_{f,d} + \mathbf{B}_{G2}\mathbf{u}_G \\
 \mathbf{y}_G &= \underbrace{\mathbf{L}^{-1} \begin{bmatrix} 1 & 0 & 0 & 0 & 0 & 0 \\ 0 & 1 & 0 & 0 & 0 & 0 \end{bmatrix}}_{\mathbf{C}_G} \boldsymbol{\psi}
 \end{aligned} \tag{6.5}$$

where the input and output vectors are defined as

$$\mathbf{u}_G = [e_{s,d} \ e_{s,q}]^T \quad \mathbf{y}_G = [i_d \ i_q]^T$$

while the matrices \mathbf{R} , \mathbf{W} , \mathbf{B}_{G1} and \mathbf{B}_{G2} are

$$\mathbf{R} = \omega_B \begin{bmatrix} R_a & 0 & 0 & 0 & 0 & 0 \\ 0 & R_a & 0 & 0 & 0 & 0 \\ 0 & 0 & -R_f & 0 & 0 & 0 \\ 0 & 0 & 0 & -R_h & 0 & 0 \\ 0 & 0 & 0 & 0 & -R_g & 0 \\ 0 & 0 & 0 & 0 & 0 & -R_k \end{bmatrix}, \quad \mathbf{W} = \begin{bmatrix} 0 & \omega & 0 & 0 & 0 & 0 \\ -\omega & 0 & 0 & 0 & 0 & 0 \\ 0 & 0 & 0 & 0 & 0 & 0 \\ 0 & 0 & 0 & 0 & 0 & 0 \\ 0 & 0 & 0 & 0 & 0 & 0 \\ 0 & 0 & 0 & 0 & 0 & 0 \end{bmatrix}$$

$$\mathbf{B}_{G1} = \begin{bmatrix} 0 \\ 0 \\ \omega_B \\ 0 \\ 0 \\ 0 \end{bmatrix}, \quad \mathbf{B}_{G2} = \begin{bmatrix} \omega_B & 0 \\ 0 & \omega_B \\ 0 & 0 \\ 0 & 0 \\ 0 & 0 \\ 0 & 0 \end{bmatrix}$$

It is of interest to observe that all elements of the matrix \mathbf{A}_G are constant, except for the cross-coupling terms in the matrix \mathbf{W} . This is very important when linearizing the model. Furthermore, if an analysis of IGE is performed, the generator-rotor speed can be considered constant at its rated value $\omega_0 = 2\pi f_0$ [53]; thus, the matrix \mathbf{A}_G becomes time invariant.

6.4 Transmission network model

Figure 6.4 shows the single-line diagram of a radial series-compensated transmission line. The investigated system is taken from the IEEE First Benchmark Model (FBM) [23] (see Appendix B for model parameters) and it consists of a single generator connected to an infinite bus through a series RLC-network.

To derive the state-space model of the transmission network, a new set of rotating coordinates, denoted as DQ -coordinate system and synchronized with the infinite bus voltage vector \underline{e}_b , has been considered. Thus, \underline{e}_b is aligned with the direction of the Q -axis during steady-state. Applying KVL to the system depicted in Fig.6.4, the following equations can be written

$$\underline{e}_s^{(DQ)} = \underbrace{(R_L + jX_L)}_{\mathbf{Z}_L} \underline{i}^{(DQ)} + \frac{X_L}{\omega_B} \frac{d\underline{i}^{(DQ)}}{dt} + \underline{e}_c^{(DQ)} + \underline{e}_b^{(DQ)} \quad (6.6)$$

$$\frac{d\underline{e}_c^{(DQ)}}{dt} = j\omega_0 \underline{e}_c^{(DQ)} + \omega_B X_c \underline{i}^{(DQ)} \quad (6.7)$$

where all symbols have the meaning in Fig.6.4 and R_L and X_L are the series resistance and inductive reactance seen from the generator terminals. For the purpose of this investigation, it is convenient to express (6.6) in the dq -frame, yielding

$$\underline{e}_s^{(dq)} = \mathbf{Z}_L \underline{i}^{(dq)} + \frac{X_L}{\omega_B} \frac{d\underline{i}^{(dq)}}{dt} + e^{j\delta} \left[\underline{e}_c^{(DQ)} + \underline{e}_b^{(DQ)} \right] \quad (6.8)$$

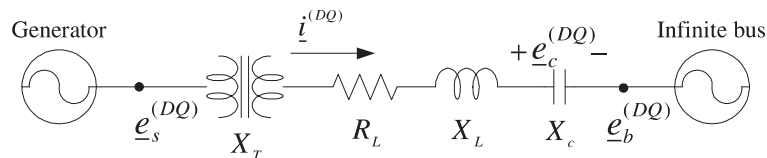


Fig. 6.4 Single-line diagram of series-compensated line.

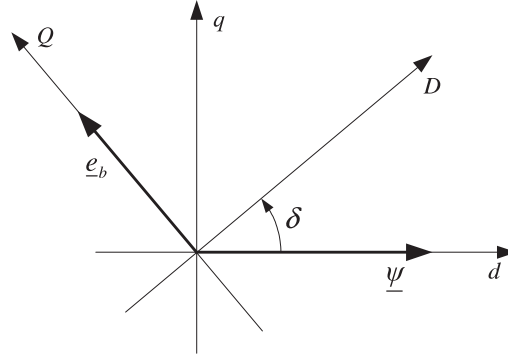


Fig. 6.5 Relation between dq -frame and DQ -frame.

with δ the angle difference between the dq - and the DQ -coordinate systems (see Fig.6.5).

As a result, the transmission network model can be expressed in state-space form as

$$\begin{aligned} \frac{d}{dt} \begin{bmatrix} e_{c,D} \\ e_{c,Q} \end{bmatrix} &= \mathbf{A}_N \begin{bmatrix} e_{c,D} \\ e_{c,Q} \end{bmatrix} + \mathbf{B}_N \begin{bmatrix} i_D \\ i_Q \end{bmatrix} \\ \begin{bmatrix} e_{s,d} \\ e_{s,q} \end{bmatrix} &= \mathbf{P} \mathbf{C}_N \begin{bmatrix} e_{c,D} \\ e_{c,Q} \end{bmatrix} + \mathbf{D}_N \begin{bmatrix} i_d \\ i_q \end{bmatrix} + \mathbf{D}_{N1} \frac{d}{dt} \begin{bmatrix} i_d \\ i_q \end{bmatrix} + \mathbf{P} \begin{bmatrix} e_{b,D} \\ e_{b,Q} \end{bmatrix} \end{aligned} \quad (6.9)$$

where \mathbf{C}_N is a second-order unit matrix, while the other matrices are

$$\begin{aligned} \mathbf{A}_N &= \begin{bmatrix} 0 & -\omega \\ \omega & 0 \end{bmatrix}, & \mathbf{B}_N &= \begin{bmatrix} \omega_B X_c & 0 \\ 0 & \omega_B X_c \end{bmatrix} \\ \mathbf{D}_N &= \begin{bmatrix} R_L & -X_L \\ X_L & R_L \end{bmatrix}, & \mathbf{D}_{N1} &= \frac{X_L}{\omega_B} \begin{bmatrix} 1 & 0 \\ 0 & 1 \end{bmatrix} \\ \mathbf{P} &= \begin{bmatrix} \cos \delta & -\sin \delta \\ \sin \delta & \cos \delta \end{bmatrix} \end{aligned} \quad (6.10)$$

Note that, in (6.9), the voltage at the machine terminals (considered as an output) is a function of the derivative of the line current, i.e. is a function of the derivative of the input. This implies a difficulty when deriving the state-space model for the transmission network. This problem can be solved by combining the network and the generator equations, as described in the following section.

6.5 Combined generator and network equations

In the previous sections, the circuit equations for the generator and the network have been derived. Furthermore, it has been pointed out in the previous section that one problem encountered when deriving the state-space model for the transmission network is that the derivative of the line current appears in the voltage equations. From (6.5), and under the consideration that the

matrix \mathbf{C}_G is time invariant, the derivative of the current can be expressed in terms of the flux linkage as

$$\frac{d}{dt} \begin{bmatrix} i_d \\ i_q \end{bmatrix} = \mathbf{C}_G \dot{\boldsymbol{\psi}} \quad (6.11)$$

After algebraic manipulations, (6.5) and (6.9) can be combined to give an unique state-space system [53]

$$\dot{x}_E = \mathbf{A}_E x_E + \mathbf{B}_{G1} e_{f,d} + \mathbf{B}_{Gb} E_b \quad (6.12)$$

where E_b is the amplitude of the infinite bus voltage while the new state vector is

$$x_E = \begin{bmatrix} \boldsymbol{\psi} \\ e_{c,D} \\ e_{c,Q} \end{bmatrix} \quad (6.13)$$

The state matrices describing the total electrical system can be derived as follows

$$\mathbf{A}_E = \begin{bmatrix} \mathbf{A}_G + \mathbf{B}_{G2} \mathbf{F} \mathbf{G} & \mathbf{B}_{G2} \mathbf{F} \mathbf{P} \mathbf{C}_N \\ \mathbf{B}_N \mathbf{P}^T \mathbf{C}_G & \mathbf{A}_N \end{bmatrix}$$

$$\mathbf{B}_{Gb} = \mathbf{B}_{G2} \mathbf{F} \mathbf{P} \begin{bmatrix} 0 \\ 1 \end{bmatrix}$$

with

$$\mathbf{F} = \left\{ \begin{bmatrix} 1 & 0 \\ 0 & 1 \end{bmatrix} - \frac{X_L}{\omega_B} \mathbf{C}_G \mathbf{B}_{G2} \right\}^{-1}, \quad \mathbf{G} = \mathbf{Z}_L \mathbf{C}_G + \frac{X_L}{\omega_B} \mathbf{C}_G \mathbf{A}_G$$

where the meaning of all employed matrices is given in Sections 6.3 and 6.4. Equation (6.12) describes the dynamical behavior of the electrical system depicted in Fig.6.4. To investigate the phenomenon of TI effect, a model describing the dynamics of the generator-turbine shaft system is needed. This will be derived in the next section.

6.6 Turbine-generator shaft model

In this section, the state-space equations describing the mechanical system of the turbine-generator will be derived. Figure 6.6 shows, as an example, the shaft model of the turbine-generator given in the IEEE FBM. The model consists of six turbine sections modeled separately: an high-pressure stage (denoted in the figure by HP), an intermediate stage (IP), two low-pressure stages (LP_A and LP_B), the generator (G) and the exciter (EX). Each rotating mass is connected to the previous and the following mass by elastic shaft-sections, represented in the figure by a spring coefficient ($K_{i,i-1}$ and $K_{i,i+1}$, respectively) and a mutual damping term ($D_{i,i-1}$ and $D_{i,i+1}$, respectively). The term D_i represents the self-damping term.

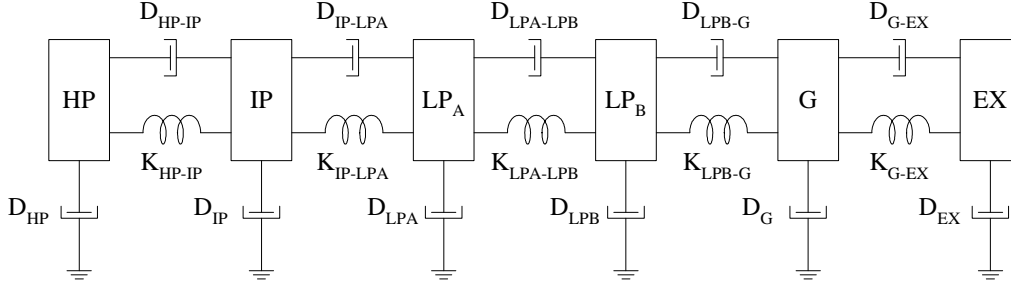


Fig. 6.6 Mechanical model of synchronous machine. Torsional system with six masses.

The equation of motion for the i^{th} -mass is given by

$$2H_i \frac{d^2 \delta_i}{dt^2} + D_i \frac{d\delta_i}{dt} + D_{i,i-1} \left(\frac{d\delta_i}{dt} - \frac{d\delta_{i-1}}{dt} \right) + D_{i,i+1} \left(\frac{d\delta_i}{dt} - \frac{d\delta_{i+1}}{dt} \right) + K_{i,i-1}(\delta_i - \delta_{i-1}) + K_{i,i+1}(\delta_i - \delta_{i+1}) = T_{mi} - T_{ei} \quad (6.14)$$

where H_i is the inertia constant of the i^{th} -rotor section, while T_{mi} and T_{ei} are the relative mechanical and electrical torque. Observe that $T_{ei} = 0$, $\forall i \neq G$ (neglecting rotating exciter), while $T_{mG} = 0$.

From now on, for clarity of the notation, the different sections of the shaft model will be indicated with progressive numbering starting from the left hand side of Fig.6.6 (as an example, the inertia of the intermediate-pressure turbine will be denoted as H_2 , while the spring constant $K_{\text{HP-IP}}$ will be K_{12}). By writing (6.14) for all sections of the turbine-shaft model and taking the generator-rotor angle and speed as outputs, the following state-space equation is obtained

$$\begin{aligned} \dot{x}_M &= \mathbf{A}_M x_M + \mathbf{B}_M T \\ y_M &= \mathbf{C}_M x_M \end{aligned} \quad (6.15)$$

where

$$x_M = [\delta_1 \ \omega_1 \ \delta_2 \ \omega_2 \ \delta_3 \ \omega_3 \ \delta_4 \ \omega_4 \ \delta_5 \ \omega_5 \ \delta_6 \ \omega_6]^T$$

$$y_M = \begin{bmatrix} \delta_5 \\ \omega_5 \end{bmatrix} = \begin{bmatrix} \delta_G \\ \omega_G \end{bmatrix}$$

For the turbine-generator shaft depicted in Fig.6.6, the matrixes \mathbf{A}_M , \mathbf{B}_M and \mathbf{C}_M are given by:

$$\mathbf{A}_M = \begin{bmatrix} 0 & \omega_B & 0 & 0 & 0 & 0 & 0 & \cdot & 0 \\ -\frac{K_{12}}{2H_1} & -\frac{D_1+D_{12}}{2H_1} & \frac{K_{12}}{2H_1} & \frac{D_{12}}{2H_1} & 0 & 0 & 0 & \cdot & 0 \\ 0 & 0 & 0 & \omega_B & 0 & 0 & 0 & \cdot & 0 \\ \frac{K_{12}}{2H_2} & \frac{D_{12}}{2H_2} & -\frac{K_{12}+K_{23}}{2H_2} & -\frac{D_2+D_{12}+D_{23}}{2H_2} & \frac{K_{23}}{2H_2} & \frac{D_{23}}{2H_2} & 0 & \cdot & 0 \\ \cdot & \cdot \\ 0 & 0 & \cdot & \cdot & \cdot & 0 & 0 & 0 & \omega_B \\ 0 & 0 & \cdot & \cdot & \cdot & \frac{K_{56}}{2H_6} & \frac{D_{56}}{2H_6} & -\frac{K_{56}}{2H_6} & -\frac{D_{56}}{2H_6} \end{bmatrix}$$

$$\mathbf{B}_M = \begin{bmatrix} 0 \\ 0 \\ \cdot \\ \cdot \\ \cdot \\ \frac{1}{2H_5} \\ 0 \\ 0 \end{bmatrix}, \quad \mathbf{C}_M = \begin{bmatrix} 0 & 0 & 0 & \cdot & \cdot & 1 & 0 & 0 & 0 \\ 0 & 0 & 0 & \cdot & \cdot & 0 & 1 & 0 & 0 \end{bmatrix}$$

The state-space system in (6.15) is a powerful tool for the analysis of the dynamics of the mechanical system. The eigenvalues of matrix \mathbf{A}_M contain information about the critical frequencies of the generator-shaft, while its eigenvectors (right eigenvectors) can give information about the relative torsional swing between two adjacent masses [39].

6.6.1 Modal analysis

In the previous section, the state-space model for a turbine-generator shaft has been derived. Generally, the parameters for the generator shaft that are of interest to build up the model in (6.15) are known with fairly good accuracy. The manufacturers supply all constants based on design data and have the possibility to predict the torsional frequencies with an inaccuracy of less than 1 Hz for the significant mode shapes [4]. If disagreement between the model and the test is observed, the data can be revised in order to match the measured critical frequencies [38].

To determine the parameters of the spring-mass model, field tests are typically carried out by the generator manufacturers. For this reason, the data for the shaft are usually given in terms of modal quantities [4]. A great advantage when using modal quantities is that the state-space equations described in (6.15) can be decoupled in order to investigate the behavior of the shaft at the different frequencies. To determine the modal parameters, it is common practice to apply a coordinate transformation to (6.14). The swing equation in (6.14) can be rewritten in compact form as

$$\mathbf{H}\ddot{\delta} + \mathbf{D}\dot{\delta} + \mathbf{K}\delta = \mathbf{T} \quad (6.16)$$

where \mathbf{T} is a vector formed by the applied torque to the shaft. The following transformation can be used

$$\delta = \mathbf{Q}_M \delta_M \quad (6.17)$$

meaning that we can transform the shaft angles in a new coordinate system. Assuming that only the self dampings are present (the damping between adjacent masses is typically smaller as compared with the damping between the mass and the reference and can thus be neglected [4]) and substituting (6.17) into (6.16), the following equation hold

$$\mathbf{H}\mathbf{Q}_M \delta_M'' + \mathbf{D}\mathbf{Q}_M \delta_M' + \mathbf{K}\mathbf{Q}_M \delta_M = \mathbf{T} \quad (6.18)$$

Premultiplying both sides for the transpose of the transformation matrix \mathbf{Q}_M , we get

$$\mathbf{Q}_M^T \mathbf{H}\mathbf{Q}_M \delta_M'' + \mathbf{Q}_M^T \mathbf{D}\mathbf{Q}_M \delta_M' + \mathbf{Q}_M^T \mathbf{K}\mathbf{Q}_M \delta_M = \mathbf{Q}_M^T \mathbf{T} \quad (6.19)$$

or

$$\mathbf{H}_M \ddot{\delta}_M + \mathbf{D}_M \dot{\delta}_M + \mathbf{K}_M \delta_M = \mathbf{T}_M \quad (6.20)$$

where

- \mathbf{H}_M is a diagonal matrix that represents the modal inertia;
- \mathbf{D}_M is a diagonal matrix that represents the modal damping;
- \mathbf{K}_M is a diagonal matrix that represents the modal spring constant;

The transformation matrix \mathbf{Q}_M must be selected so that the matrices \mathbf{H}_M and \mathbf{K}_M are diagonal. Although there are infinite number of matrices that can fulfill this property, it is common practice to build up the \mathbf{Q}_M matrix using the eigenvectors of the system described in (6.15) [4, 53].

The modal inertias and spring constants for the IEEE FBM, together with the natural frequencies of the generator-shaft system, are shown in Table 6.1. Here, the system damping has been

TABLE 6.1: Modal quantities for IEEE FBM.

	Mode 1	Mode 2	Mode 3	Mode 4	Mode 5
Frequency (ω_M)	98.72	126.99	160.53	202.85	298.19
Inertia (H_M)	2.70	27.80	6.92	3.92	11297
Spring constant (K_M)	139.63	2376.40	945.89	856.30	$532.86 \cdot 10^3$

neglected. Observe that the radial frequency of the i^{th} torsional mode is given by [53]

$$\omega_i = \sqrt{\omega_B \frac{K_{Mi}}{2H_{Mi}}} \quad (6.21)$$

As shown in Table 6.1, the lowest inertia is the one corresponding to Mode 1, while the highest is corresponding to Mode 5. From this analysis it can be easily understood that Mode 1 undamping resulting from any torsional interaction will be the most severe, while Mode 5 will be unlikely affected by TI effect, due to the high value of the corresponding inertia.

One particular remark has to be made for the damping constants. The practice tells that although spring and inertia constants can be predicted with high accuracy, the estimated damping constants (both self and mutual damping) might differ from the measured quantities with a factor that varies from two to five [38]. This is due to the rough approximation that the braking torque produced by the damping is directly proportional to the relative speed between the considered mass and the reference (self damping) or between adjacent masses (mutual damping). Typically, the generator manufactures provide the so called “decrement factor” (obtained from the decrement test) instead of the modal damping. For the i^{th} -mode, the relation between modal damping and decrement factor is [4, 53]

$$\sigma_{Mi} = \frac{D_{Mi}}{4H_{Mi}} \quad (6.22)$$

From the above equation it is possible to observe that, for a given σ_{Mi} , the modal damping is proportional to the modal inertia H_{Mi} . In case of hydro turbines, the rotor inertia is about 10 to 40 times higher as compared to a steam turbine [53]. This explains why SSR phenomena have not been observed on hydro units.

In this thesis, the purpose of the modal analysis in (6.19) or of the shaft-system model in (6.15) is to determine the critical frequencies of the generator shaft. When calculating the eigenvalues of the shaft system, the damping coefficients have no significant effect on the imaginary part of the poles (i.e., they do not affect the calculated natural frequencies of the shaft), but only on their real part. This is confirmed from the root locus depicted in Fig.6.7, where the poles of the shaft-system for the IEEE FBM when varying the decrement factor from 0 to 0.05 s^{-1} is depicted.

Example: Dynamical behavior of IEEE FBM shaft model

In this example, the response of the shaft system depicted in Fig.6.6 when a sinusoidal input torque is suddenly applied to the generator rotor will be analyzed. The frequency of the applied torque corresponds to the imaginary part of the eigenvalues of the matrix \mathbf{A}_M . Mechanical data for the considered system are given in the IEEE FBM, reported in Appendix B. The damping data is not provided in the IEEE FBM and have been neglected in this analysis. The matrix \mathbf{A}_M has been built as described in the previous section. The corresponding eigenvalues are displayed in Table 6.2.

As expected from the modal analysis carried out in the previous section, there are five mechanical resonances at 47.46 Hz, 32.28 Hz, 25.55 Hz, 20.20 Hz and 15.71 Hz. In addition, there is a mode 0 that, when considering the mechanical system alone, has a characteristic frequency of 0 Hz. If also the electrical system (generator plus network) is modeled, the interaction between

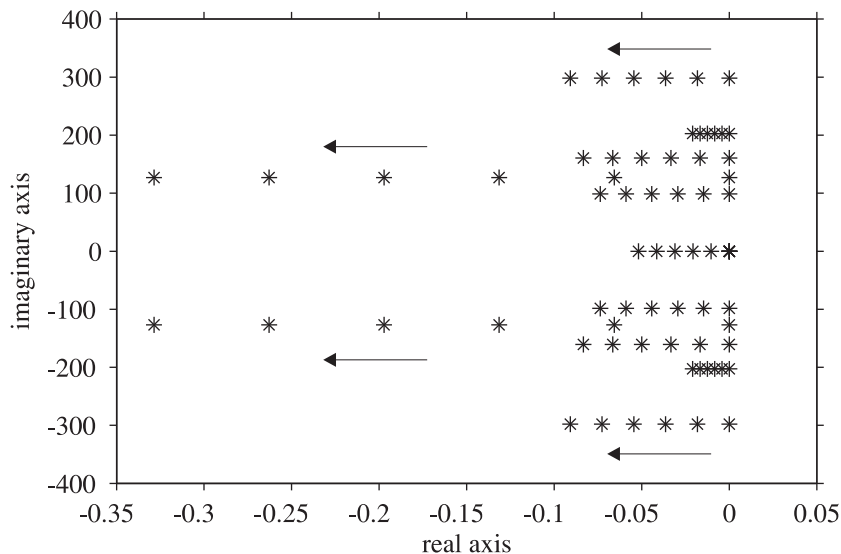


Fig. 6.7 Root locus of IEEE FBM shaft-system when varying decrement factor from 0 to 0.05 s^{-1} .

TABLE 6.2: Eigenvalues for A_M .

$-1.1 \cdot 10^{-014} \pm j298.18$
$-3.5 \cdot 10^{-015} \pm j202.85$
$5.3 \cdot 10^{-015} \pm j160.52$
$0 \pm j126.95$
$-3.5 \cdot 10^{-015} \pm j98.721$
$-4.5 \cdot 10^{-016}$
0

the mechanical and the electrical system leads to non-zero frequencies for mode 0 (typically between 0.2 and 2 Hz). Frequency oscillations corresponding to mode 0 will appear also in absence of SSR and in this case all masses in the rotor-shaft system will oscillate as a single mass.

The analyzed system has been simulated using Matlab. Figures 6.8(a) to 6.8(e) show the applied mechanical torque (upper plot) and the obtained rotor angle (lower plot) for the different eigenfrequencies. It can be observed that at these frequencies, the variation in the input torque will result in the excitation of oscillations in the rotor angle. It is clear from the figure that the shaft-system reacts differently at the different frequencies. In particular, as expected from the modal analysis, the system is more sensitive to applied torques with frequencies of 15.71, 25.55 and 32.38 Hz, due to the low inertia of the mechanical system at these specific frequencies.

6.7 Combined mechanical-electrical equations

Since SSR is the result of an interaction between electrical and mechanical systems, it is of interest to derive a model that combines the mechanical system in (6.15) and the complete electrical system, consisting of the generator and the electrical transmission network, in (6.12). As shown in Fig.6.9, the link between these two systems is the electrical torque, which can be written in the dq -coordinate system as

$$T_e = \text{Im}\{\underline{i}^{(dq)} \text{conj}[\underline{\psi}^{(dq)}]\} = i_q \psi_d - i_d \psi_q \quad (6.23)$$

Assuming that the mechanical input torque T_m is constant, for small variations $\Delta T_m = 0$. The linearized electrical torque is given by

$$\Delta T_e = i_{q0} \Delta \psi_d + \psi_{d0} \Delta i_q - i_{d0} \Delta \psi_q - \psi_{q0} \Delta i_d \quad (6.24)$$

where i_{d0} is the value of the armature current in the d -direction at the equilibrium point. The same notation holds for the other quantities. Equation (6.24) can be expressed in matrix form as

$$\Delta T_e = C_{ME} \Delta x_G \quad (6.25)$$

6.7. Combined mechanical-electrical equations

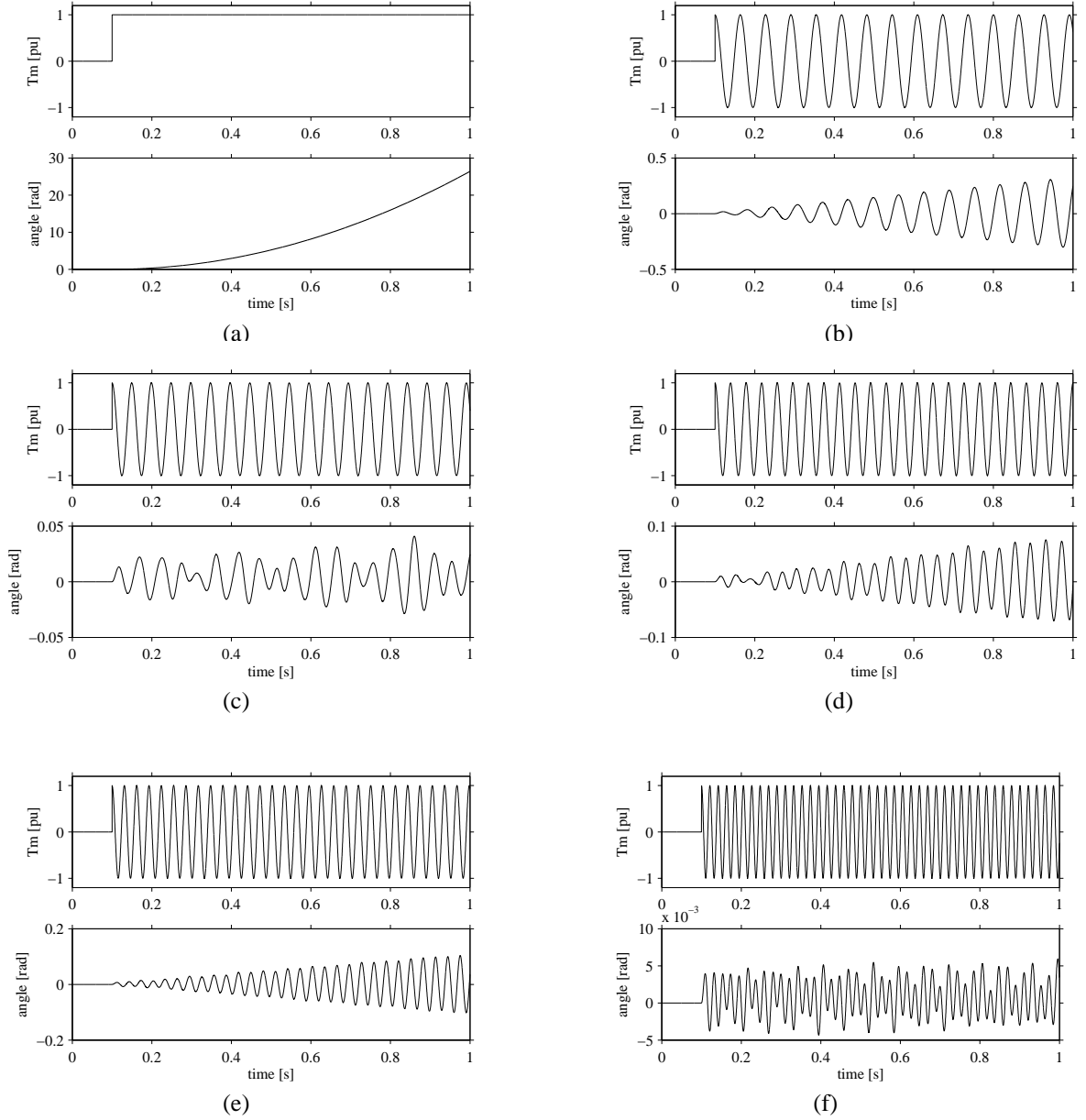


Fig. 6.8 Simulated turbine-shaft response in generator angle to oscillating generator torque. Plot (a): torque frequency equal to 0 Hz (mode 0); Plot (b): torque frequency equal to 15.71 Hz (mode 1); Plot (c): torque frequency equal to 20.205 Hz (mode 2); Plot (d): torque frequency equal to 25.547 Hz (mode 3); Plot (e): torque frequency equal to 32.28 Hz (mode 4); Plot (f): torque frequency equal to 47.456 Hz (mode 5).

with

$$\mathbf{C}_{ME} = [i_{q0} \ -i_{d0} \ 0 \ 0 \ 0] + [-\psi_{q0} \ \psi_{d0}] \mathbf{C}_G$$

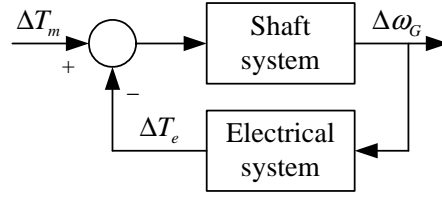


Fig. 6.9 Block-diagram of combined mechanical-electrical system for SSR studies.

The linearized state equation for the electrical model given in (6.12) is

$$\Delta \dot{x}_E = \mathbf{A}_{El} \Delta x_E + \mathbf{B}_{EM} \Delta y_M \quad (6.26)$$

The matrix \mathbf{A}_{El} has the same structure of the matrix \mathbf{A}_E , with the difference that it is written in terms of small perturbations. The matrix \mathbf{B}_{EM} can be written as

$$\mathbf{B}_{EM} = \begin{bmatrix} \mathbf{B}_{EM1} & \mathbf{B}_{EM2} \\ \mathbf{B}_{EM3} & \mathbf{B}_{EM4} \end{bmatrix}$$

where:

$$\begin{aligned} \mathbf{B}_{EM1} &= \mathbf{B}_{G2} \mathbf{F} \mathbf{P}_{\delta=\delta_0} \{ \mathbf{C}_N x_{N0} + [0 \ E_b]^T \} \\ \mathbf{B}_{EM2} &= \{ \mathbf{A}_E|_{\omega=\omega_0} + \mathbf{B}_{G2} \mathbf{F} \mathbf{Z}_L|_{\omega=\omega_0} \mathbf{C}_G + \frac{X_L}{\omega_B} \mathbf{B}_{G2} \mathbf{C}_G \mathbf{A}_E|_{\omega=\omega_0} \} x_{G0} \\ \mathbf{B}_{EM3} &= \mathbf{B}_N \mathbf{P}^T|_{\delta=\delta_0} \mathbf{C}_G x_{G0} \\ \mathbf{B}_{EM4} &= [0 \ 0]^T \end{aligned}$$

with x_{G0} and x_{N0} the state variables for the generator (electrical model) and for the network calculated at the equilibrium point, respectively.

Finally, (6.24) and (6.26) can be combined in order to obtain the state equations of the combined mechanical-electrical system. The final system equations can be written as

$$\begin{bmatrix} \Delta \dot{x}_E \\ \Delta \dot{x}_M \end{bmatrix} = \begin{bmatrix} \mathbf{A}_E & \mathbf{B}_{EM} \mathbf{C}_M \\ \mathbf{B}_M [\mathbf{C}_{ME} \ 0 \ 0] & \mathbf{A}_M \end{bmatrix} \begin{bmatrix} \Delta x_E \\ \Delta x_M \end{bmatrix} = \mathbf{A}_T \Delta x_T$$

The eigenvalues of the matrix \mathbf{A}_T contain all the information regarding the stability of the analyzed system at a specific operating point. In particular, the eigenvalues of the matrix \mathbf{A}_T give information about the risk of TI between the electrical and the mechanical system.

6.8 SSR due to torsional interaction effect

The mathematical model described in the previous sections is suitable for analyzing SSR due to the TI effect. SSR due to TI effect build up fairly slowly but can reach very high torque for

the generator shaft, causing a reduction of the life time of the generator shaft or even its failure. The risk for SSR due to the TI effect can be investigated using the feedback loop depicted in Fig.6.9 [56], which describes the interaction between the electrical and the mechanical system in the rotating coordinate system synchronized with the generator rotor. Let us call G_e the transfer function from $\Delta\omega_G$ to ΔT_e

$$G_e(s) = \frac{\Delta T_e}{\Delta\omega_G}(s) \quad (6.27)$$

To investigate the response of the electrical system at different frequencies, the Laplace operator can simply be substituted with $j\omega_k$, where ω_k is the frequency of interest (for example, one of the natural frequencies of the generator shaft). At each frequency, the transfer function G_e can be split up into its real and imaginary part as

$$G_e(j\omega_k) = \text{Re}[G_e(j\omega_k)] + j\text{Im}[G_e(j\omega_k)] = \Delta T_{De}(j\omega_k) - j\frac{\omega_B}{\omega_k}\Delta T_{Se}(j\omega_k) \quad (6.28)$$

where $\Delta T_{De}(j\omega_k)$ and $\Delta T_{Se}(j\omega_k)$ are named damping and synchronizing torque, respectively. A similar definition holds for the mechanical damping and synchronizing torque, ΔT_{Dm} and ΔT_{Sm} . In a series-compensated network, the electrical damping torque can be considered equal to zero for all frequencies except the resonance frequency of the electrical system [53], where ΔT_{De} becomes negative. SSR due to TI can occur in the power system if the electrical resonance of the system (calculated in the rotating coordinates) coincides with, or is electrically close to, one of the natural resonance frequencies of the generator-turbine shaft system. In fixed coordinates this means that SSR may occur if the sum of the electrical resonance frequency and one of the natural resonance frequencies of the generator shaft system is close to the generator mechanical rotation frequency (i.e. the network frequency). Under the assumption that the synchronizing torque is negligible [53], the instability of a torsional mode of frequency ω_m occurs if

$$\Delta T_D(j\omega_m) = \Delta T_{De}(j\omega_m) + \Delta T_{Dm}(j\omega_m) < 0 \quad (6.29)$$

A typical situation when the system can experience TI effect is depicted in Fig.6.10, where the damping curves for the electrical (top) and the mechanical (bottom) system of the IEEE FBM are depicted. The value of the capacitive reactance is set to 0.35 pu, corresponding to 70% compensation of 0.50 pu inductive reactance of the considered transmission line. This level of series compensation is a practical upper limit for series compensation of long transmission lines. From the figure it is possible to observe that there are two critical frequencies for the generator shaft in the neighborhood of the network electrical undamping, one at 20.21 Hz and one at 25.55 Hz. This can lead to resonance between the transmission line and the turbine-generator shaft. The risk for a TI effect can also be observed from the poles location of the combined mechanical-electrical system (Fig.6.11), where two pairs of complex and conjugate poles present a positive real part. Finally, the system instability is confirmed by the time-domain simulation results in Fig.6.12, where the torques between the different turbine sections of the generator shaft are depicted. As shown, due to the TI effect, oscillations slowly build up in all sections of the turbine system connected with the generator. These oscillations, having characteristic frequency of 25.55 Hz for all shaft sections, reach high values, for instance 6 pu (peak value) in the LP_A - LP_B torque after two minutes.

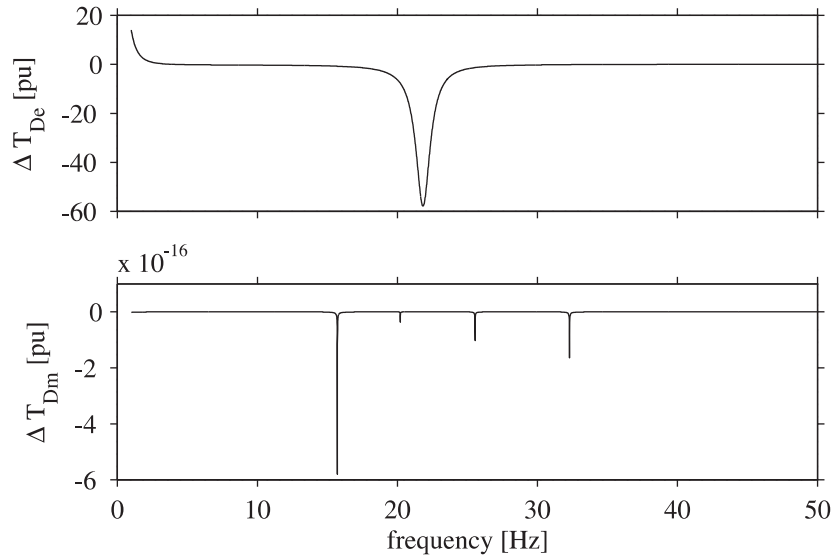


Fig. 6.10 Comparison between electrical damping (top) and mechanical damping (bottom) for IEEE FBM.

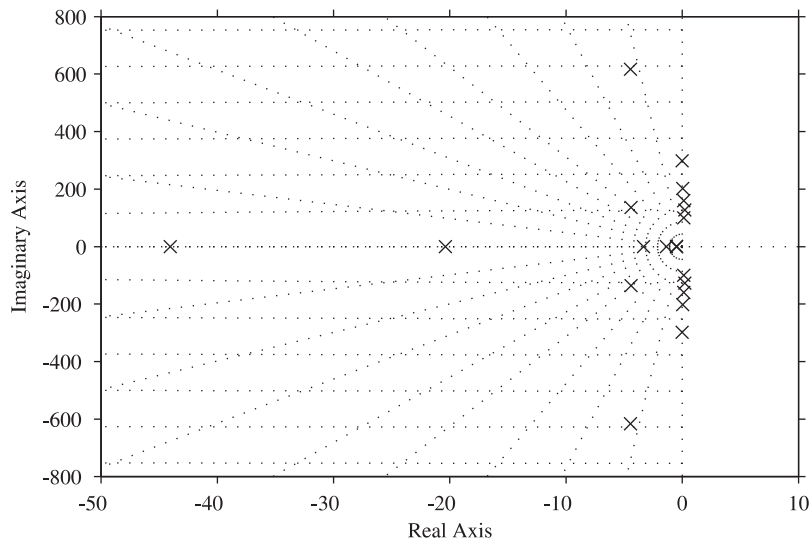


Fig. 6.11 Poles location for combined mechanical-electrical system for IEEE FBM. Two pairs of complex-conjugate poles have positive real part.

6.8. SSR due to torsional interaction effect

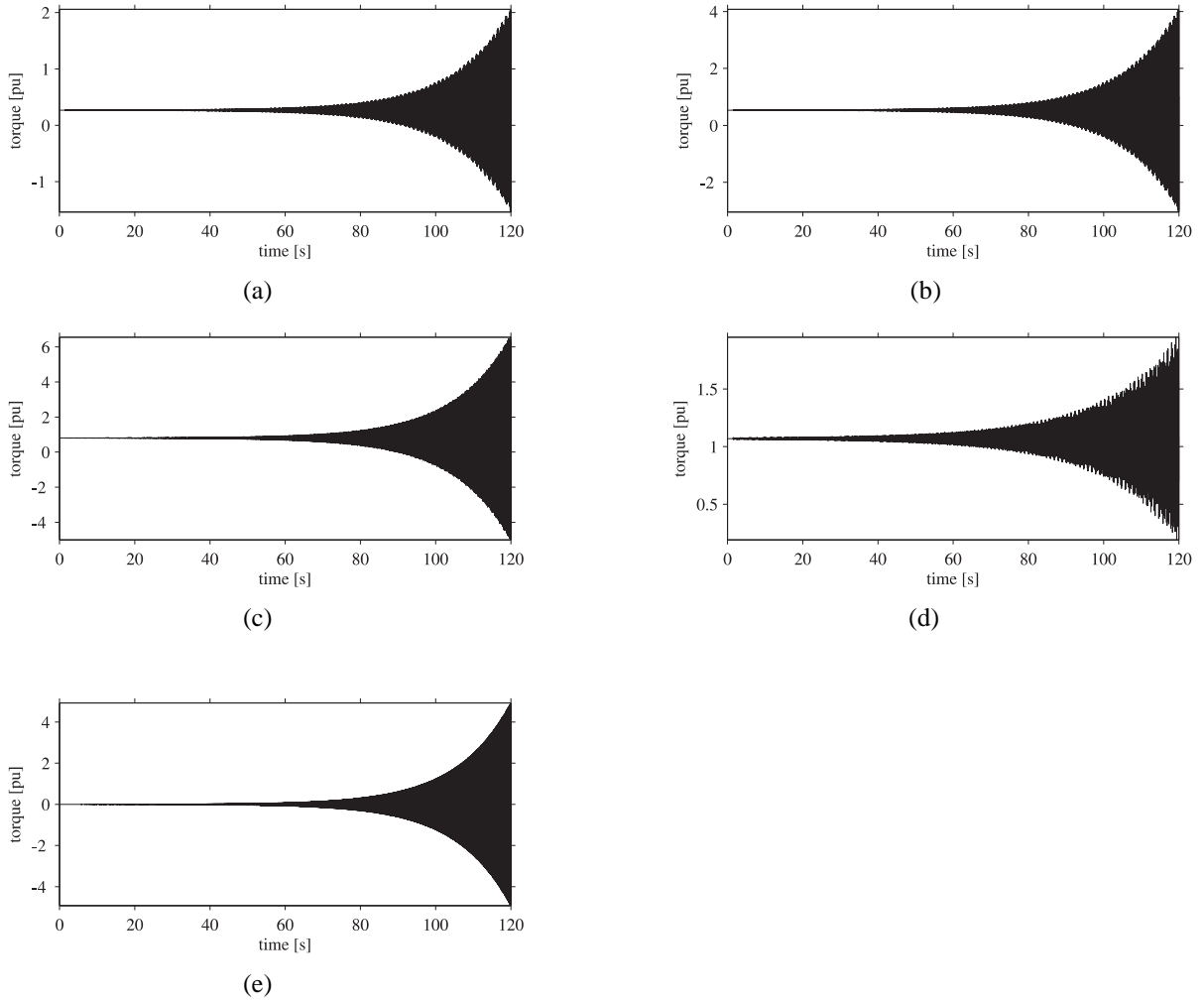


Fig. 6.12 Simulated TI effect on generator-shaft torques for IEEE FBM. Plot a: HP-IP torque; Plot b: IP-LP_A torque; Plot c: LP_A-LP_B torque; Plot d: LP_B-GEN torque; Plot e: GEN-EXC torque.

6.9 Frequency scanning analysis

In Section 6.7, the complete state-space model for a synchronous generator connected to a series-compensated transmission line has been derived. One problem related with this approach is that it is cumbersome and leads to high-order systems, depending on the complexity of the generator and the transmission system. As an example, the combined mechanical-electrical system for the IEEE FBM is a 20th-order system. Therefore, alternative methods for a simplified analysis of the SSR phenomenon are needed, especially when deriving a control algorithm. One of these methods is the frequency scanning analysis (FSA) [54]. FSA is a frequency method that can be used to screen the system conditions that give rise to potential SSR problems. The advantage of using this method is that it gives a quick and simple check to determine the stability of a torsional mode. When using FSA, the synchronous generator is modeled as a frequency dependent voltage source behind its subtransient inductance X_G'' . Thus, the model described in Fig.6.4 is approximated as in Fig.6.13. Note that, since only subsynchronous frequencies are considered, the infinite bus has been replaced by a short-circuit.

Applying KVL in the fixed $\alpha\beta$ -frame, the following equation in the Laplace domain can be written

$$\underline{e}_s^{''(\alpha\beta)}(s) = \left(R + sL + \frac{1}{sC} \right) \underline{i}^{(\alpha\beta)}(s) = Z(s)\underline{i}^{(\alpha\beta)}(s) \quad (6.30)$$

with

$$C = \frac{1}{\omega_B X_c}, \quad L = \frac{X_G'' + X_T + X_L}{\omega_B}$$

Equation (6.30) can be expressed in the DQ -coordinate systems as

$$\underline{e}_s^{''(DQ)}(s) = Z^{(DQ)}(s)\underline{i}^{(DQ)}(s) \quad (6.31)$$

where $Z^{(DQ)}(s)$ is the impedance of the network seen from the internal bus of the generator in the DQ -frame. The objective of the FSA is to derive the transfer function of the electrical torque as a function of the speed variation for the simplified system depicted in Fig.6.13. Under the assumption that the amplitude of the internal bus voltage vector $\underline{e}_s^{''(\alpha\beta)}$ is constant and equal to E_s'' , the variation of the electrical torque is given by

$$\Delta T_e = E_s'' \Delta i_q \quad (6.32)$$

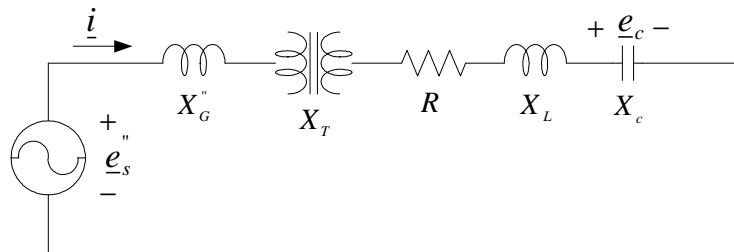


Fig. 6.13 Single-line diagram of series-compensated line for FSA.

6.9. Frequency scanning analysis

The active component of the line current in the rotoric dq -coordinate system, i_q , is linked to the current in the DQ -reference frame through the transformation matrix \mathbf{P} , defined in (6.10), as

$$i_q = i_D \sin \delta + i_Q \cos \delta \quad (6.33)$$

or, for small signal analysis

$$\begin{aligned} \Delta i_q &= \Delta i_D \sin \delta_0 + i_{D0} \cos \delta_0 \Delta \delta + \Delta i_Q \cos \delta_0 - i_{Q0} \sin \delta_0 \Delta \delta \\ &= \Delta i_Q + i_{d0} \Delta \delta \end{aligned} \quad (6.34)$$

where it has been assumed that the rotor angle at the operating point δ_0 is equal to zero. The relation between the internal bus voltage in the DQ - and in the dq -coordinate system is

$$\underline{e}_s^{(DQ)} = \underline{e}_s^{(dq)} e^{-j\delta} \quad (6.35)$$

When a variable speed $\Delta\omega$ is applied to the generator rotor, (6.35) can be linearized around an operating point as

$$\begin{aligned} \Delta e_{s,D} &= \Delta e_{s,d} \cos \delta_0 - e_{s,d0} \sin \delta_0 \Delta \delta + \Delta e_{s,q} \sin \delta_0 + e_{s,q0} \cos \delta_0 \Delta \delta \\ \Delta e_{s,Q} &= -\Delta e_{s,d} \sin \delta_0 - e_{s,d0} \cos \delta_0 \Delta \delta + \Delta e_{s,q} \cos \delta_0 - \Delta e_{s,q0} \sin \delta_0 \Delta \delta \end{aligned} \quad (6.36)$$

or, assuming that $\delta_0 = 0$ as before

$$\begin{aligned} \Delta e_{s,D} &= \Delta e_{s,d} + e_{s,q0} \Delta \delta \\ \Delta e_{s,Q} &= -e_{s,d0} \Delta \delta + \Delta e_{s,q} \end{aligned} \quad (6.37)$$

Since the dq -frame is a flux-oriented system, the d -component of the generator voltage is equal to zero, while the per-unit q -component is given by

$$e_{s,q} = \frac{\omega_0}{\omega_B} E_s'' \quad (6.38)$$

Therefore, if the voltage amplitude E_s'' is constant, (6.37) simplifies to

$$\begin{aligned} \Delta e_{s,D} &= E_s'' \frac{\omega_0}{\omega_B} \Delta \delta = E_s'' \omega_0 \frac{\Delta \omega}{s} \\ \Delta e_{s,Q} &= E_s'' \Delta \omega \end{aligned} \quad (6.39)$$

Denoting as $Y(s)$ the admittance function of the system in Fig.6.13 ($Y(s) = Z^{-1}(s)$), from (6.31) it is possible to express the D - and the Q -component of the line current as

$$\begin{bmatrix} \Delta i_D(s) \\ \Delta i_Q(s) \end{bmatrix} = \begin{bmatrix} Y_{DD}(s) & Y_{DQ}(s) \\ Y_{QD}(s) & Y_{QQ}(s) \end{bmatrix} \begin{bmatrix} \Delta e_{s,D}(s) \\ \Delta e_{s,Q}(s) \end{bmatrix} \quad (6.40)$$

where, the components of the admittance function are given by [53]

$$\begin{aligned} Y_{DD}(s) &= Y_{QQ}(s) = \frac{1}{2} [Z^{-1}(s - j\omega_0) + Z^{-1}(s + j\omega_0)] \\ Y_{DQ}(s) &= Y_{QD}(s) = -j\frac{1}{2} [Z^{-1}(s - j\omega_0) - Z^{-1}(s + j\omega_0)] \end{aligned} \quad (6.41)$$

It is now possible to derive the expression for the current Δi_Q as

$$\Delta i_Q(s) = Y_{QD}(s)\Delta e_{s,D}(s) + Y_{QQ}(s)\Delta e_{s,Q}(s) = \left[Y_{QQ}(s) + Y_{QD}(s)\frac{\omega_0}{s} \right] E_s'' \Delta\omega \quad (6.42)$$

Substituting (6.42) into (6.34) and assuming for simplicity that the line current at the operating point is equal to zero, the variation of the electrical torque can be expressed as

$$\Delta T_e(s) = \left[Y_{QQ}(s) + Y_{QD}(s)\frac{\omega_0}{s} \right] E_s''^2 \Delta\omega \quad (6.43)$$

Therefore, the transfer function G_e for the simplified system is given by

$$G_e(s) = \frac{\Delta T_e}{\Delta\omega}(s) = \left[Y_{QQ}(s) + Y_{QD}(s)\frac{\omega_0}{s} \right] E_s''^2 \quad (6.44)$$

thus, the electrical damping torque can be found as

$$\Delta T_{De}(j\omega) = \text{Re} [G_e(j\omega)] \quad (6.45)$$

Figure 6.14 shows the resulting electrical damping torque when using FSA (solid curve). It is possible to observe that the negative peak in the electrical damping occurs at the same frequency (21.83 Hz) as for the detailed model of the synchronous generator (dashed curve). As a difference, the electrical damping curve is approximately equal to zero for all frequencies below the resonance, while when the detailed model is considered the electrical damping is positive for frequencies below 5 Hz. This is due to the effect of the damping windings in the machine (neglected in the simplified model). However, this range of frequencies is not of interest for SSR studies, thus, this region can be neglected. Another discrepancy that can be observed between the detailed and the simplified model is that the minimum peak in the electrical damping is higher for the detailed model, meaning that the simplified model gives a slightly optimistic view for the TI effect. This is due to the fact that the simplified model does not take into account the negative resistance presented by the synchronous machine in the subsynchronous frequency range (IGE effect). The correction for IGE is possible by adding a small frequency-dependent negative resistance to the total resistance of the electrical system. This resistance

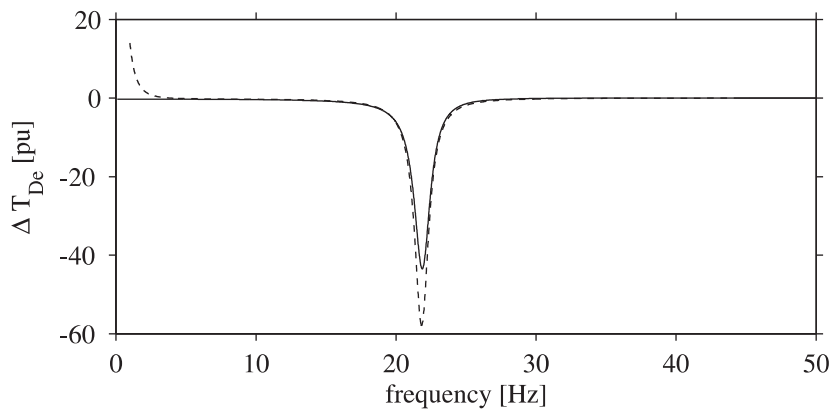


Fig. 6.14 Comparison between calculated electrical damping torque when using FSA (solid curve) and when using detailed model of synchronous generator (dashed curve).

can be computed from the impedance offered by the generator. The phase impedance (encountered by armature currents) can be calculated using the operator inductances of the synchronous machine [44, 53] as

$$Z_G(s) = R_G(s) + jX_G(s) = \frac{1}{2} [Z_{GDD}(s - j\omega_0) + Z_{GQQ}(s - j\omega_0)] + j\frac{1}{2} [Z_{GDQ}(s - j\omega_0) - Z_{GQD}(s - j\omega_0)] \quad (6.46)$$

where

$$\begin{aligned} Z_{GDD}(s) &= \frac{s x_d(1 + sT'_d)(1 + sT''_d)}{\omega_B (1 + sT'_{d0})(1 + sT''_{d0})}, & Z_{GDQ}(s) &= \frac{\omega_0 x_d(1 + sT'_d)(1 + sT''_d)}{\omega_B (1 + sT'_{d0})(1 + sT''_{d0})} \\ Z_{GQD}(s) &= -\frac{\omega_0 x_q(1 + sT'_q)(1 + sT''_q)}{\omega_B (1 + sT'_{q0})(1 + sT''_{q0})}, & Z_{GQQ}(s) &= \frac{s x_q(1 + sT'_q)(1 + sT''_q)}{\omega_B (1 + sT'_{q0})(1 + sT''_{q0})} \end{aligned} \quad (6.47)$$

with

- x_d the synchronous reactance in the d -direction;
- T'_{d0} and T''_{d0} the d -axis open-circuit transient and subtransient time constants, respectively;
- T'_d and T''_d the d -axis short-circuit transient and subtransient time constants, respectively.

Analog definition holds for the parameters in the q -direction. Figure 6.15 shows the trend of the resistance R_G and the reactance X_G as a function of the frequency. It is possible to observe that the resistance R_G presents a negative value for frequencies below the synchronous one. When the frequency ω is higher than the synchronous frequency ($\omega > \omega_0$), the resistance R_G will become positive. From Fig.6.15 it is also possible to observe that the reactance X_G is a linear

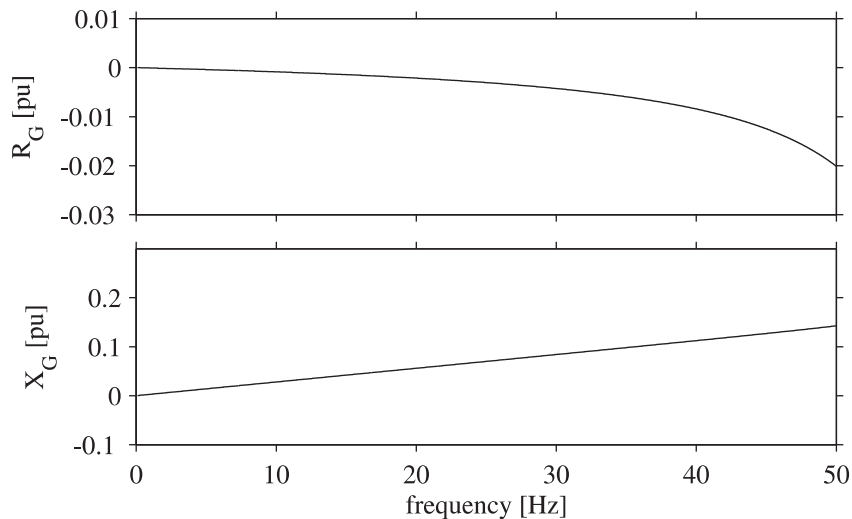


Fig. 6.15 Frequency response of generator resistance (top) and generator inductance (bottom) for IGE.

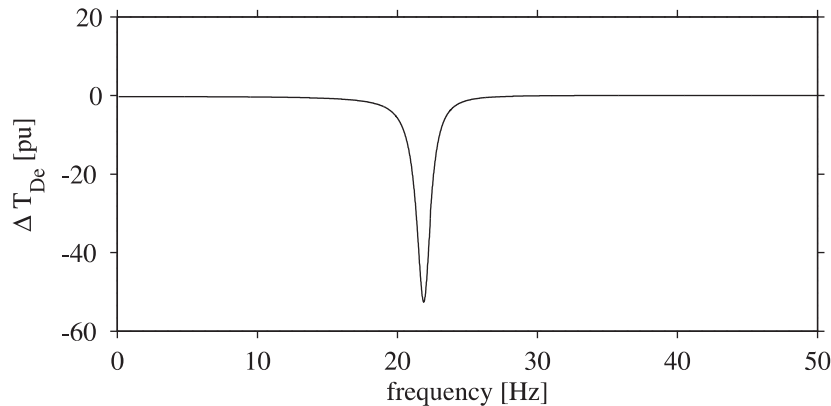


Fig. 6.16 Calculated electrical damping torque using FSA. Grid resistance corrected for IGE.

function of the frequency. Figure 6.16 shows the trend of the damping torque as a function of the frequency when the simplified model has been improved considering the negative resistance due to IGE. It is possible to observe that, although the negative damping occurs still at the same frequency, now the absolute value of its magnitude is higher (56 pu) and closer to the one obtained using the detailed model of the generator. However, it is important to remember that the effect of the IGE effect is not significant in practical applications, thus can be neglected without losing generality of the considered model.

6.10 Countermeasures to the SSR problem

As mentioned earlier in this chapter, all SSR phenomena cause stress on the shaft system in the turbine-generator string in the power plant. Without a fast action from the system operators, shaft damage can eventually occur causing lack of available power and great economical losses. An extended analysis of possible countermeasures to avoid or mitigate the risk of SSR in the power system is carried out in [53]; the following is a brief summary.

6.10.1 Power system design improvements

SSR is a phenomena that occurs under specific conditions in a series-compensated power system. A first solution to avoid the problem might be a proper choice of the series-compensation level to ensure that the network resonance frequency does not coincide with the complementary of one of the natural frequencies of the generator shaft. Although effective, this solution is not feasible, since the value of the network impedance, thus its resonance frequency, varies depending on the operating conditions of the power system.

Alternatively, the use of shunt compensation can be employed instead of series compensation. It has been shown that shunt capacitors lead to resonances above the synchronous frequency (supersynchronous range) [53]. At these frequencies, the network presents a small positive damping, i.e. they do not represent a risk for the rotor shaft. However, the use of shunt compensation

cannot completely replace the series compensation. The use of series compensation is more economically attractive and flexible. Furthermore, when series compensation is used, the angle deviation between the sending and the receiving ends of the transmission lines decreases. This improves the synchronizing strength of the power system. It is convenient, when possible, to always use a combination of shunt and series compensation.

6.10.2 Turbine-generator design improvements

The possibilities for improvements in this area are limited. Of course, it is straightforward to imagine to design the machines so that the lowest torsional frequency of the shaft system is greater than the synchronous frequency (i.e., natural frequencies of the generator-shaft system only in the supersynchronous range). This is impractical due to constraints on shaft and bearing size. The natural frequencies of the shaft can typically be varied only within a small limit. However, this will not have a greater impact on the SSR problem, due to the uncertainty of the resonant frequency of the network. Use of pole-face damping windings can reduce the negative resistance of the generator seen from the machine terminals [53]. This solution is relatively inexpensive and can be easily installed in new machines. However, it is impractical to install such windings in old machines. Moreover, this solution is effective only against SSR due to IGE, while it does not have any impact on mitigation of SSR due to TI and TA.

6.10.3 Use of auxiliary devices

The most commonly applied method for SSR mitigation is to install an auxiliary (mitigation) device in the power system. It is mainly in this direction that the research community is moving towards. Here, a brief description of some possible solutions is given.

Blocking filter

A simple method to achieve SSR mitigation is to install a blocking filter in series with the generator step-up transformer winding [22]. Typically, the filter is connected on the neutral end of the high voltage side of the transformer, as shown in Fig.6.17. Alternatively, the filter can be connected to the phases on the high voltage side of the step-up transformer. To protect the system against overvoltages, a protection device (such as a varistor, not shown for clarity of the figure) must be connected across the series filter.

This type of filter is meant to block the line current components having frequency $f_0 - f_m$. In practical installations, the rotor shaft has more than one natural frequency (i.e., the shaft is constituted by several turbine stages). In this case, the blocking filter will be constituted by several resonant circuits connected in series. Each filter will be tuned for one natural frequency of the generator-turbine shaft system. This solution is effective both for mitigation of SSR due to TI and TA and its performance is not affected by changes in the power system.

A disadvantage with this solution is that the tuning of the filter is dependent on the system frequency (which changes during normal operations and during fault conditions) and on the

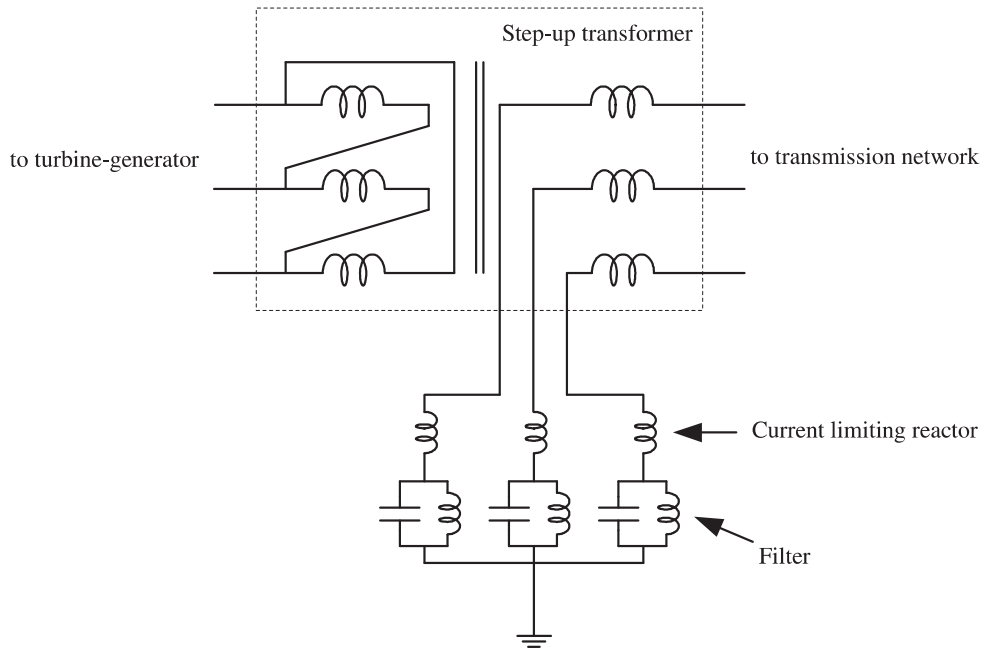


Fig. 6.17 Three-line diagram of step-up transformer with blocking filter.

variation of the filter components value due to temperature and aging.

NGH-damping scheme

The NGH-damping scheme, depicted in Fig.6.18, was first introduced by N. G. Hingorani in 1981 [32, 33] and consists of a resistor and a thyristor based ac switch connected in parallel with the series capacitor of the line. To understand the principle of operations of the NGH-scheme for SSR mitigation, the curves depicted in Fig.6.19 can be used. Consider a purely sinusoidal voltage waveform having characteristic frequency f_0 (either 50 or 60 Hz). In this case, two subsequent zero crossing will occur in a time equal to $1/(2f_0)$ (dashed curve). If the voltage is constituted by a fundamental and a subsynchronous component, some half cycles will

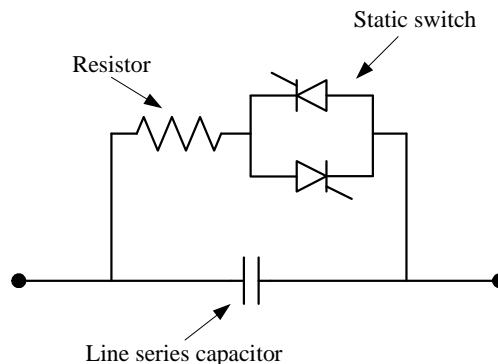


Fig. 6.18 Single-line diagram of NGH-damping scheme.

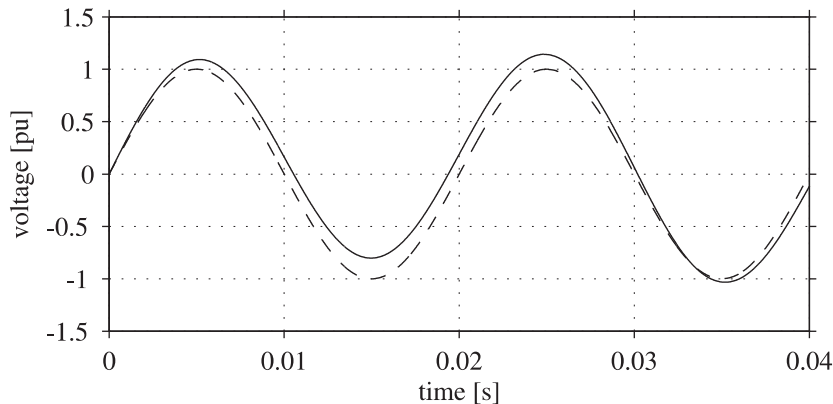


Fig. 6.19 Comparison between fundamental voltage (dashed curve) and fundamental plus subsynchronous voltage (solid curve).

be longer than $1/(2f_0)$, as it can be seen from the solid curve in the figure. The principle of the NGH-damping scheme is to dissipate capacitor charges over the resistor whenever the measured voltage half cycle period exceeds the rated value. This can be achieved by proper control of the static switch.

The control system operation is independent for each phase and does not require detection of a specific subsynchronous signal. This solution is effective in mitigation of SSR both due to TI and TA. Furthermore, the NGH scheme can be used to protect the series capacitor against overvoltages. However, studies have shown that some undamping might occur for torsional modes that are not in resonance with the electrical system [53]. This must be taken into account when installing this type of device. The NGH damping principle can be further extended to the basic TCSC circuit structure, in order to make it immune to SSR.

FACTS devices

The actual trend for SSR mitigation is to install a FACTS device in the transmission line. There are several FACTS controllers that have been proposed and developed for this purpose. Typically, FACTS controllers are divided into two main categories: shunt-connected and series-connected devices. In particular, these categories include:

- **Shunt-connected FACTS devices:** as the shunt-connected VSC described in Section 2.3.3, this type of devices are controlled to inject (or absorb) reactive power to (from) the power systems by proper control of static semiconductor valves or switches. Among the shunt-connected FACTS devices, it is important to mention the Static Var Compensator (SVC), constituted by Thyristor Controlled Reactors (TCR), Thyristor Switched Capacitors (TSC) together with passive capacitive filter banks [33]. The SVC only is intended for reactive power control. A newer device for shunt compensation is the STATCOM [53,55], which is based on VSC technology. The STATCOM can be equipped with energy storage for active power injection.
- **Series-connected FACTS devices:** as the series-connected VSC, this type of devices are

controlled to inject a voltage in series with the grid voltage. Among the series-connected FACTS devices, it is important to mention the Thyristor Controlled Switched Capacitor (TCSC) [1], the Thyristor Switched Series Capacitor (TSSC) [33] and the Static Synchronous Series Compensator (SSSC) [59].

Both in shunt and series connection, the effect of a FACTS device, seen from the generation unit terminals, is to dynamically modify the impedance of the power system. Therefore, FACTS devices represent an interesting solution to the problem of SSR mitigation. In particular, series-connected FACTS are generally considered more efficient in damping oscillations [33, 53]. Accordingly, the core of this thesis is on control of SSSC or SSR mitigation. This will be discussed in the next chapter.

6.11 Conclusions

In this chapter, an overview of the problem of subsynchronous resonance (SSR) in power systems has been given. To describe the origin of SSR due to Torsional Interaction effect (TI), a linearized model of a synchronous generator connected to a radial series-compensated transmission line has been derived. Thus, different countermeasures to the SSR problem have been described. Nowadays, FACTS controllers are considered as one of the most attractive solutions for the problem of SSR in transmission networks. In the last decade, several researchers have put their attention to the development of novel control strategies for a cost-effective way of providing power system damping at frequencies below the fundamental. This has been the driving force for this part of the project. In particular, in the next chapter a novel control algorithm for a SSSC dedicated to SSR mitigation will be derived.

Chapter 7

Control of Static Synchronous Series Compensator for SSR Mitigation

In this chapter, the control of the Static Synchronous Series Compensator (SSSC) for SSR mitigation will be described. First, the control strategy adopted in the literature will be briefly described. Then, the proposed control strategy for an SSSC dedicated to SSR mitigation will be investigated.

7.1 Introduction

In the previous chapter, the problem of subsynchronous resonance in power systems has been introduced. Analysis tools to investigate the preconditions that might lead to SSR have been discussed. Furthermore, possible countermeasures that can be adopted to avoid the risk of SSR have been described. The core of this chapter (and of this part of the thesis) is to derive and analyze a novel control strategy for a SSSC dedicated to SSR mitigation. The controller eliminates the frequency components of the line current corresponding to the natural frequencies of the turbine-generator shaft system. In the following, the proposed control system will be derived and compared with the classical approach proposed in the literature. The validity of the proposed controller to mitigate SSR due to TI effect will be shown through eigenvalue analysis of the combined mechanical-electrical system and through frequency scanning analysis. Furthermore, to investigate the effectiveness of the controller to mitigate SSR due to TA effect, time-domain simulation results will be presented. It will be shown that SSR mitigation is achieved by injecting a low magnitude voltage into the grid, leading to a reduced power rating of the SSSC and, thus, to a cost-effective solution to the SSR problem.

7.2 Classical control of SSSC for SSR mitigation

In this section, the control strategy of the SSSC for SSR mitigation proposed in the literature (here addressed to as “classical control”) will be briefly described.

Figure 7.1 shows the IEEE FBM with an SSSC installed downstream the generator step-up transformer. The voltage injected by the SSSC into the grid is denoted by \underline{u} . The SSSC is constituted by a three-phase VSC, a capacitor bank connected to the dc-side of the VSC and an injection transformer. A filtering stage (not shown in the figure for clarity) is typically added at the output of the VSC to reduce the harmonic pollution in the injected voltage. When used for reactive power compensation only, the dc capacitor is needed for proper commutation in the VSC. Otherwise, when active power injection is allowed, the dc capacitor is also used as an energy storage.

The principle of the SSR mitigation using the classical control is to replace the fundamental frequency voltage created by (at least a portion of) the inserted fixed capacitor banks by injecting a similar voltage that has been created by the SSSC. As the capacitive reactance from the capacitor bank is eliminated (or reduced), the electrical resonance of the system becomes shifted, thus avoiding the risk of SSR. The effectiveness of the classical control has been described in several publications [37, 59] and has been proved both analytically and through time-domain simulations. As an example, Fig.7.2 shows the resulting damping torque for the IEEE FBM when only fixed series compensation is used (dashed curve) and in case of hybrid compensation (fixed capacitor + SSSC, solid curve). As shown, when only fixed compensation is used, the damping torque is maximum negative at a frequency of 24.7 Hz, which is in the neighborhood of one of the natural frequencies of the generator shaft (see Table 6.1). In case of hybrid compensation, instead, the characteristic frequency of the undamped pole is moved from 24.7 to 28.2 Hz, which does not coincide with any of the torsional modes. Thus, this control strategy moves the undamping parts to frequencies that are not of danger for the generator-shaft system.

Although effective, the drawback of the classical control for the SSSC for SSR mitigation is that the device must continuously inject reactive power into the system, regardless the presence or not of SSR. Moreover, depending on the system parameters, large amount of reactive power must be injected in the system in order to change the electrical impedance seen from the generator terminals. These issues have limited the commercial exploitation of this device as a countermeasure to the SSR problem. For this reason, the driving force for this part of the

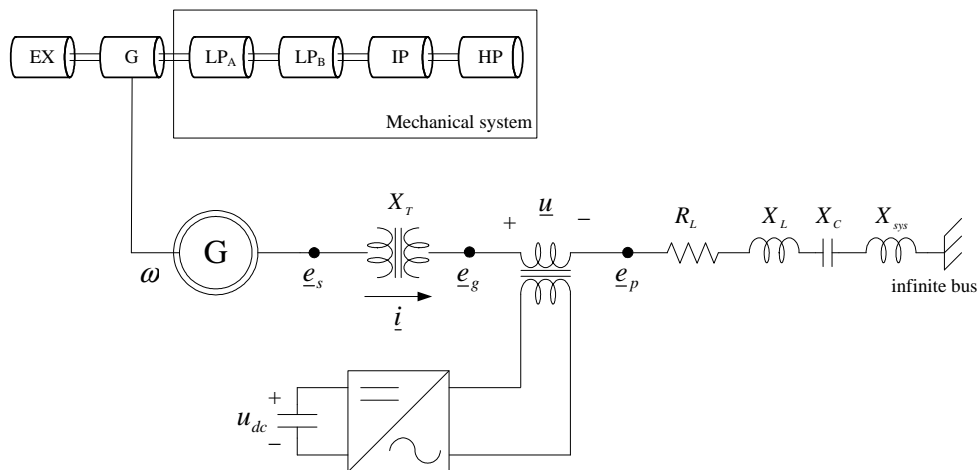


Fig. 7.1 Single-line diagram of IEEE FBM and SSSC.

7.3. Proposed control strategy for SSSC for SSR mitigation

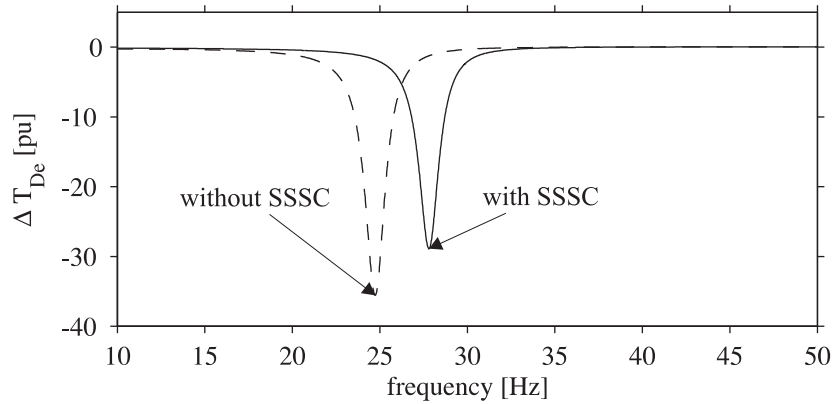


Fig. 7.2 Resulting electrical damping torque for IEEE FBM with SSSC. Classical control strategy has been adopted. Dashed curve: fixed series compensation only; solid curve: hybrid compensation (fixed capacitor and SSSC).

project was to find a more cost-effective solution to solve the problem of SSR mitigation by using SSSC. In the following, a different approach for controlling the SSSC for SSR mitigation will be presented.

7.3 Proposed control strategy for SSSC for SSR mitigation

When approaching the SSR problem, the first consideration was that this phenomenon occurs only if three conditions are fulfilled:

- The generator shaft system has a mechanical resonance at the subsynchronous frequency ω_m ;
- The generator mass must participate and be one of the swinging masses in the oscillation mode at frequency ω_m ;
- A matching electrical resonance must exist in the transmission network at the complementary frequency $\omega_0 - \omega_m$.

Therefore, the problem of SSR mitigation can be tackled in two different ways: by inspection of the resonance frequency of the network (which is the basic idea behind the classical approach), or by looking at the resonance frequencies of the generator shaft. This second option is the one considered here. As shown in Fig.6.10, the turbine-generator shaft is characterized by sharp and poorly damped resonant points. This can also be seen in Fig.7.3, where the gain of the frequency response from the input ΔT_e (expressed in pu torque) to the generator angle $\Delta\delta$ (expressed in rad) for the generator shaft system given in the IEEE FBM is depicted. From (6.29), a torsional mode will become unstable if the amplitude of the negative peak of the electrical damping torque exceeds the inherited mechanical damping at the considered frequency. Thus, SSR mitigation can be achieved by increasing the network damping only at those frequencies that are critical for the turbine-generator shaft. It is important to observe that:

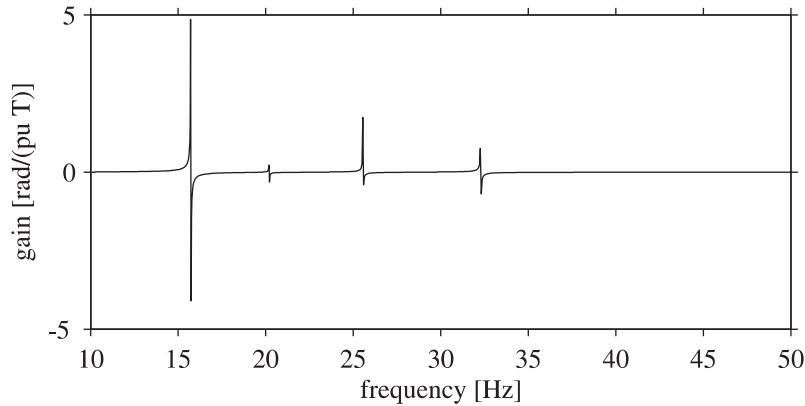


Fig. 7.3 Gain of frequency response of rotor-shaft system for IEEE FBM from input electrical torque ΔT_e to output generator angle $\Delta\delta$.

- The natural frequencies of the generator-turbine shaft system are known with fairly good accuracy and can be considered to be constant with time [4];
- Since synchronous generators are characterized by sharp resonant points (as displayed in Fig.7.3), the compensator will not interact with neighboring machines which have different resonance frequencies;
- The SSSC will be active (i.e., will inject power into the grid) only in presence of SSR.

Since the electrical damping is a function of the generator stator flux and of the line current, to achieve this goal the SSSC must control the subsynchronous component of the line current to zero. In the following, the adopted control strategy will be described.

7.4 Subsynchronous controller

As mentioned in the previous section, the basic idea behind the proposed control strategy is to control the subsynchronous component of the line current to zero. The adopted control system (here denoted as “subsynchronous controller”) is constituted by two main parts: an estimation algorithm (EA), used to estimate the subsynchronous components in the measured voltages and currents, and the subsynchronous current controller (SSCC), used to control the subsynchronous line current. These two algorithms will be described in detail in the following.

7.4.1 Subsynchronous components Estimation Algorithm (EA)

When the generator rotor oscillates around its rated speed, the voltage at the machine terminals can be expressed in the synchronous (with undisturbed rotor position) dq -coordinate systems as [53]

$$\underline{e}_s^{(dq)}(t) = \underline{e}_{s,f}^{(dq)}(t) + \underline{e}_{s,sub}^{(dq)}(t) + \underline{e}_{s,sup}^{(dq)}(t) \quad (7.1)$$

7.4. Subsynchronous controller

where the subscripts “f”, “sub” and “sup” denote the fundamental, the subsynchronous and the supersynchronous component of the measured voltage, respectively. As explained in [53], the network presents a small positive damping for frequencies above the fundamental. Therefore, the supersynchronous component is not of interest in this thesis. The subsynchronous voltage rotates clockwise in the synchronous reference frame (see Paper VII and Section 7.7). Assume that the generator rotor oscillates with angular frequency ω_m . Denoting with dq_m -plane a new set of coordinate systems that rotates synchronously with the subsynchronous voltage vector, (7.1) can be rewritten as

$$\underline{e}_s^{(dq)}(t) = \underline{e}_{s,f}^{(dq)}(t) + \underline{e}_{s,sub}^{(dq_m)}(t)e^{-j(\omega_m t)} \quad (7.2)$$

In order to extract the subsynchronous component from the measured signal, (7.2) can be rearranged so that $\underline{e}_{s,f}^{(dq)}$ and $\underline{e}_{s,sub}^{(dq_m)}$ become isolated and then applying low-pass filtering (LPF) on the resulting expression [49]. Denote the estimated quantities with the superscript $\hat{\cdot}$, the EA can be expressed as follows

$$\hat{\underline{e}}_{s,f}^{(dq)}(t) = H_f(p) \left[\underline{e}_s^{(dq)}(t) - \hat{\underline{e}}_{s,sub}^{(dq_m)}(t)e^{-j(\omega_m t)} \right] \quad (7.3)$$

$$\hat{\underline{e}}_{s,sub}^{(dq_m)}(t) = H_{sub}(p) \left[\underline{e}_s^{(dq)}(t)e^{j(\omega_m t)} - \hat{\underline{e}}_{s,f}^{(dq)}(t)e^{j(\omega_m t)} \right] \quad (7.4)$$

where, indicating with p the operator (d/dt), $H_f(p)$ and $H_{sub}(p)$ represent the transfer function of a LPF for the fundamental and for the subsynchronous component, respectively. Equation (7.4) can be rewritten in the synchronous dq -frame, yielding

$$\hat{\underline{e}}_{s,sub}^{(dq)}(t) = H_{sub}(p + j\omega_m) \left[\underline{e}_s^{(dq)}(t) - \hat{\underline{e}}_{s,f}^{(dq)}(t) \right] \quad (7.5)$$

Equations (7.3) and (7.5) can, thus, be combined together in order to extract the fundamental and the subsynchronous components of the measured voltage, as shown in Fig.7.4, where the block diagram of the described EA is depicted.

In (7.1), the voltage vector \underline{e}_s has been expressed as the sum of the fundamental plus the subsynchronous and the supersynchronous components. In actual applications, other frequency components (corresponding to the dc-offset signal, $\underline{e}_{s,0}$, and to the negative-sequence component, $\underline{e}_{s,n}$) are typically present in the measured voltage. Therefore, again neglecting the supersynchronous voltage component, the generic dq -voltage at the machine terminals can be expressed

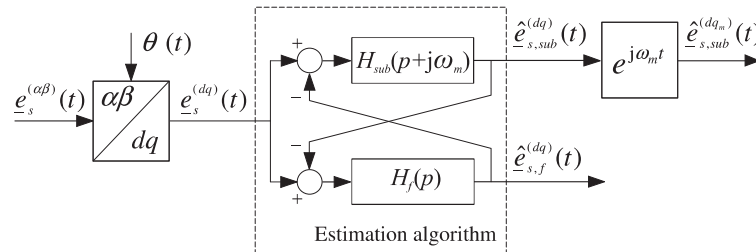


Fig. 7.4 Block diagram of subsynchronous components estimation algorithm.

as

$$\underline{e}_s^{(dq)}(t) = \underline{e}_{s,0}^{(dq)}(t) + \underline{e}_{s,f}^{(dq)}(t) + \underline{e}_{s,n}^{(dq)}(t) + \underline{e}_{s,\text{sub}}^{(dq)}(t) \quad (7.6)$$

For a proper estimation, it is convenient to estimate also these frequency components by using the EA. Under the consideration that the dc-offset component rotates clockwise in the synchronous dq -plane with angular speed ω_0 , while the negative sequence component rotates in the same direction with speed $2\omega_0$, the final algorithm describing the adopted EA is

$$\begin{aligned} \hat{\underline{e}}_{s,0}^{(dq)}(t) &= H_0(p + j\omega_0) \left[\underline{e}_s^{(dq)}(t) - \hat{\underline{e}}_{s,f}^{(dq)}(t) - \hat{\underline{e}}_{s,n}^{(dq)}(t) - \hat{\underline{e}}_{s,\text{sub}}^{(dq)}(t) \right] \\ \hat{\underline{e}}_{s,f}^{(dq)}(t) &= H_f(p) \left[\underline{e}_s^{(dq)}(t) - \hat{\underline{e}}_{s,0}^{(dq)}(t) - \hat{\underline{e}}_{s,n}^{(dq)}(t) - \hat{\underline{e}}_{s,\text{sub}}^{(dq)}(t) \right] \\ \hat{\underline{e}}_{s,n}^{(dq)}(t) &= H_n(p + j2\omega_0) \left[\underline{e}_s^{(dq)}(t) - \hat{\underline{e}}_{s,0}^{(dq)}(t) - \hat{\underline{e}}_{s,f}^{(dq)}(t) - \hat{\underline{e}}_{s,\text{sub}}^{(dq)}(t) \right] \\ \hat{\underline{e}}_{s,\text{sub}}^{(dq)}(t) &= H_{\text{sub}}(p + j\omega_m) \left[\underline{e}_s^{(dq)}(t) - \hat{\underline{e}}_{s,0}^{(dq)}(t) - \hat{\underline{e}}_{s,f}^{(dq)}(t) - \hat{\underline{e}}_{s,n}^{(dq)}(t) \right] \end{aligned} \quad (7.7)$$

where $H_0(p)$ and $H_n(p)$ are the LPF transfer functions for the dc-offset and the negative-sequence component, respectively. Observe that, in case of high harmonic pollution in the measured voltages and currents, it is convenient to improve the EA even further in order to be able to remove the harmonic components from the estimated subsynchronous quantities.

Figure 7.5 displays the frequency response (gain and phase-shift) from $\underline{e}_s^{(dq)}$ to $\underline{e}_{s,\text{sub}}^{(dq)}$ of the EA described in (7.7) when first-order LPFs are used. The oscillation frequency is assumed to be equal to 20.0 Hz ($\omega_m = 125.66$ rad/s). As shown in Fig.7.3, the natural resonance frequencies of the generator shaft can be very close to each other. Therefore, for a proper estimation of the subsynchronous components, high selectivity (corresponding to a low bandwidth) in the EA is needed. As suggested in Paper VII, the filter cut-off frequency (f_{cut}) should be no greater than one-fifth of the minimum frequency interval between two subsequent natural frequencies of the turbine-generator shaft system. Here, f_{cut} has been set to 1 Hz for all filters, yielding

$$H_i(p) = \frac{6.28}{p + 6.28}, \quad i = 0, f, n, \text{ sub} \quad (7.8)$$

Observe that the EA has the same behavior as a resonant filter with center frequency at ω_m . The algorithm presents a 1 pu gain with zero phase-shift at the frequency ω_m . Then, the gain rapidly decreases for all other frequencies. Further, the EA presents two notches at 60 and 120 Hz, i.e. at the frequencies corresponding to the dc-offset and to the negative-sequence component, respectively. Another notch, only partially visible in the figure, is at 0 Hz, corresponding to the fundamental component. The selectivity of the detection algorithm, i.e. the sharpness of the peak and the notches, depends on the selected cut-off frequency of the filters.

Details related to the practical implementation of the investigated EA (addressed to as LPF-based estimation algorithm) are reported in Paper VII. Furthermore, in the paper the LPF-based EA is compared with the recursive least square (RLS) algorithm. It is shown that the RLS algorithm presents the same behavior of the LPF-based EA when first-order LPFs are used. However, as explained in the paper, thanks to its higher flexibility, the LPF-based EA is here considered to be the best solution for the problem of subsynchronous components estimation.

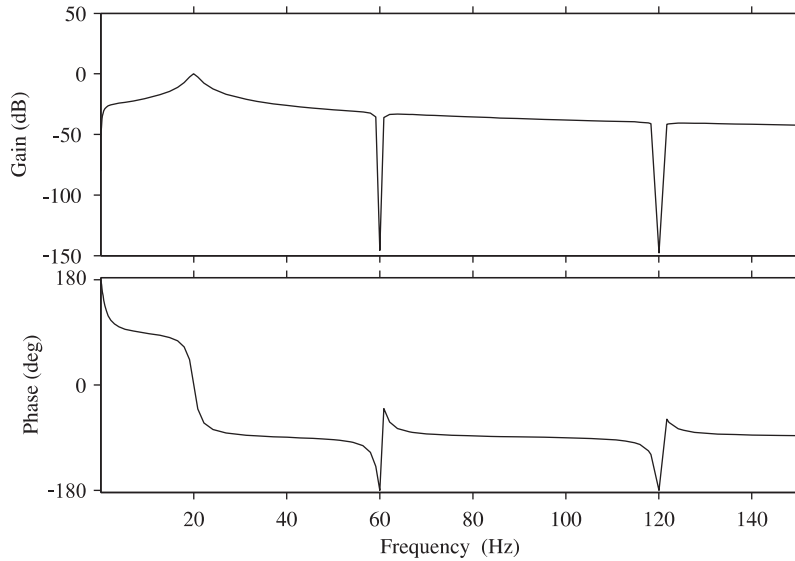


Fig. 7.5 Frequency response of estimation algorithm from $e_s^{(dq)}$ to $e_{s,sub}^{(dq)}$. First-order low-pass filters have been used. Top: gain; bottom: phase-shift.

7.4.2 Subsynchronous Current Controller (SSCC)

For this investigation, the generator is modeled as an ideal voltage source (internal bus voltage) behind the subtransient inductance of the generator, as discussed in Section 6.9. Furthermore, the infinite bus appears at subsynchronous frequencies as a short circuit. As a result, the system depicted in Fig.7.1 can be redrawn in the subsynchronous dq_m -plane as in Fig.7.6. Note that, however complex the layout of the grid between the SSSC and the infinite bus might be in reality, for instance including multiple parallel lines, this can always be represented by its Thevenin equivalent impedance. Provided that the SSSC is connected directly in series with the generator step-up transformer, the whole system can then always be modeled in the dq_m -plane as a radial single-line diagram, as in the IEEE FBM in Fig.7.6.

From the single-line diagram in Fig.7.6, the voltage behind the subtransient reactance of the

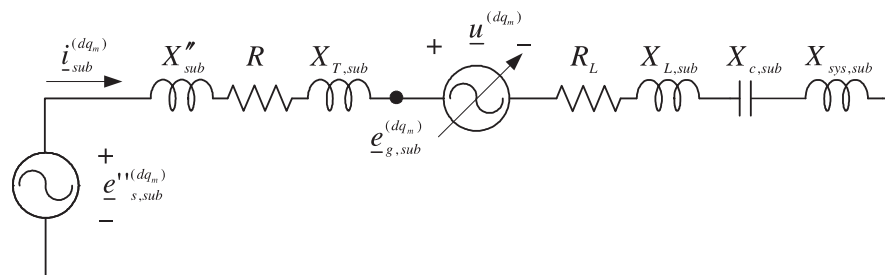


Fig. 7.6 Single-line diagram of synchronous generator connected to series compensated transmission line for SSR studies. System modeled in dq_m -reference frame.

generator in the dq_m -frame, $\underline{e}_{s,\text{sub}}''^{(dq_m)}$, can be expressed as

$$\underline{e}_{s,\text{sub}}''^{(dq_m)}(t) = \underbrace{\{R + [p + j(\omega_0 - \omega_m)](L'' + L_T)\}}_{\mathbf{Z}_1} \underline{i}_{\text{sub}}^{(dq_m)}(t) + \underline{e}_{g,\text{sub}}^{(dq_m)}(t) \quad (7.9)$$

where R , L_T and L'' are the resistance of the system upstream the SSSC (i.e. the sum of the stator resistance of the generator and the series resistance of the transformer), the leakage inductance of the transformer and the subtransient inductance of the generator, respectively. In order to control the subsynchronous current to zero, the control system has to rebuild the internal bus voltage $\underline{e}_{s,\text{sub}}''^{(dq_m)}$. Assuming that the voltage downstream the SSSC is equal to zero, i.e. treating the voltage drop over the impedance downstream the compensator as a disturbance, and with the signal references given in Fig.7.6, the law governing the controller can be written in the Laplace domain as

$$\underline{u}_{\text{sub}}^{(dq_m)}(s) = \underline{e}_{g,\text{sub}}^{(dq_m)}(s) + [R + j(\omega_0 - \omega_m)L] \underline{i}_{\text{sub}}^{(dq_m)}(s) + \left(k_p + \frac{k_i}{s}\right) \left[\underline{i}_{\text{sub}}^{(dq_m)}(s) - \underline{i}_{\text{sub}}^{(dq_m)*}(s)\right] \quad (7.10)$$

with $L = L_T + L''$. The current reference is $\underline{i}_{\text{sub}}^{(dq_m)*}$, while k_p and k_i are the proportional and the integral gains of the PI-regulator, respectively. To select the regulator gains, the closed-loop transfer function from $\underline{i}_{\text{sub}}^{(dq_m)*}$ to the actual current $\underline{i}_{\text{sub}}^{(dq_m)}$ can be shaped as a first-order LPF, where the cut-off frequency of the filter corresponds to the bandwidth of the controller [29]. Thus, calling α_{cc} the bandwidth of the SSCC, the gains become equal to $k_p = \alpha_{cc}L$ and $k_i = \alpha_{cc}R$.

Figure 7.7 shows the block diagram of the subsynchronous controller. The algorithm of the subsynchronous controller can be summarized as follows:

1. Measure grid voltages and line currents;
2. Transform all quantities from the three-phase coordinate system to the fixed $\alpha\beta$ -coordinate system and then to the rotating dq -coordinate system, using the transformation angle θ , obtained from the PLL_f;
3. Estimate the subsynchronous components of grid voltage and line current through the EA;
4. Transform the subsynchronous quantities from the dq - to the dq_m coordinate system using the transformation angle θ_m , obtained from the PLL_{sub};
5. Calculate the reference voltage $\underline{u}_{\text{sub}}^{(dq_m)*}$ through the SSCC;
6. Convert the reference voltage from the rotating dq_m -coordinate system to the three-phase coordinate system by using the transformation angle $\theta - \theta_m$;
7. Calculate the duty-cycles in the PWM block and send the switching pulses to the VSC valves.

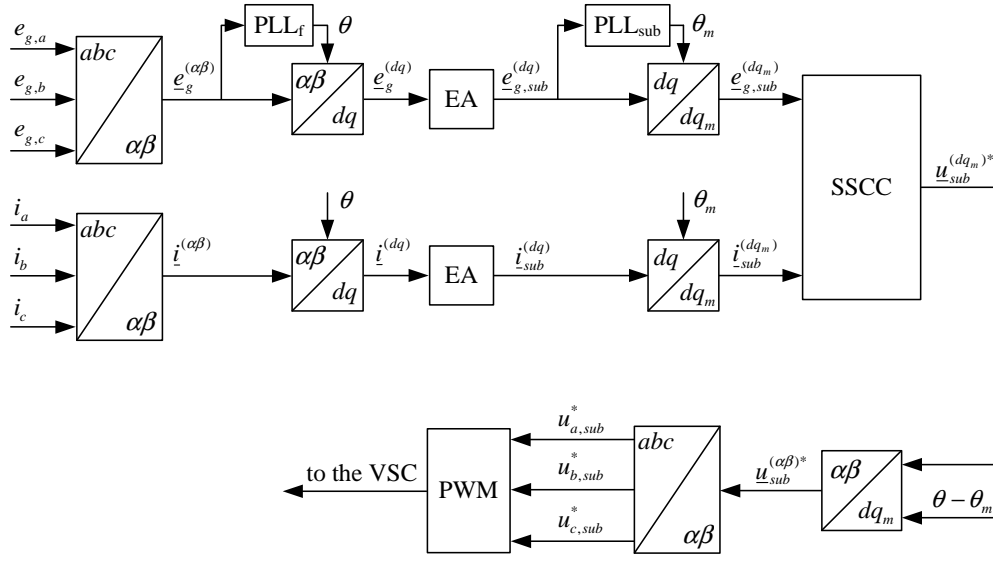


Fig. 7.7 Block-scheme of subsynchronous controller.

It is of importance to observe that the block diagram in Fig.7.7 is derived under the assumption that the rotor shaft has only one natural frequency, i.e. is constituted by only two masses (generator and one turbine stage). If more than two shaft-sections are present, such as for the IEEE FBM, the complete control system will be constituted by several controllers as the one displayed in Fig.7.7 (one for each natural frequency of the turbine-generator shaft system) connected in parallel. The outputs of each subsynchronous controller will then be added in the $\alpha\beta$ -plane.

7.5 Stability analysis

In this section, the stability analysis for the system in Fig.7.6 using the proposed control algorithm will be presented. Here, accurate knowledge of the system parameters is assumed, meaning that (7.10) contains the exact value for the impedance upstream the SSCC. Stability analysis in case of inaccurate knowledge of the impedance upstream the SSCC and when varying the series-compensation level of the transmission line is reported in Paper VIII.

The purpose of this analysis is to find the most suitable value for the controller bandwidth α_{cc} . The block diagram of the closed-loop system considered for this analysis is depicted in Fig.7.8. The process (i.e., the transfer function of the transmission network, including the subtransient inductance of the generator) and the control algorithm are implemented in the dq_m -coordinate system. The impact of the EA on the dynamics of the estimated subsynchronous voltages and currents is also included. For simplicity of the analysis, the EA is approximated to a first-order LPF.

Figure 7.9 shows the closed-loop poles placement for the investigated system when varying the controller bandwidth from 0.6283 to 31.416 rad/s. A detail of the closed-loop poles close to the origin is depicted in Fig.7.9(b) for clarity. The cut-off frequency for the LPF is set equal to

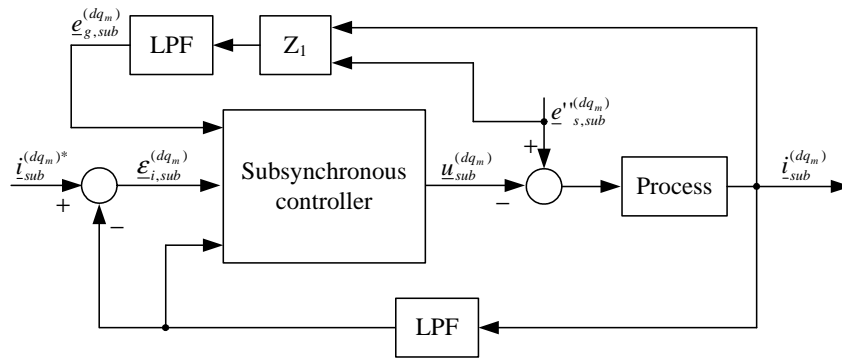


Fig. 7.8 Block-diagram of closed-loop system constituted by control system, process and estimation algorithm.

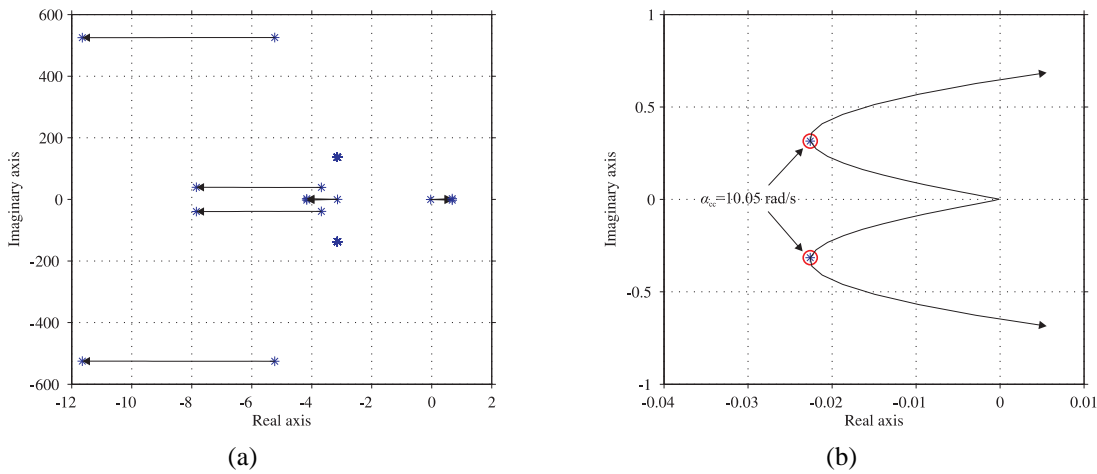


Fig. 7.9 Root locus of closed-loop control system when varying controller bandwidth α_{cc} from 0.6283 to 31.416 rad/s (a) and detail of poles close to origin (b).

1 Hz. It can be observed that when increasing the controller bandwidth, the high-frequency poles move away from the imaginary axis, while the poles close to the origin move in the opposite direction. Instability is reached for a controller bandwidth $\alpha_{cc} = 14.45$ rad/s. The selection of the controller bandwidth is a trade-off between the speed of response and the system damping. Here, a bandwidth of 10.05 rad/s, corresponding to the knee in Fig.7.9(b) has been selected.

It is of importance to observe that when deriving the block diagram in Fig.7.8, the voltage behind the subtransient inductance of the generator is considered as an input, i.e. it is assumed that this voltage is not affected by the controller dynamics. This is a reasonable assumption, since the time constant of the mechanical system is typically much larger than the electrical one. However, in case of torsional modes having very small modal inertia (leading to a small time constant for the mechanical system at the investigated frequency), this assumption might be no longer valid. In this case, carefulness must be taken when selecting the bandwidth of the controller. In particular, it is suggested to model the mechanical system using modal quantities and to include its effect in the linearized model in Fig.7.8.

7.6 Analysis of SSR due to TI effect

As already mentioned in Section 6.2, where the classification of the different types of SSR that can occur in the power system has been given, SSR due to TI effect can be analyzed using linear models. In this section, the effectiveness of the proposed control strategy for mitigation of SSR due to TI effect will be shown through the eigenvalue analysis of the combined mechanical-electrical system and through the frequency scanning analysis. For simplicity of the analysis, the controller in (7.10) has been implemented in the synchronous dq -frame, yielding [43]

$$\underline{u}_{\text{sub}}^{(dq)}(s) = \underline{e}_{\text{g,sub}}^{(dq)}(s) + (R + j\omega_0 L) \dot{\underline{i}}_{\text{sub}}^{(dq)}(s) + \left(K_p + K_i \frac{2s}{s^2 + \omega_m^2} \right) \left[\dot{\underline{i}}_{\text{sub}}^{(dq)}(s) - \dot{\underline{i}}_{\text{sub}}^{(dq)*}(s) \right] \quad (7.11)$$

7.6.1 Eigenvalue analysis

The effectiveness of the proposed control strategy when mitigating SSR due to TI effect can be investigated from an eigenvalue analysis of the closed-loop system of the combined mechanical-electrical system in Fig.7.10. As a difference compared to the closed-loop system described in Fig.6.9, the electrical system includes the SSSC with the proposed subsynchronous controller. The detailed block-scheme of the electrical system considered for this investigation is depicted in Fig.7.11. Refer to Section 6.9 for details of (6.32), (6.39) and the admittance matrix \mathbf{Y} .

The series-compensation level of the transmission network is equal to 60%. Table 7.1 shows the eigenvalues (real and imaginary part) of the IEEE FBM without and with the SSSC. From the results obtained from the stability analysis, the SSCC bandwidth is equal to 10.05 rad/s, while $f_{\text{cut}} = 1$ Hz. As shown, due to the selected series-compensation level, the closed-loop system without SSSC presents four unstable poles. The inclusion of the SSSC leads to a stable system, thus reducing the risk of SSR.

7.6.2 Frequency scanning analysis

It is of interest to observe how the electrical damping torque ΔT_{De} is modified when the SSSC with the proposed control strategy is connected to the grid. For this analysis, the block diagram for the electrical system depicted in Fig.7.11 has been considered. Assume that the generator

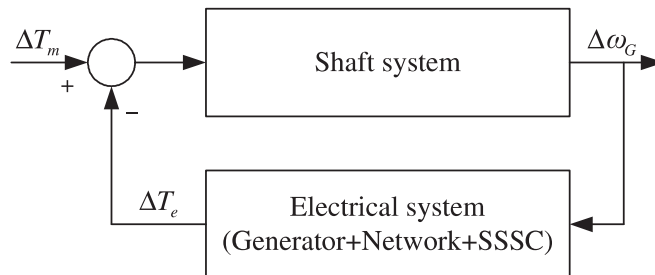


Fig. 7.10 Block-diagram of combined mechanical-electrical system for SSR studies. Electrical system includes SSSC with proposed subsynchronous controller.

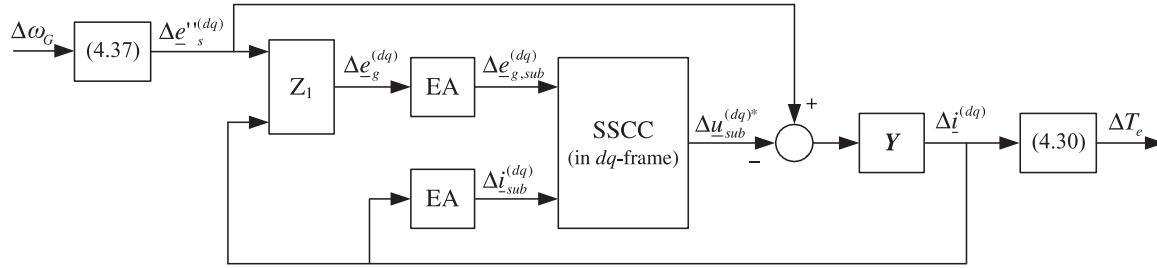


Fig. 7.11 Block-diagram of electrical system for study of SSR due to TI effect.

TABLE 7.1: Calculated eigenvalues for IEEE FBM.

without SSSC		with SSSC	
Re [s ⁻¹]	Im [rad/s]	Re [s ⁻¹]	Im [rad/s]
-4.35	±598.68	-4.35	±598.68
-2.2 e ⁻¹⁷	±298.18	-1.47 e ⁻⁶	±298.18
0.007	±202.82	-0.007	±202.82
0.52	±160.03	-0.0006	±160.57
-4.95	±155.58	-3.97	±156.57
0.01	±127.04	-7.17	±127.5
0.043	±99.54	-0.06	±98.97

shaft has a natural frequency at 24.7 Hz, coinciding with the electrical resonance of the grid (at the complementary frequency $60 - 24.7 = 35.3$ Hz). Figure 7.12 shows a comparison between the resulting damping torque for the investigated system when the compensator is in idle mode (dashed curve) and when the compensator is online (solid curve). As shown, when the SSSC is online, the pole corresponding to the system undamping has been split into two new poles located at the sidebands of the original pole (23.92 and 25.4 Hz). The damping torque at the critical frequency for the generator shaft ω_m is equal to zero. In this way, the risk of SSR due to TI can be avoided.

The selected bandwidths of the EA and of the SSSC will, of course, impact the resulting damping torque. These results are reported in Paper IX. In particular, it is found that an increased bandwidth in the SSSC leads to a wider range of frequencies where the controller modifies the damping torque, thus to higher amount of injected voltage. Therefore, the selection of the controller parameters is a trade-off between the desired speed of response and the voltage rating (thus, the cost) of the SSSC. However, it is of importance to remember that SSR is typically a slow phenomenon, thus, low bandwidth for the SSSC is suggested.

The difference between the proposed control strategy and the classical control in Fig.7.2 is clearly visible. As shown in Fig.7.12, with the proposed control system the SSSC will act only at the critical frequency ω_m . Therefore, SSR mitigation can be achieved by injecting low amount of voltage into the grid, resulting in a reduced power rating of the compensator. This concept will be shown in the next section.

7.7. Evaluation of voltage requirements for SSSC for SSR mitigation

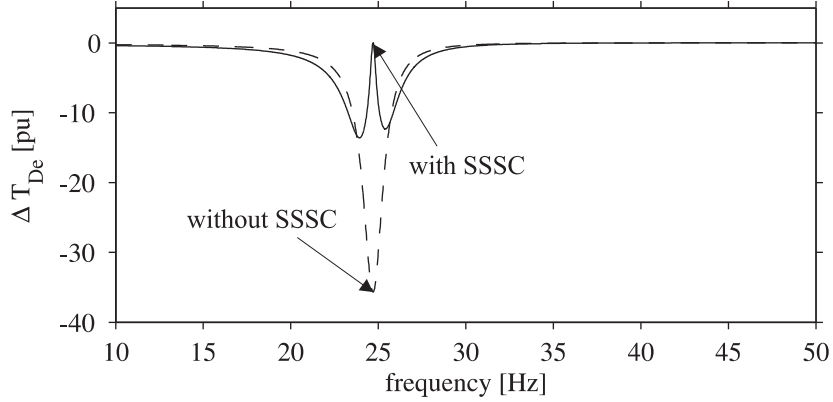


Fig. 7.12 Resulting electrical damping torque for investigated system with proposed control strategy. Dashed curve: SSSC in idle mode; solid curve: SSSC online.

7.7 Evaluation of voltage requirements for SSSC for SSR mitigation

As mentioned in the previous sections, with the proposed control strategy the controller must rebuild the subsynchronous component of the internal bus voltage. Beside the characteristics of the considered system, the amount of voltage injected by the SSSC into the grid during SSR mitigation operation depends on the controller parameters, i.e. on the bandwidths of the EA and SSCC. However, to evaluate the voltage requirements for the SSSC, it can be assumed the injected voltage is exactly equal to the subsynchronous voltage $\underline{e}_{s,\text{sub}}''$, i.e.

$$\underline{u}_{\text{sub}}^* = \underline{e}_{s,\text{sub}}'' \quad (7.12)$$

To derive this subsynchronous voltage, the generic case of a synchronous generator connected to a transmission line can be considered. The interaction between the electrical and the mechanical system can be simulated by applying an oscillating speed ω to the generator shaft [53]. The per-unit voltage at the generator terminals can be written in the $\alpha\beta$ -plane as

$$\underline{e}_s''^{(\alpha\beta)}(t) = e_{s,\alpha}''(t) + j e_{s,\beta}''(t) = \bar{\omega}(t) E_s'' e^{j[\omega_0 t + \delta(t)]} \quad (7.13)$$

where E_s'' is the amplitude of the voltage vector at rated speed, δ is its phase displacement, $\bar{\omega}$ is the per-unit rotor speed and ω_0 is the fundamental frequency expressed in rad/s. If the generator rotor oscillates around ω_0 , its per-unit speed can be expressed as

$$\bar{\omega}(t) = \bar{\omega}_0 + A \sin(\omega_m t) \quad (7.14)$$

where A is the amplitude of the oscillation and ω_m is the oscillation frequency (in rad/s) of the rotor. Substituting (7.14) in (7.13), the α -component of the voltage can be written as

$$\begin{aligned} e_{s,\alpha}''(t) &= [\bar{\omega}_0 + A \sin(\omega_m t)] E_s'' \cos[\omega_0 t + \delta(t)] = \bar{\omega}_0 E_s'' \cos[\omega_0 t + \delta(t)] + \\ &+ \frac{A E_s''}{2} \{-\sin[(\omega_0 - \omega_m)t + \delta(t)] + \sin[(\omega_0 + \omega_m)t + \delta(t)]\} \end{aligned} \quad (7.15)$$

The derivative of the rotor angle δ is given by

$$\frac{d\delta(t)}{dt} = [\bar{\omega}(t) - \bar{\omega}_0]\omega_B = A \sin(\omega_m t)\omega_B \quad (7.16)$$

Therefore, by integrating both sides of (7.16) and calling δ_0 the rotor angle in steady-state conditions, the rotor angle can be expressed as

$$\delta(t) = \delta_0 - A \frac{\omega_B}{\omega_m} \cos(\omega_m t) \quad (7.17)$$

Substituting (7.17) in (7.15) and after some algebraic manipulations, the α -component of the voltage behind the subsynchronous inductance of the generator is given by

$$e''_{s,\alpha}(t) = \bar{\omega}_0 E''_s \cos(\omega_0 t + \delta_0) + \frac{A E''_s}{2\omega_m} \{(\omega_0 - \omega_m) \sin[(\omega_0 - \omega_m)t + \delta_0] + (\omega_0 + \omega_m) \sin[(\omega_0 + \omega_m)t + \delta_0]\} \quad (7.18)$$

Analogously, the β -component of the voltage is found to be equal to

$$e''_{s,\beta}(t) = \bar{\omega}_0 E''_s \sin(\omega_0 t + \delta_0) + \frac{A E''_s}{2\omega_m} \{-(\omega_0 - \omega_m) \cos[(\omega_0 - \omega_m)t + \delta_0] - (\omega_0 + \omega_m) \cos[(\omega_0 + \omega_m)t + \delta_0]\} \quad (7.19)$$

As shown in (7.18) and (7.19), when a small oscillation is applied to the generator rotor, the internal bus voltage will be constituted by the sum of three terms: one term rotating at the rated frequency plus two terms oscillating with frequencies of $\omega_0 + \omega_m$, corresponding to the supersynchronous voltage component, and $\omega_0 - \omega_m$, corresponding to the subsynchronous component. In particular, from (7.18) and (7.19), the subsynchronous voltage component is given by

$$\begin{aligned} \underline{e}''_{s,\text{sub}}^{(\alpha\beta)}(t) &= \frac{A E''_s}{2\omega_m} (\omega_0 - \omega_m) \{ \sin [(\omega_0 - \omega_m)t + \delta_0] - j \cos [(\omega_0 - \omega_m)t + \delta_0] \} = \\ &- \frac{A E''_s}{2\omega_m} (\omega_0 - \omega_m) e^{j[(\omega_0 - \omega_m)t + \delta_0 + \pi/2]} \end{aligned} \quad (7.20)$$

meaning that the subsynchronous voltage vector rotates in the positive direction (counterclockwise) in the $\alpha\beta$ -plane.

The voltage vector $\underline{e}''_{s}^{(\alpha\beta)}$ can be further transformed in the synchronous dq -plane as

$$\underline{e}''_{s}^{(dq)}(t) = \underline{e}''_{s}^{(\alpha\beta)}(t) e^{-j\omega_0 t} = \underline{e}''_{s,f}^{(dq)}(t) + \underline{e}''_{s,\text{sub}}^{(dq)}(t) \quad (7.21)$$

where $\underline{e}''_{s,f}^{(dq)}$ is the dq -voltage vector at the fundamental frequency. The subsynchronous voltage component is given by

$$\underline{e}''_{s,\text{sub}}^{(dq)}(t) = \underline{e}''_{s,\text{sub}}^{(\alpha\beta)}(t) e^{-j\omega_0 t} = -\frac{A E''_s}{2\omega_m} (\omega_0 - \omega_m) e^{-j(\omega_m t + \delta_0 + \pi/2)} \quad (7.22)$$

7.7. Evaluation of voltage requirements for SSSC for SSR mitigation

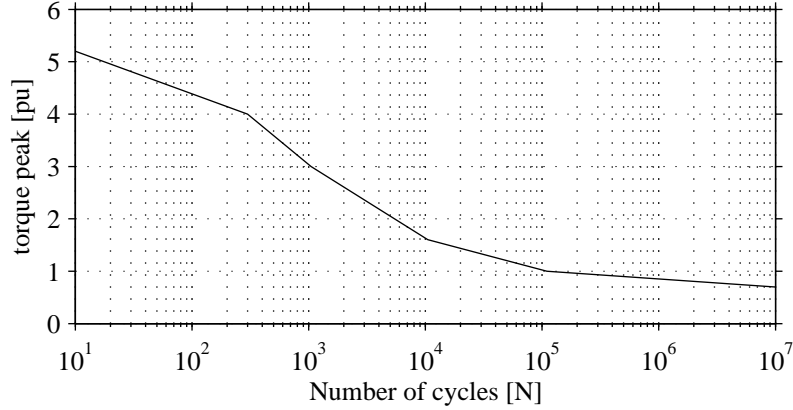


Fig. 7.13 Maximum peak torque vs number of cycles for turbine-generator shaft before shaft crack initiation (from [5]).

From (7.22) it can be observed that although the subsynchronous component of the voltage $\underline{e}_{s,\text{sub}}''^{(\alpha\beta)}$ rotates in the positive direction in the fixed $\alpha\beta$ -plane, the same vector rotates clockwise in the plane that rotates synchronously with the rated frequency of the system.

From (7.20) and (7.22), the amplitude of the subsynchronous voltage $\underline{e}_{s,\text{sub}}''$ (in pu) depends on the triggered frequency ω_m and on the oscillations amplitude A only. Therefore, with the proposed approach, the voltage requirements for the SSSC are only related on the mechanical characteristics of the considered generator, while are independent on the power system parameters.

Example: Calculation of maximum expected subsynchronous voltage component for IEEE FBM

The purpose of this example is to calculate the maximum subsynchronous component of the internal bus voltage that can be expected when considering the IEEE FBM. From the swing equations given in Section 6.6, the term A is a function of the torque applied to the generator shaft. It has been shown through the modal analysis in Section 6.6.1 that the shaft system reacts differently depending on the characteristic frequency of the applied torque. In the specific case of the turbine-generator shaft system given in the IEEE FBM, it was found that the most critical mode shape is the first one, corresponding to a characteristic frequency of 98.72 rad/s.

To select the amplitude of the torque applied to generator shaft, the S-N curve in Fig.7.13 has been considered [5]. This curve gives the maximum peak torque that can be applied to a turbine section, before crack initiation, as a function of the number of cycles. From the figure it can be observed that the maximum torque that can be applied to a shaft without direct failure is about 5 pu. Therefore, it is here assumed that the electrical torque T_e applied to the generator shaft has an amplitude of 5 pu and a characteristic frequency of 98.72 rad/s. With the mentioned values, the amplitude of the angular frequency oscillations (first peak) is $A = 0.049$ pu. Substituting this value in (7.20) and assuming $E_s'' = 1$ pu, the amplitude of the subsynchronous voltage component is equal to

$$|\underline{e}_{s,\text{sub}}^{n(\alpha\beta)}| = \frac{AE_s''}{2\omega_m}(\omega_0 - \omega_m) = \frac{0.049}{2 \cdot 98.72}(376.99 - 98.72) = 0.06 \text{ pu} \quad (7.23)$$

Therefore, it can be observed that even in case of large torques applied to the generator shaft, the initial amplitude of the subsynchronous component of the internal bus voltage is only 6% of the rated voltage. This proves that, with the proposed approach, SSR mitigation can be achieved with very low voltage injection.

7.8 Dc-link voltage controller (DCVC)

The control system for the SSSC must be completed with a dc-link voltage controller, to control the voltage u_{dc} across the dc-link capacitor. The problem of controlling the voltage of the dc link of the VSC can be reformulated as controlling the active power flowing into the VSC. In particular, the objective of the DCVC is to calculate a voltage \underline{u}_f , at the fundamental frequency, of appropriate amplitude that is in phase with the line current. Under the assumption that the VSC is lossless, the power flowing into the dc link (p_{VSC}) must be equal to the energy stored in the dc capacitor w_c , yielding

$$\frac{dw_c(t)}{dt} = p_{\text{VSC}}(t) \quad (7.24)$$

where the energy w_c is given by

$$w_c(t) = \frac{1}{2}C_{dc}u_{dc}^2(t) = \frac{1}{2}C_{dc}W(t) \quad (7.25)$$

with $u_{dc}^2 = W$. The voltage injected by the SSSC is constituted by the sum of a fundamental and a subsynchronous component. Assuming that the dc capacitor of the VSC is large enough to provide appropriate filtering at subsynchronous frequencies, the active power p_{VSC} can be expressed as

$$p_{\text{VSC}}(t) = \underline{u}_f \dot{i} = |\underline{u}_f| |\dot{i}| \quad (7.26)$$

since, as mentioned earlier, the injected fundamental voltage vector \underline{u}_f is taken to be in phase with the line current \dot{i} . Assuming that the dc link is purely capacitive, the transfer function from the amplitude of the fundamental injected voltage $|\underline{u}_f|$ to the term W is equal to

$$G_{dc}(s) = \frac{2|\dot{i}|}{sC_{dc}} \quad (7.27)$$

To derive the control law, (7.24) can be linearized as

$$C_{dc}u_{dc,0} \frac{d\Delta u_{dc}}{dt} = \Delta p_{\text{VSC}} \quad (7.28)$$

where $u_{dc,0}$ is the operating point of the dc-link voltage. As shown, the closed-loop dynamics depend on the operating point. This inconvenience can be avoided by using the square of the

7.8. Dc-link voltage controller (DCVC)

dc voltage when deriving the control law, as suggested in [52]. As for the current controller described in Section 7.4.2, the DCVC can be shaped as a first order LPF having bandwidth α_{dc} , yielding a P-controller having a gain of $k_{p,dc} = \alpha_{dc}C_{dc}/(2|\underline{i}|)$, [52]. In addition to the proportional controller, a small integral term $k_{i,dc}$ can be employed in the controller law, in order to remove steady-state impact of mismatch between the actual and the modeled system. As a result, the reference voltage \underline{u}_f is given by

$$|\underline{u}_f| = \left(k_{p,dc} + \frac{k_{i,dc}}{s} \right) \frac{u_{dc}^2(s) - u_{dc}^{2*}}{2}, \quad \angle \underline{u}_f = \angle \underline{i} \quad (7.29)$$

Figure 7.14 shows the step response of the investigated DCVC. The bandwidth of the DCVC is equal to 6.28 rad/s. At start, the reference voltage is set equal to 0.3 pu and the dc-link is totally discharged. At $t = 2$ s, the VSC is enabled and the dc-link charges up to the reference voltage. Then, steps in the reference voltage are applied. As shown, the control system works properly and presents the desired step response.

DCVC bandwidth selection

The objective of the DCVC is to control the active power p_{VSC} only. To avoid interactions with the SSCC, the DCVC should not react at the frequency component ω_m . Therefore, it is convenient to set the bandwidth α_{dc} at least five times lower [68] than the lowest natural frequency of the generator shaft. Low ratio between the controlled subsynchronous frequency ω_m and the DCVC bandwidth leads to a less damped system, resulting in a longer settling time to control the subsynchronous current down to zero (see Paper X). From a control point of view, it is more convenient to set α_{dc} ten times lower than the lowest natural frequency of the generator shaft, as suggested in [52]. On the other hand, if a perturbation occurs in the power system, the generator-shaft system will swing as a unique mass. These oscillations, typically of a few Hz, are damped by the damping windings of the synchronous generator. This results in low-frequency oscillations affecting the dc link of the VSC. To reduce the ratings of the dc side, it is desirable to use the DCVC to damp these oscillations by selecting α_{dc} sufficiently high. Therefore, the selection of the bandwidth α_{dc} is a trade-off between the overrating of the dc-side and the maximum time

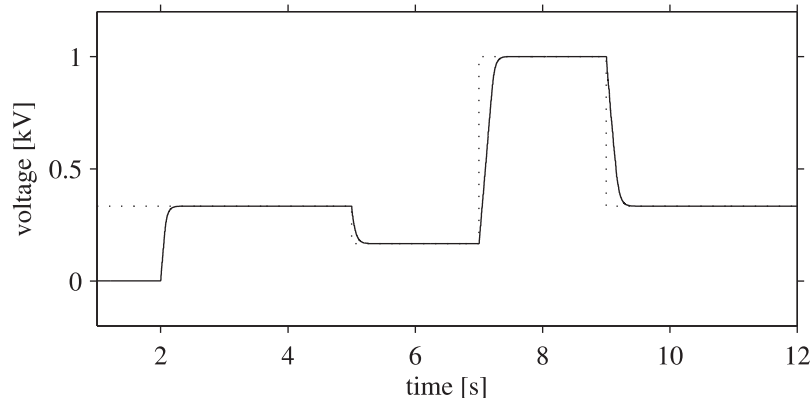


Fig. 7.14 Simulated step response of DCVC. Solid: actual voltage; dashed: reference voltage.

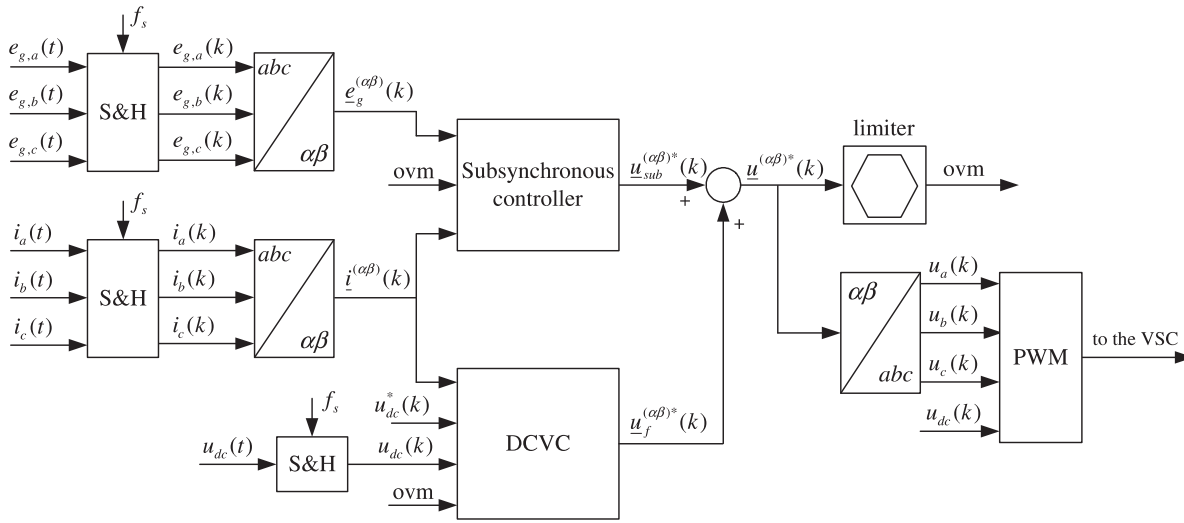


Fig. 7.15 Block-diagram of SSSC control system for SSR mitigation.

allowed to control the subsynchronous current to zero. As an example, for the IEEE FBM, the oscillation frequency due to rotor swing is expected to be below 2 Hz [53]. Therefore, in this case, a bandwidth $\alpha_{dc} = 12.57$ rad/s (corresponding to 2 Hz) is suggested.

7.9 SSSC control structure

The structure of the complete control system for the SSSC is depicted in Fig.7.15. Measured grid voltages and line currents are discretized with sampling frequency f_s . To be implemented in a digital controller, the EA, the SSCC and the DCVC are discretized with a sampling time of $T_s = 1/f_s$. As shown in the figure, the DCVC is connected in parallel to the subsynchronous controller. Output of the control system is the injected voltage reference \underline{u}^* , constituted by the sum of the subsynchronous voltage \underline{u}_{sub}^* output of the subsynchronous controller and the fundamental voltage component, \underline{u}_f^* , output of the DCVC. These two voltages are added up in the $\alpha\beta$ -coordinate systems. The resulting voltage is then transformed to the three-phase coordinates and sent to the PWM block to calculate the switching signals for the VSC valves. Note that the signal $\underline{u}^{(\alpha\beta)*}$ is passed through a limitation block that checks if the reference voltage vector exceeds the boundary of the hexagon described in Section 3.3.2. If saturation occurs, the overmodulation signal “ovm” will be equal to 1 (0 otherwise). In this case, to avoid integration windup, the integrators in the SSCC and in the DCVC will be inhibited. It is of importance to observe that, as a difference compared with the saturation strategy adopted for the SSC and for the shunt-connected VSC, in case of saturation the amplitude of the reference voltage vector is not limited. Thus, since the VSC will operate in its non linear region, low frequency harmonics will appear in the injected voltage. However, as already mentioned earlier, the voltage injected by the SSSC during SSR mitigation operations is only a few percent of the rated voltage of the system. Therefore, this will not have an impact of the power quality of the grid voltage.

7.10 Simulation results

In Section 7.6, the effectiveness of the investigated control algorithm to mitigate SSR due to TI has been shown through eigenvalue and frequency scanning analysis. Here, time-domain simulation results for the SSSC with the proposed control strategy for mitigation of SSR due to TA effect will be presented. Simulations have been carried out using the simulation program PSCAD/EMTDC and the control system has been implemented using Fortran 90 language. The selected sampling frequency is equal to $f_s = 1.2$ kHz. One particular remark should be made for the two PLLs in Fig.7.7. The purpose of the first PLL (denoted as PLL_f and used to determine the transformation angle θ) is to track the phase-angle of the fundamental component of the grid voltage \underline{e}_g only. Moreover, the PLL must be able to follow the dynamics of the machine due to rotor swing (typically in the range of a few Hz). For these reasons, the bandwidth of the PLL (denoted as $\alpha_{\text{PLL},f}$) is set equal to 18.85 rad/s. The purpose of the second PLL (PLL_{sub}), instead, is just to estimate the transformation angle θ_m . This angle must be insensitive to system disturbances, thus, the bandwidth of the PLL_{sub} is set equal to 6.28 rad/s. Observe that the PLL_{sub} is enabled only in presence of oscillations having reasonable amplitude. In absence of subsynchronous voltage component (i.e. when the amplitude of the estimated subsynchronous component is below a predefined threshold, here equal to 0.005 pu), this PLL will not be active and the transformation angle θ_m is obtained by integrating the calculated frequency ω_m .

The dynamic performance of the SSSC when mitigating SSR due to short-circuit faults in the power system is reported in Papers VIII to X. Furthermore, in Paper IX, the effect of variation of control system parameters on the overall performance of the system is discussed. Finally, Paper X proposes the use of a single-phase VSCs based SSSC dedicated to SSR mitigation.

In all papers, the IEEE FBM has been considered. It is of importance to observe that, beside its simplicity, the advantage of using the IEEE FBM over other benchmark models is that the considered generator-shaft system is constituted by a large number of masses. This leads to a greater complexity when deriving the control system, since the natural frequencies of the generator-shaft are very close to each other. Furthermore, a radial resonance leads to a fairly deep negative electrical damping (deeper, for example, as compared with the parallel resonance case), thus to higher amount of voltage needed to control the subsynchronous current to zero. However, one objection could be that the network model considered in the IEEE FBM does not represent a realistic system. For this reason, in this section simulation results obtained when using the IEEE Second Benchmark Model (SBM) [24] will be presented.

Figure 7.16 shows the single-line diagram of the IEEE SBM. The model consists of a single generator connected to two lines, one of which is series compensated (line 1). As compared with the IEEE FBM in Fig.7.1, it can be noted that the turbine-generator shaft system is constituted by four masses only: an high pressure turbine stage, a low pressure, the generator and the exciter. The system parameters for the IEEE SBM are reported in Appendix B.

From the eigenvalue analysis of the mechanical system, the natural frequencies are 24.65, 32.39 and 51.10 Hz. For this benchmark model, the value of the series capacitor is not given. Here, a compensation value of 50% has been chosen in the compensated line, since this provides the best tuning for the first torsional mode. This can be observed in Fig.7.17, where the electrical

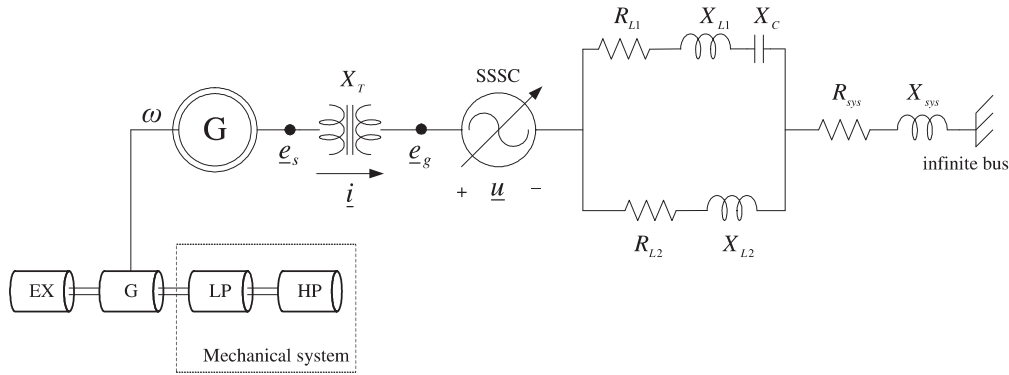


Fig. 7.16 Single-line diagram of IEEE SBM and SSSC.

(top) and mechanical (bottom) damping torques for the considered system are depicted.

As shown in Fig.7.16, here the SSSC has been implemented as a controlled ideal voltage source. The reason for this choice is that the bandwidth of the proposed controller is very small. Furthermore, as mentioned in Section 7.4.1, the estimation algorithm has the same characteristic of a resonant filter having center frequency at the natural frequency ω_m . As a result, assuming that the DCVC and the SSCC do not interact (see Paper X), even a moderate switching frequency will not have an impact on the resulting transfer function. Observe that for the system in Fig.7.16, the subsynchronous controller is still designed as in (7.10) and its bandwidth is kept equal to 10.05 rad/s.

In order to study a critical case of torque amplification, a three-phase fault has been applied directly downstream the SSSC. The fault is applied at $t = 12$ s and its clearing time is assumed to be 100 ms. With the selected level of series compensation, excitation of the first and second torsional mode of the shaft assembly will occur, leading to high shaft torques at the cou-

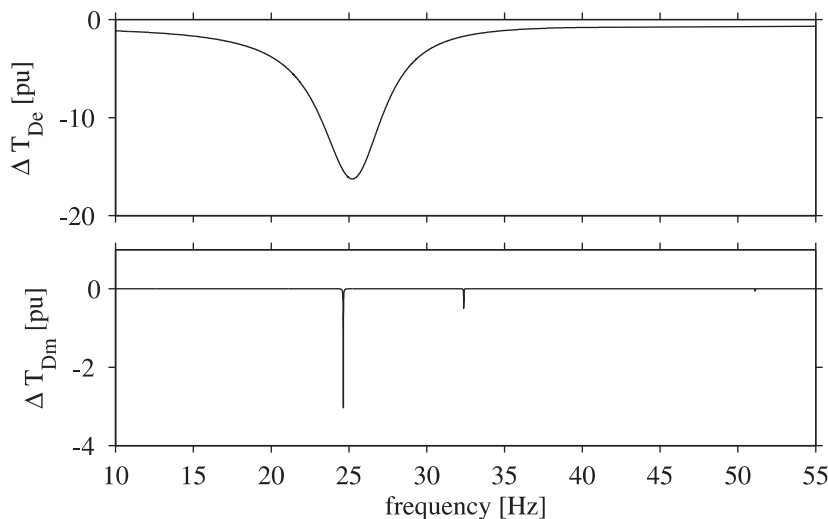


Fig. 7.17 Comparison between electrical damping (top) and mechanical damping (bottom) for IEEE SBM.

plings HP-LP and GEN-LP. This can be observed from Fig.7.18, where the simulated torques between the different sections of the turbine-generator system when the SSSC is in idle mode are depicted.

When the compensator is active, the system will react to control the subsynchronous components of the line current to zero. Figure 7.19 shows the controlled voltage components output of the subsynchronous current controllers in the corresponding dq_m -coordinate systems, while Fig.7.20 shows the estimated subsynchronous components of the line current in the corresponding subsynchronous reference frames. As expected from Fig.7.17, due to the selected series-compensation level, the dominant subsynchronous frequency component will be the first one, having a characteristic frequency of 24.65 Hz ($\omega_{m1} = 154.88$ rad/s). It can be observed from Fig.7.20(a) that the subsynchronous current is equal to zero before the fault. After the fault is cleared, the subsynchronous current raises up to about 0.8 pu. Then, the SSSC slowly controls this current component to zero. As a result, the turbines of the generator shaft will still experience oscillations due to the perturbation in the grid, but they will be damped and slowly go back to the pre-fault value, as displayed in Fig.7.21. From the figure it can be observed that the maximum peak torque is equal to 2 pu. However, this torque oscillations will withstand for a few cycles only. Therefore, they do not represent a risk for the generator shaft, as it can be seen from the S-N curve in Fig.7.13.

Figure 7.22 shows the simulated rotor speed, while its FFT is depicted in Fig.7.23. From these figures it can be noted that directly after the fault has been cleared, the rotor speed is mainly affected by two frequency components in addition to the dc quantity: one at 1.5 Hz and one at 24.6 Hz. The frequency of 1.5 Hz is due to the rotor swing after the fault. This component will decay with the time constant of the damping windings in the synchronous generator. The other

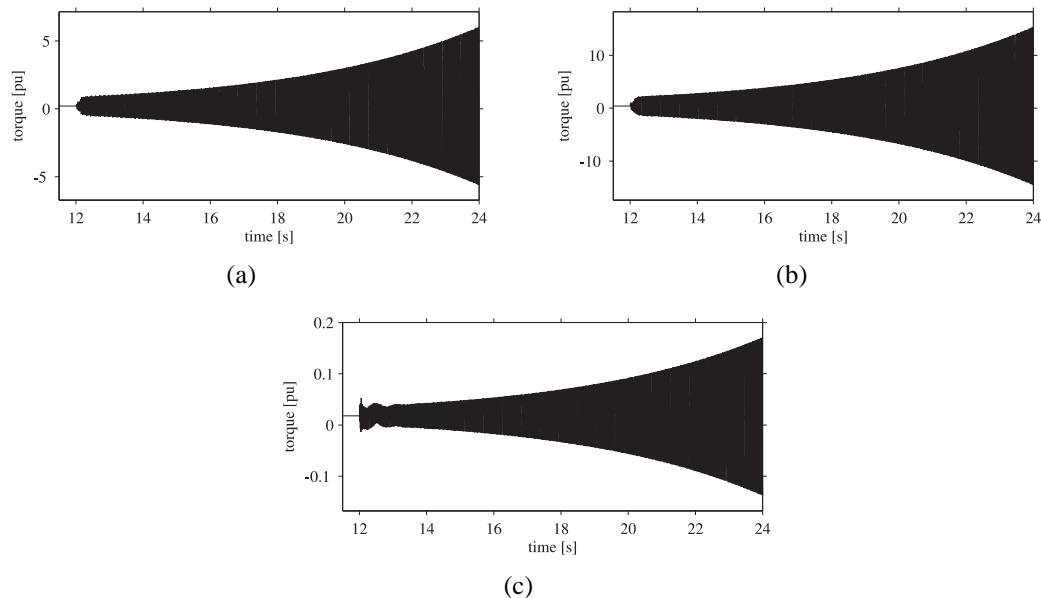


Fig. 7.18 Simulated generator shaft torques for IEEE SBM. SSSC in idle mode. Plot a: HP-LP torque; Plot b: LP-GEN torque; Plot c: GEN-EX torque.

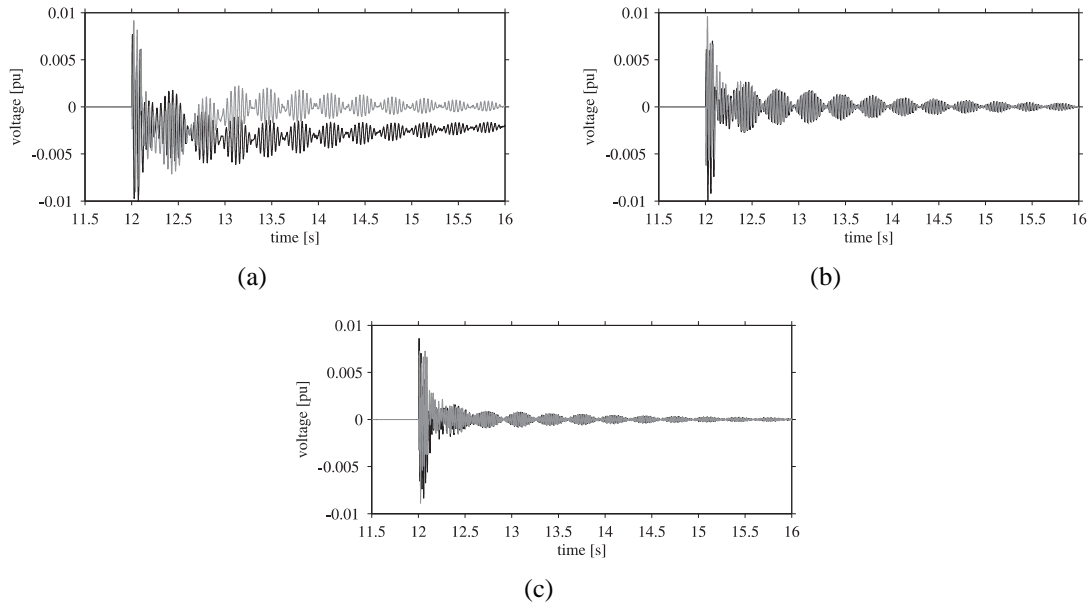


Fig. 7.19 Voltage components output of SSCs in corresponding subsynchronous reference planes. Plot a: $\omega_{m1} = 154.88$ Hz; Plot b: $\omega_{m2} = 203.51$ Hz; Plot c: $\omega_{m3} = 321.07$ Hz. Black curve: d_m component; gray curve: q_m component.

frequency component, instead, corresponds to the triggered subsynchronous resonance and will be damped out by the subsynchronous controller.

Finally, Fig.7.24 shows the voltage injected by the SSSC during SSR mitigation operations. The voltage is expressed in percent of the rated phase-to-ground voltage of the system. As shown, thanks to the proposed control strategy, SSR mitigation is achieved by injecting only 0.8% of the rated voltage. Furthermore, Fig.7.25 shows the harmonic content of the voltage injected by the SSSC at the beginning of the mitigation operations. It can be observed that, beside the frequency component at the complementary of the triggered mode shape ($60 - 24.6 = 35.4$ Hz), the injected voltage is characterized by other three frequencies: one at 84.6 Hz (corresponding to the supersynchronous component) and two frequency components located at the sidebands of the fundamental, due to the rotor swing.

The obtained simulation confirm that, with the proposed approach, SSR mitigation can be achieved with very low voltage injection, leading to a reduced voltage rating for the SSSC. Unfortunately, the author was unable to find information in the literature regarding the size of the SSSC when classical control is used. For this reason, this information is lacking in this thesis. The author has implemented the controller described in [54, 59] and the voltage needed to mitigate the same phenomenon was equal to 0.11 pu, corresponding to an oversize of 13.75 pu as compared with the approach here proposed.

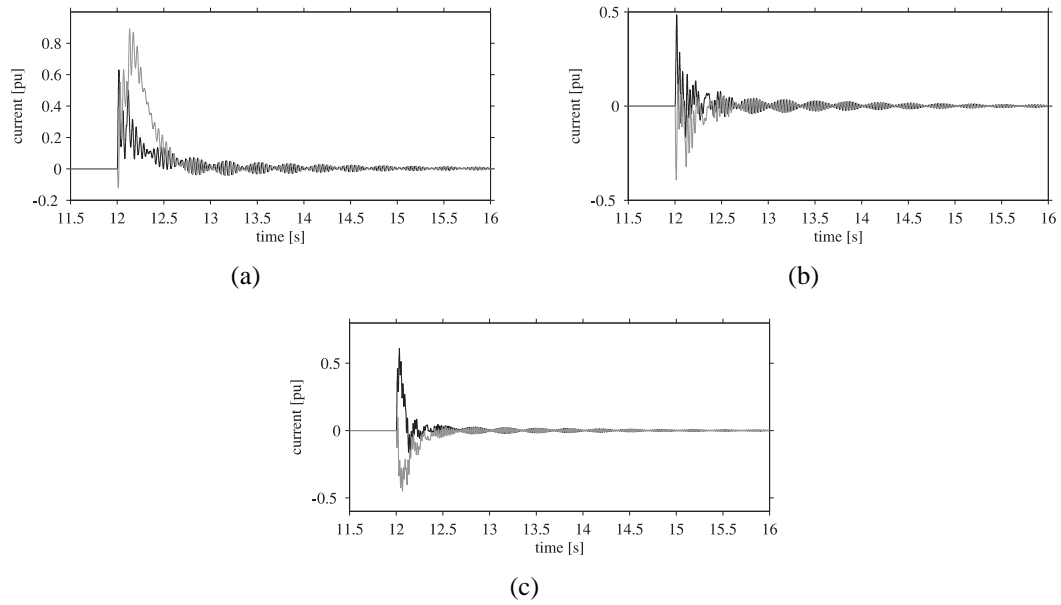


Fig. 7.20 Estimated subsynchronous components of measured line current in corresponding subsynchronous reference planes. Plot a: $\omega_{m1} = 154.88$ Hz; Plot b: $\omega_{m2} = 203.51$ Hz; Plot c: $\omega_{m3} = 321.07$ Hz. Black curve: d_m component; gray curve: q_m component.

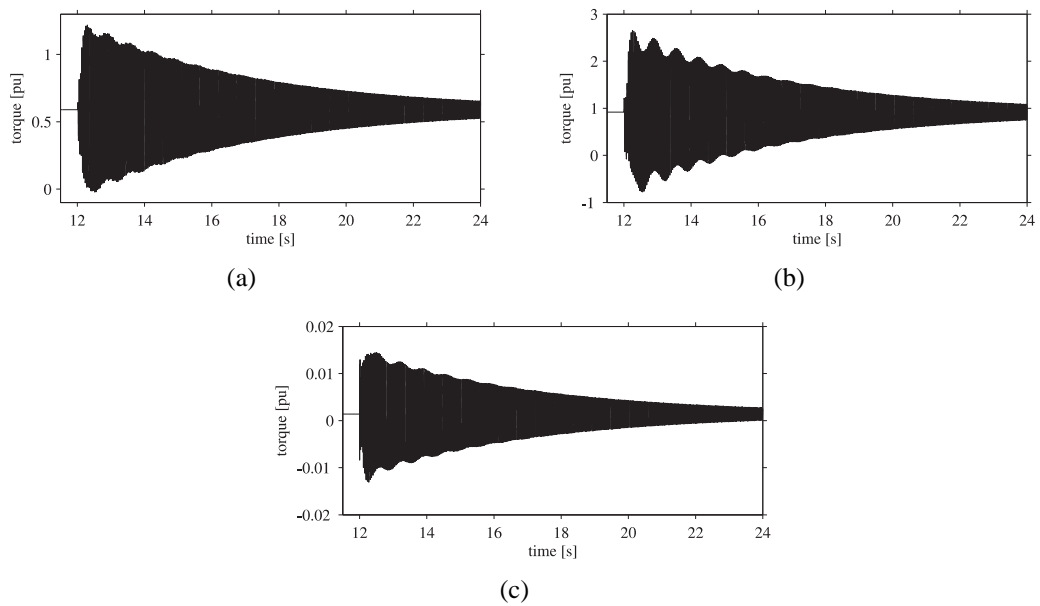


Figure 7.21: Simulated generator shaft torques for IEEE SBM. SSSC online. Plot a: HP-LP torque; Plot b: LP-GEN torque; Plot c: GEN-EX torque.

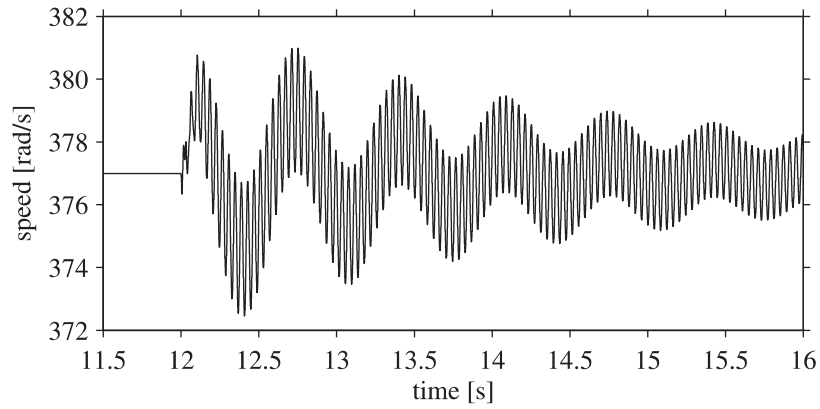


Fig. 7.22 Simulated rotor shaft speed during SSR mitigation operation.

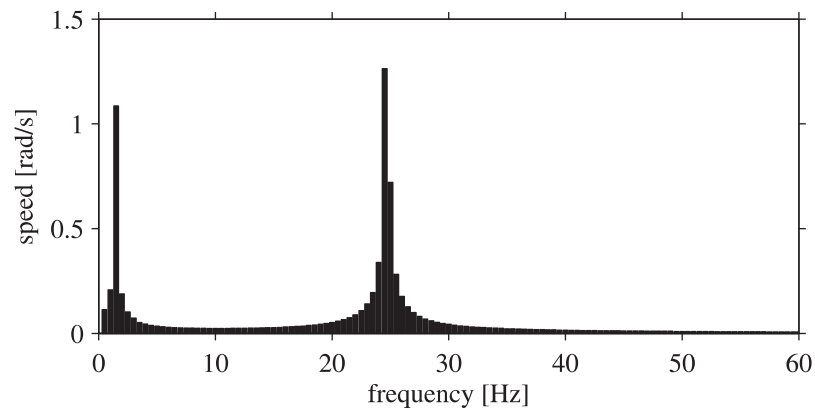


Fig. 7.23 Harmonic content of rotor speed at beginning of mitigation operation.

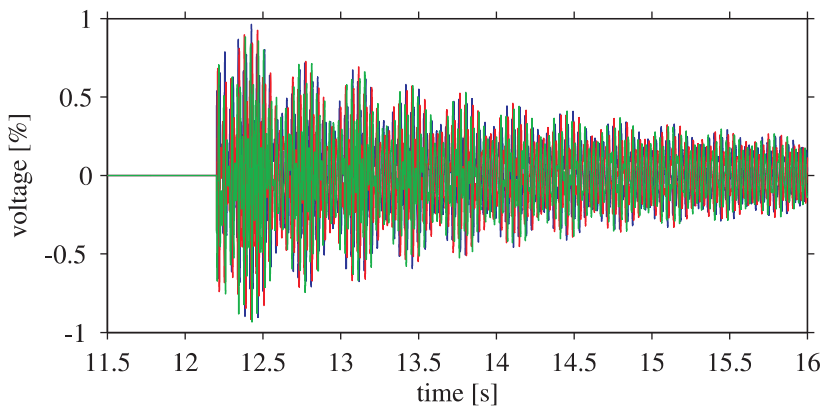


Fig. 7.24 Simulated three-phase voltage injected by SSSC during SSR mitigation operation.

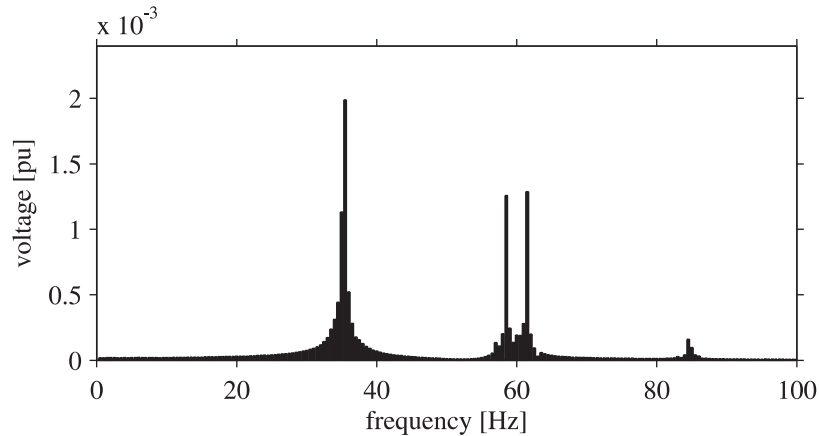


Fig. 7.25 Harmonic content of injected voltage at beginning of mitigation operation.

7.11 Conclusions

This chapter has dealt with the control of the Static Synchronous Series Compensator (SSSC) for SSR mitigation. First, the control strategy proposed in the literature has been described. Thus, a novel control strategy for an SSSC dedicated to SSR mitigation has been introduced. Based on a current controller implemented in the subsynchronous reference frame, SSR mitigation is obtained by increasing the network damping only at those frequencies that are critical for the generator shaft. To estimate the subsynchronous components of the measured voltages and currents, an estimation algorithm based on the use of low-pass filters has been derived. Stability analysis of the proposed subsynchronous controller has been carried out. Further, a control algorithm to control the dc-link voltage of the VSC has been derived.

It has been shown both through eigenvalue and frequency scanning analysis that the proposed control strategy can be successfully adopted to avoid the risk of SSR due to torsional interaction effect. Furthermore, the effectiveness of the proposed controller to mitigate SSR due to torque amplification effect has been proved through time-domain simulations by using the program PSCAD/EMTDC. A first important result is that, with the proposed configuration, the control system is robust and does not depend on the configuration of the transmission system. Furthermore, it has been shown that SSR mitigation can be achieved by injecting low amount of voltage in the grid, leading to a reduced power rating for the SSSC.

Chapter 7. Control of Static Synchronous Series Compensator for SSR Mitigation

Chapter 8

Conclusions and Future Work

This chapter summarizes conclusions and provides some suggestions for further research related to the different topics considered in this thesis.

8.1 Conclusions

This thesis has dealt with control of Voltage Source Converters (VSCs) for distribution and transmission systems applications.

In particular, the first part of the thesis has dealt with mitigation of voltage dips by using a VSC connected in series and in shunt with the grid. In both configurations, one important issue is to have a fast-response, high-performance control system that is robust to voltage disturbances. In both configurations, the core of the control system is the current controller. In Chapter 3, the deadbeat current controller for shunt-connected VSC has been investigated. With a constant dc-link voltage, the dynamic performance of the system has been tested under balanced and unbalanced conditions of the grid voltage, both in steady-state and during transients (voltage dips). It has been demonstrated that, using a vector current-controller designed by only considering positive-sequence components (VCC1), the dq -currents under unbalanced grid voltage are affected by an oscillation at double the power frequency. By feeding the same controller only the positive-sequence component of the grid voltage (VCC2), the response is improved and the actual current tracks the reference current with almost no delay. The dual vector current-controller (DVCC), where both voltages and currents are separated into their sequence components and two separate current controllers are used, shows a slower response compared with VCC2, due to the delay introduced by the sequence separation. It is important to stress that these results are valid for any application of shunt-connected VSC where a robust response to voltage disturbances is required. This can be the case of VSC used as active front-end in drive systems, variable-speed wind power and VSC-based HVDC.

A high-performance current controller is also the base of the cascade controller for the series-connected VSC (or Static Series Compensator, SSC), which has been presented in Chapter 4. The current controller is combined with an outer voltage controller loop. An extended analysis

Chapter 8. Conclusions and Future Work

of the control system and of the interaction between the inner controller and the outer controller has been carried out. It has been demonstrated through experimental results that using dual vector-controller type 1 (DVC1), designed by only considering the positive-sequence components of the measured signals, the SSC mitigates three-phase voltage dips, but not unbalanced voltage dips. To achieve a proper mitigation also in case of unbalanced voltage dips, the Positive Negative DVC (PN-DVC), based on two separate cascade controllers for the positive and the negative sequence components, has been presented. It has been demonstrated that PN-DVC presents good performance when mitigating balanced and unbalanced voltage dips. Due to the inherited time delay introduced by the sequence detection algorithm, the PN-DVC has slower response as compared with DVC1, but it ensures a perfect mitigation of the voltage dip, regardless the percentage of unbalance of the dip.

The performance of the shunt-connected VSC when used to mitigate voltage dips has been investigated in Chapter 5. It has been shown that successful restoration of the amplitude of the voltage at PCC can be achieved. However, the phase angle of the grid voltage at PCC is affected by a phase deviation during mitigation. To obtain a robust high-performance controller, insensitive to grid and load impedance variations, a modified configuration of shunt-connected VSC with LCL-filter has been proposed. The transient performance of the modified system, with the same cascade controller derived in Chapter 4 for the SSC, has been tested under balanced and unbalanced voltage dips. It has been shown that, to overcome undesired resonances between the filter components, an active damping term in the inner current controller must be added. With this modification, satisfactory mitigation of voltage dips can be achieved. However, depending on the short-circuit power of the grid at the PCC, the VSC may have to be designed to handle injection of high amount of reactive power.

The second part of this thesis has dealt with the control of the Static Synchronous Series Compensator (SSSC) for mitigation of Subsynchronous Resonances (SSR) in transmission systems. As first, Chapter 6 gave an overview of the problem of SSR in power systems. To describe the origin of SSR due to Torsional Interaction effect (TI), a linearized model of a synchronous generator connected to a radial series-compensated transmission line has been derived. Thus, a simplified model of the synchronous generator for SSR studies has been considered.

In Chapter 7, a novel control strategy for the SSSC for SSR mitigation has been introduced. Based on a current controller implemented in a reference frame that rotates synchronously with the subsynchronous voltage vector (subsynchronous reference frame), SSR mitigation is obtained by increasing the network damping only at those frequencies that are critical for the generator shaft. To estimate the subsynchronous components of the measured voltages and currents, an estimation algorithm based on the use of low-pass filters has been derived. Stability analysis of the proposed subsynchronous controller has been carried out. It has been shown both through eigenvalue and frequency scanning analysis that the proposed control strategy can be successfully adopted to avoid the risk of SSR due to torsional interaction effect. Furthermore, the effectiveness of the proposed controller to mitigate SSR due to torque amplification effect has been proved through time-domain simulation of the dynamical system. In particular, it has been shown that, by injecting a subsynchronous voltage only, SSR mitigation can be achieved by injecting only subsynchronous voltage into the power system, leading to a reduced power rating for the SSSC.

8.2 Future work

The current control algorithms presented in the first part of this thesis are very general and can be applied in different applications of VSC connected to the grid. However, they have been developed and tested with a stiff voltage source connected to the dc link of the VSC. Alternatively, a capacitor can be connected to the dc link and the controller must include regulation of the voltage across the dc-link capacitor. This limits the range of active power control. An energy storage device can be connected to the dc link. Possible solutions for storage are capacitors, super-capacitors, fuel cells and batteries. A requirement is that the energy storage device must be able to deliver a high amount of power quickly. It is not clear at this point which, among all possible solutions, represents the most suitable choice for the investigated application.

It has been shown that the shunt-connected VSC can be an interesting alternative to the problem of voltage dips mitigation. Unlike the SSC, this configuration allows mitigation of both voltage dips and short interruptions, given that a sufficient energy storage system is mounted on the dc side of the VSC. Furthermore, the shunt-connected VSC does not require a complicated protection system as the SSC. However, it was pointed out that a drawback of using a shunt-connected VSC for voltage dip mitigation is that the current to be injected into the grid may be too high if the grid is strong. An interesting solution, in this case, is to connect an inductor between the PCC and the supply in order to weaken the grid, thus, reducing the power needed during mitigation operations.

In the second part of the thesis, it has been proven that SSR mitigation can be achieved by injecting a subsynchronous voltage of appropriate amplitude and phase into the grid. The analysis carried out in the thesis is promising, but more investigation should be made in order to find the limits of the proposed approach. More complex systems, such as the CORPALS Benchmark model [4] can be simulated. Furthermore, it can be of interest to investigate the system behavior when the SSSC is installed not directly after the step-up transformer of the generator but further into the power system, in particular if more than one transmission line is fed by the power station. Finally, an economical investigation of the proposed solution should be carried out.

Chapter 8. Conclusions and Future Work

References

- [1] K. Ahlgren, D. Holmberg, P. Halvarsson, and L. Ängquist, “Thyristor controlled series capacitor used as a means to reduce torsional interaction subsynchronous resonance,” in *Proc. of Cigré SC14 Colloquium on HVDC and FACTS in South Africa*, 1997.
- [2] H. Akagi, “Trends in active power line conditioner,” *IEEE Trans. on Power Electron.*, vol. 9, no. 3, pp. 263–268, May 1994.
- [3] M. Alaküla, *Power Electronic Control*. Lund, Sweden: Lund University, 2002.
- [4] P. M. Anderson, B. L. Agrawal, and J. E. V. Ness, *Subsynchronous resonance in Power Systems*. New York, United States of America: IEEE Press, 1989.
- [5] P. M. Anderson and R. Farmer, *Series Compensation of Power Systems*. United States of America: PBLSH! Inc., 1996.
- [6] A. Arulampalam, J. B. Ekanayake, and N. Jenkins, “Application study of a STATCOM with energy storage,” in *Proc. of IEE Generation, Transmission and Distribution Conference*, vol. 150, May 2003, pp. 373–384.
- [7] T. M. L. Assis, E. H. Watanabe, L. A. S. Pilotto, and R. B. Sollero, “A new technique to control reactive power oscillations using STATCOM,” in *Proc. of 10th International Conference on Harmonics and Quality of Power*, vol. 2, October 2002, pp. 607 – 613.
- [8] H. Awad, J. Svensson, and M. H. J. Bollen, “Mitigation of unbalanced voltage dips using static series compensator,” *IEEE Trans. on Power Electron.*, vol. 9, no. 3, pp. 837–846, May 2004.
- [9] H. Awad, “Control of static series compensator for mitigation of power quality problems,” Ph.D. dissertation, Chalmers University of Technology, Göteborg, Sweden, April 2004.
- [10] V. Blasko and V. Kaura, “A new mathematical model and control of a three-phase AC-DC voltage source converter,” *IEEE Trans. on Power Electron.*, vol. 12, no. 1, pp. 116–123, January 1997.
- [11] —, “A novel control to actively damp resonance in input LC filter of a three-phase voltage source converter,” *IEEE Trans. on Ind. Appl.*, vol. 3, no. 2, pp. 542–550, March-April 1997.

References

- [12] M. H. J. Bollen, *Understanding Power Quality problems: voltage sags and interruptions*. New York: IEEE Press, 1999.
- [13] ———, “Voltage, power and current ratings of series voltage controllers,” in *Proc. of IEEE Power Engineering Society Winter Meeting*, vol. 33, no. 2, March-April 2000, pp. 1132–1137.
- [14] M. Bongiorno, “Control of voltage source converters for voltage dip mitigation in shunt and series configurations,” Chalmers University of Technology, Göteborg, Sweden, Licentiate Thesis TR-515L, December 2004.
- [15] A. Campbell and R. McHattie, “Backfilling the sinewave. a Dynamic Voltage Restorer case study,” *Power Engineering Journal*, vol. 13, no. 3, pp. 153–158, June 1999.
- [16] J. W. Choi and S. K. Sul, “Fast current controller in three-phase AC/DC boost converter using d-q axis crosscoupling,” *IEEE Trans. on Power Electron.*, vol. 13, no. 1, pp. 179–185, January 1998.
- [17] S.-K. Chung, “A phase tracking system for three phase utility interface inverters,” *IEEE Trans. on Power Electron.*, vol. 15, no. 3, pp. 431–438, May 2000.
- [18] E. R. Collins and M. A. Bridgwood, “The impact of power system disturbances on AC-coil contactors,” *IEEE Annual Technical Conference on Textile, Fiber, and Film Industry*, May 1997.
- [19] E. R. Collins and A. Mansoor, “Effects of voltage sags on AC motor drives,” *IEEE Annual Technical Conference on Textile, Fiber, and Film Industry*, May 1997.
- [20] P. Daehler and R. Affolter, “Requirements and solutions for Dynamic Voltage Restorer, a case study,” in *Proc. of IEEE Power Engineering Society Winter Meeting*, vol. 4, 2000, pp. 2881–2885.
- [21] T. Davis, G. E. Beam, and C. J. Melhorn, “Voltage sags: their impact on the utility and industrial customers,” *IEEE Trans. on Ind. Appl.*, vol. 34, no. 3, pp. 549–558, May-June 1998.
- [22] R. G. Farmer, A. L. Schwalb, and E. Katz, “Navajo project report on subsynchronous resonance: analysis and solution,” *IEEE Trans.*, vol. PAS-96, no. 1, pp. 1226–1232, 1977.
- [23] IEEE SSR Task Force, “First benchmark model for computer simulation of subsynchronous resonance,” *IEEE Trans. on Power App. Syst.*, vol. PAS-96, no. 5, pp. 1565–1571, Sept./Oct. 1977.
- [24] ———, “Second benchmark model for computer simulation of subsynchronous resonance,” *IEEE Trans. on Power App. Syst.*, vol. PAS-104, no. 5, pp. 1057–1066, 1985.
- [25] IEEE SSR Working Group, “Terms, definitions and symbols for subsynchronous oscillations,” *IEEE Trans.*, vol. PAS-104, June 1985.

- [26] R. Grunbaum, "SVC Light: a powerful means for dynamic voltage and power quality control in industry and distribution," in *Proc. of 8th International Conference on Power Electronics and Variable Speed Drives*, vol. 1, Sept. 2000, pp. 404 – 409.
- [27] M. C. Hall and D. A. Hodges, "Experience with 500-kV Subsynchronous Resonance and Resulting Turbine Generator Shaft Damage at Mohave Generating Station," *IEEE PES Special Publication, Analysis and Control of Subsynchronous Resonance, IEEE Publication 76 CH 1066-0-PWR*, pp. 22–29, 1976.
- [28] L. Harnefors, *Control of Variable-Speed Drives*. Västerås, Sweden: Applied Signal Processing and Control, Dept. of Electronics, Mälardalen University College, 2002.
- [29] L. Harnefors and H.-P. Nee, "Model-based current control of ac-drives using the internal model control method," *IEEE Trans. on Ind. Appl.*, vol. 34, no. 1, pp. 133–141, Jan. 1998.
- [30] —, "A general algorithm for speed and position estimation of ac motors," *IEEE Trans. on Ind. Electron.*, vol. 47, no. 1, pp. 77–83, Feb. 2000.
- [31] N. G. Hingorani, "Introducing custom power," *IEEE Spectrum*, vol. 32, no. 6, pp. 41–48, June 1995.
- [32] N. G. Hingorani, B. Bhargava, G. F. Garrigue, and G. D. Rodrigues, "Prototype NGH subsynchronous resonance damping scheme. Part I - field installation and operating experience," *IEEE Trans. on Power Syst.*, vol. PWRS-2, no. 4, pp. 1034–1039, 1987.
- [33] N. G. Hingorani and L. Gyugyi, *Understanding FACTS. Concepts and technology of Flexible AC Transmission Systems*. New York: IEEE Press, 2000.
- [34] J. Holtz, "Pulsewidth modulation for electronic power conversion," in *Proc. of IEEE*, vol. 82, no. 8, August 1994, pp. 1194 – 1214.
- [35] *IEEE Recommended Practice for Monitoring Electric Power Quality*, IEEE Std.1159-1995, New York, IEEE, 1995.
- [36] *IEEE Recommended Practice for Evaluating Power System Compatibility with Electronic Process Equipment*, IEEE Std.1346-1998, New York, IEEE, 1998.
- [37] F. A. Rahaman Al Jowder and B.-T. Ooi, "Series compensation of radial power systems by a combination of SSSC and dielectric capacitors," *IEEE Trans. on Power Del.*, vol. 20, no. 1, pp. 458–465, Jan. 2005.
- [38] E. Katz, J. Tang, C. E. J. Bowler, B. L. Agrawal, R. G. Farmer, J. A. Demcko, D. A. Selin, C. Cruz, and J. Sims, "Comparison of SSR calculations and test results," *IEEE Trans. on Power Syst.*, vol. 4, no. 1, pp. 336–344, Feb. 1977.
- [39] P. Kundur, *Power Systems Stability and Control*. United States of America: MacGraw-Hill, Inc, 1993.

References

- [40] T. N. Le, “Kompensation schnell veränderlicher Blindströme eines Drehstromverbrauchers (in German),” *etzArchiv, Bd. 11*, vol. H. 8, pp. 249–253, 1989.
- [41] M. Lindgren, “Modeling and control of voltage source converters connected to the grid,” Ph.D. dissertation, Chalmers University of Technology, Göteborg, Sweden, November 1998.
- [42] M. Liserre, F. Blaabjerg, and S. Hansen, “Design and control of an LCL-filter based three-phase active rectifier,” in *Proc. of 36th IEEE IAS Annual Meeting*, vol. 1, September 2001, pp. 299 – 307.
- [43] M. Liserre, R. Teodorescu, and F. Blaabjerg, “Control for three-phase grid converter systems with the use of PI-RES current controller in a rotating frame,” *IEEE Trans. on Power Electron.*, vol. 21, no. 3, pp. 836–841, May 2006.
- [44] J. Luomi, *Transient Phenomena in electrical Machines*. Göteborg, Sweden: Dept. of Electric Power Engineering, Chalmers University of Technology, 1998.
- [45] M. McGranaghan and B. Roettger, “Economic evaluation of power quality,” *IEEE Power Engineering Review*, vol. 22, no. 2, pp. 8–12, February 2002.
- [46] M. F. McGranaghan, D. R. Mueller, and M. J. Samotyj, “Voltage sags in industrial systems,” *IEEE Trans. on Ind. Appl.*, vol. 29, no. 2, pp. 397–403, March-April 1993.
- [47] N. Mohan, T. Undeland, and W. Robbins, *Power Electronics*. Canada: John Wiley and Sons, Inc., 1995.
- [48] M. J. Newman and D. G. Holmes, “An integrated approach for the protection of series injection inverters,” *IEEE Trans. on Ind. Appl.*, vol. 38, no. 3, pp. 679–687, May-June 2002.
- [49] L. Ängquist, “Synchronous voltage reversal control of thyristor controlled series capacitor,” Ph.D. dissertation, Royal Institute of Technology, Department of Electrical Engineering, Stockholm, Sweden, September 2002.
- [50] J. D. Nielsen, “Design and control of a Dynamic Voltage Restorer,” Ph.D. dissertation, Aalborg University, Denmark, March 2002.
- [51] R. Ottersten and J. Svensson, “Vector current controlled voltage source converter - dead-beat control and saturation strategies,” *IEEE Trans. on Power Electron.*, vol. 17, no. 2, pp. 279–285, March 2002.
- [52] R. Ottersten, “On control of back-to-back converters and sensorless induction machine drives,” Ph.D. dissertation, Chalmers University of Technology, Göteborg, Sweden, June 2003.
- [53] K. R. Padiyar, *Analysis of Subsynchronous Resonance in Power systems*. United States of America: Kluwer Academic Publishers, 1999.

- [54] K. R. Padiyar and N. Prabhu, "Analysis of subsynchronous resonance with three level twelve-pulse VSC based SSSC," in *Proc. of Conference on Convergent Technologies for Asia-Pacific Region (TENCON), 2003*, vol. 1, Oct. 2003, pp. 76–80.
- [55] ———, "Design and performance evaluation of subsynchronous damping controller with STATCOM," *IEEE Trans. on Power Del.*, vol. 21, no. 3, pp. 1398–1405, July 2006.
- [56] K. Padiyar and R. Varma, "Damping torque analysis of static VAR system controllers," *IEEE Trans. on Power Syst.*, vol. 6, no. 2, pp. 458–465, May 1991.
- [57] Z. J. Palmor, *The Control Handbook*. Orlando: FL: CRC Press, 1996.
- [58] A. Petersson, L. Harnefors, and T. Thiringer, "Evaluation of current control methods for wind turbines using doubly-fed induction machines," *IEEE Trans. on Power Electron.*, vol. 20, no. 1, pp. 227–235, Jan. 2005.
- [59] G. N. Pillai, A. Ghosh, and A. Joshi, "Robust control of SSSC to improve torsional damping," in *Proc. of 38th IEEE Power Engineering Society Winter Meeting, 2001*, vol. 3, Jan. 2001, pp. 1115–1120.
- [60] T. Raimondi, *Principi di controllori automatici* (in Italian). Palermo, Italy: Scientific books, 1997.
- [61] A. Sannino, "Static transfer switch: analysis of switching conditions and actual transfer time," in *Proc. of IEEE Power Engineering Society Winter Meeting*, vol. 1, January 2001, pp. 120–125.
- [62] A. Sannino, M. H. J. Bollen, and J. Svensson, "Voltage tolerance testing of three-phase voltage source converters," *IEEE Trans. on Power Del.*, vol. 20, no. 2, pp. 1633–1639, April 2005.
- [63] A. Sannino, M. Ghans-Miller, and M. H. J. Bollen, "Overview of voltage sag mitigation techniques," in *Proc. of IEEE Power Engineering Society Winter Meeting*, vol. 4, January 2000, pp. 23–27.
- [64] A. Sannino, "Application of power-electronic devices for improving power quality in industrial systems," Ph.D. dissertation, University of Palermo, Italy, December 2000.
- [65] K. K. Sen, "SSC - Static Series Compensator: theory, modeling and applications," *IEEE Trans. on Power Del.*, vol. 13, no. 1, pp. 241–246, Jan. 1998.
- [66] Y. H. Song and A. T. Johns, *Flexible AC Transmission Systems (FACTS)*. London: The Institution of Electrical Engineers, 1999.
- [67] M. Steurer and S. Eckroad, "Voltage control performance enhancement by adding energy storage to shunt connected voltage source converters," in *Proc. of 10th International Conference on Harmonics and Quality of Power*, vol. 2, October 2002, pp. 590 – 594.

References

- [68] K. J. Åström and T. Hägglund, *PID Controllers, 2nd Edition*. United States of America: Instrument Society of America, 1994.
- [69] K. J. Åström and B. Wittenmark, *Computer Controlled System: Theory and Design, 3rd Edition*. United States of America: Prentice-Hall, Inc., Englewood Cliffs, 1996.
- [70] J. Sun, D. Czarkowski, and Z. Zabar, “Voltage flicker mitigation using PWM-based distribution STATCOM,” in *Proc. of IEEE Power Engineering Society Summer Meeting*, vol. 1, July 2002, pp. 616–621.
- [71] J. Svensson, “Inclusion of dead-time and parameter variations in VSC modeling for predicting responses of grid voltage harmonics,” in *Proc. of 7th European Conf. Power Electronics and Applications (EPE’97)*, vol. 3, September 1997, pp. 216 – 221.
- [72] ———, “Grid-connected voltage source converter - control principles and wind energy applications,” Ph.D. dissertation, Chalmers University of Technology, Göteborg, Sweden, March 1998.
- [73] P. C. Tan, R. E. Morrison, and D. G. Holmes, “Voltage form factor control and reactive power compensation in a 25-kV electrified railway system using a shunt active filter based on voltage detection,” *IEEE Trans. on Ind. Appl.*, vol. 39, no. 2, pp. 575–581, March-April 2003.
- [74] N. S. Tunaboylu, E. R. Collins, S. W. Middlekauff, and R. L. Morgan, “Ride-through issues for DC motor drives during voltage sags,” in *Proc. of IEEE Southeastcon ’95, Visualize the Future*, 1995, pp. 52 – 58.
- [75] E. Twining and D. G. Holmes, “Voltage compensation in weak distribution networks using multiple shunt connected voltage source inverters,” in *Proc. of IEEE Bologna PowerTech Conference*, vol. 4, June 2003, pp. 619 – 626.
- [76] E. Twining, M. J. Newman, P. C. Loh, and D. G. Holmes, “Voltage compensation in weak distribution networks using a D-STATCOM,” in *Proc. of 5th IEEE PEDS International Conference*, vol. 1, Nov. 2003, pp. 178 – 183.
- [77] S. M. Woo, D. W. Kang, W. C. Lee, and D. S. Hyun, “The distribution STATCOM for reducing the effect of voltage sag and swell,” in *Proc. of 27th Annual Conference of the IEEE Industrial Electronics Society*, vol. 2, December 2001, pp. 1132–1137.
- [78] N. Woodley, “Power electronics implementation of custom power applications,” *Panel Session on Custom Power Applications for Power Quality Improvement, IEEE PES Transmission and Distribution Conference and Exposition*, April 1999.
- [79] ———, “Field experience with Dynamic Voltage Restorer (DVR) systems,” in *Proc. of IEEE Power Engineering Society Winter Meeting*, vol. 4, 2000, pp. 2864 – 2871.
- [80] N. Woodley, L. Morgan, and A. Sundaram, “Experience with an inverter-based Dynamic Voltage Restorer,” *IEEE Trans. on Power Del.*, vol. 14, no. 3, pp. 1181–1184, July 1999.

References

- [81] L. D. Zhang and M. H. J. Bollen, "A method for characterizing unbalanced voltage dips (sags) with symmetrical components," *IEEE Power Engineering Review*, vol. 18, no. 7, pp. 50–52, July 1998.
- [82] —, "Characteristic of voltage dips (sags) in power systems," *IEEE Trans. on Power Del.*, vol. 15, no. 2, pp. 827–832, April 2000.

References

Appendix A

Transformations for Three-phase Systems

This appendix reports necessary transformations to calculate voltage vectors from three-phase quantities and vice versa. Expressions of the voltage vector both in the fixed and rotating reference frames are given in the general case of unsymmetrical three-phase quantities.

A.1 Transformation of three-phase quantities into vectors

A three-phase positive system constituted by the three quantities $v_1(t)$, $v_2(t)$ and $v_3(t)$ can be transformed into a vector in a complex reference frame, usually called $\alpha\beta$ -frame, by applying the transformation defined by

$$\underline{v}(t) = v_\alpha + jv_\beta = K \left[v_1(t) + v_2 e^{j\frac{2}{3}\pi}(t) + v_3 e^{j\frac{4}{3}\pi}(t) \right] \quad (\text{A.1})$$

where the factor K is equal to $\sqrt{3/2}$ or $3/2$ to ensure power invariance or voltage invariance, respectively, between the two systems. Equation (A.1) can be expressed as a matrix equation as follows

$$\begin{bmatrix} v_\alpha(t) \\ v_\beta(t) \end{bmatrix} = \mathbf{C}_{23} \begin{bmatrix} v_1(t) \\ v_2(t) \\ v_3(t) \end{bmatrix} \quad (\text{A.2})$$

where, using power-invariant transformation, the matrix \mathbf{C}_{23} is equal to

$$\mathbf{C}_{23} = \begin{bmatrix} \sqrt{\frac{2}{3}} & -\frac{1}{\sqrt{6}} & -\frac{1}{\sqrt{6}} \\ 0 & \frac{1}{\sqrt{2}} & \frac{1}{\sqrt{2}} \end{bmatrix} \quad (\text{A.3})$$

The inverse transformation, assuming no zero-sequence, is given by

$$\begin{bmatrix} v_1(t) \\ v_2(t) \\ v_3(t) \end{bmatrix} = \mathbf{C}_{32} \begin{bmatrix} v_\alpha(t) \\ v_\beta(t) \end{bmatrix} \quad (\text{A.4})$$

where

$$\mathbf{C}_{32} = \begin{bmatrix} \sqrt{\frac{2}{3}} & 0 \\ -1 & 1 \\ \frac{\sqrt{6}}{2} & \frac{\sqrt{2}}{2} \\ -1 & -1 \\ \frac{\sqrt{6}}{2} & \frac{\sqrt{2}}{2} \end{bmatrix} \quad (\text{A.5})$$

A.2 Transformation between fixed and rotating coordinate systems

Let the vectors $\underline{v}(t)$ and $\underline{u}(t)$ rotate in the $\alpha\beta$ -frame with the angular frequency $\omega(t)$ in the positive (counter-clockwise) direction. If the vector $\underline{u}(t)$ is taken as the d -axis of a dq -frame that rotates in the same direction with the same angular frequency $\omega(t)$, both vectors will appear as fixed vectors in that frame. The components of $\underline{v}(t)$ in the dq -frame are thus given by the projections of the vector on the direction of $\underline{u}(t)$ and on the orthogonal direction, as illustrated in Fig.A.1.

The transformation can be written in vector form as

$$\underline{v}^{(dq)}(t) = \underline{v}^{(\alpha\beta)}(t)e^{-j\theta(t)} \quad (\text{A.6})$$

with the angle $\theta(t)$ in Fig.A.1 given by

$$\theta(t) = \theta_0 + \int_0^t \omega(\tau)d\tau \quad (\text{A.7})$$

The inverse transformation, from the rotating dq -frame to the fixed $\alpha\beta$ -frame is defined by

$$\underline{v}^{(\alpha\beta)}(t) = \underline{v}^{(dq)}(t)e^{j\theta(t)} \quad (\text{A.8})$$

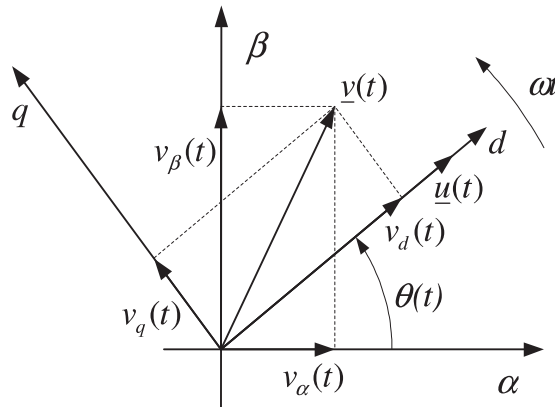


Fig. A.1 Relation between $\alpha\beta$ -frame and dq -frame.

A.3. Voltage vectors for unsymmetrical three-phase systems

The components in the dq -frame can be determined from Fig.A.1. In matrix form, the transformation from the fixed $\alpha\beta$ -frame to the dq -frame can be written as

$$\begin{bmatrix} v_d(t) \\ v_q(t) \end{bmatrix} = \mathbf{R}(-\theta(t)) \begin{bmatrix} v_\alpha(t) \\ v_\beta(t) \end{bmatrix} \quad (\text{A.9})$$

while the inverse is given by

$$\begin{bmatrix} v_\alpha(t) \\ v_\beta(t) \end{bmatrix} = \mathbf{R}(\theta(t)) \begin{bmatrix} v_d(t) \\ v_q(t) \end{bmatrix} \quad (\text{A.10})$$

where the projection matrix is

$$\mathbf{R}(\theta(t)) = \begin{bmatrix} \cos(\theta(t)) & -\sin(\theta(t)) \\ \sin(\theta(t)) & \cos(\theta(t)) \end{bmatrix} \quad (\text{A.11})$$

A.3 Voltage vectors for unsymmetrical three-phase systems

The phase voltages for a three-phase system can be written as

$$e_a(t) = \hat{e}_a(t) \cos[\omega(t) - \varphi_a] \quad (\text{A.12})$$

$$e_b(t) = \hat{e}_b(t) \cos\left[\omega(t) - \frac{2}{3}\pi - \varphi_b\right] \quad (\text{A.13})$$

$$e_c(t) = \hat{e}_c(t) \cos\left[\omega(t) - \frac{4}{3}\pi - \varphi_c\right] \quad (\text{A.14})$$

where $\hat{e}_a(t)$ and φ_a are the amplitude and the phase angle of the phase voltage $e_a(t)$, while ω is the angular frequency of the system.

If the voltage amplitude of the three phases are unequal, the resulting voltage vector $\underline{u}^{(\alpha\beta)}(t)$ in the fixed $\alpha\beta$ -coordinate system can be expressed as the sum of two vectors rotating in opposite directions and interpreted as positive- and negative-sequence component vectors

$$\underline{u}^{(\alpha\beta)}(t) = E_p e^{j(\omega t + \varphi_p)} + E_n e^{-j(\omega t + \varphi_n)} \quad (\text{A.15})$$

where E_p and E_n are the amplitudes of the positive and negative voltage vectors, respectively, and the corresponding phase angles are denoted by φ_p and φ_n .

When transforming the voltage vector $\underline{u}^{(\alpha\beta)}$ from the fixed $\alpha\beta$ -plane to the rotating dq -coordinate system, two rotating frames can be used, accordingly. These two frames are called positive and negative synchronous reference frames (SRFs) and are denoted as dqp - and dqn -plane: the positive SRF rotates counterclockwise with the angular frequency, while the negative SRF rotates clockwise with the same frequency. These two frames can be defined by the following transformations

$$\underline{u}^{(dqp)}(t) = e^{-j\theta(t)} \underline{u}^{(\alpha\beta)}(t) \quad (\text{A.16})$$

$$\underline{u}^{(dqn)}(t) = e^{j\theta(t)} \underline{u}^{(\alpha\beta)}(t) \quad (\text{A.17})$$

Chapter A. Transformations for Three-phase Systems

From the latter, it is straightforward to understand that a positive-sequence component corresponds to a DC-component (zero frequency) in the positive SRF, while a negative-sequence component corresponds to a vector that rotates with 100 Hz clockwise in the positive SRF

$$\underline{u}_n^{(dqp)}(t) = e^{-j\theta(t)} e^{-j\theta(t)} \underline{u}^{(dq\eta)}(t) = e^{j2\theta(t)} \underline{u}^{(dq\eta)}(t) \quad (\text{A.18})$$

An analogous relation can be derived for a positive-sequence component in the negative SRF.

Appendix B

Benchmark Models for SSR Studies

This appendix reports the two benchmark models introduced by the IEEE for SSR studies. The first model deals with SSR due to radial resonance in the power systems, while the second model deals with parallel resonance.

B.1 IEEE First Benchmark Model (FBM)

The IEEE First Benchmark Model (FBM, depicted in Fig.B.1) deals with SSR due to radial resonance and consists of a 892.4 MVA turbine generator connected to a single-line, series-compensated transmission network [23]. The rated voltage of the system is 539 kV, while the rated frequency is 60 Hz. Parameters for the transmission line and for the synchronous machine are reported in Tables B.1 and B.2, respectively. Parameters for the generator-shaft model are reported in Table B.3.

B.2 IEEE Second Benchmark Model (SBM)

Figure B.2 shows the single-line diagram of the IEEE Second Benchmark Model (SBM) [24]. As a difference compared with the IEEE FBM, the IEEE SBM deals with the parallel resonance

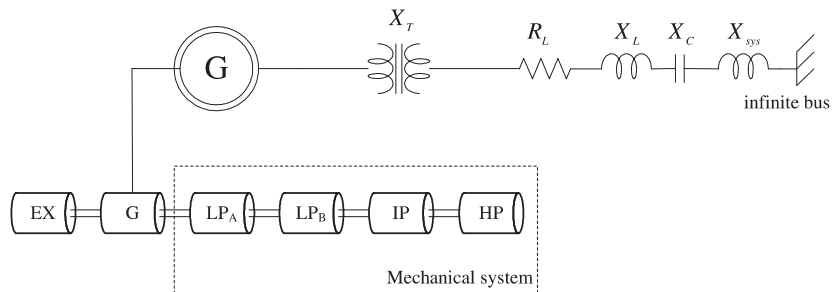


Fig. B.1 Single-line diagram of IEEE FBM.

TABLE B.1: IEEE FBM Network Parameters.

Network resistance	R_L	0.02 pu
Transformer reactance	X_T	0.14 pu
Transformer ratio		26/539 kV
Line reactance	X_L	0.50 pu
Downstream system reactance	X_{sys}	0.06 pu

TABLE B.2: IEEE FBM Synchronous Machine Parameters.

Reactance	Value [pu]	Time constant	Value [sec]
$X_{a\sigma}$	0.13	T'_{d0}	4.3
X_d	1.79	T''_{d0}	0.032
X'_d	0.169	T'_{q0}	0.85
X''_d	0.135	T''_{q0}	0.05
X_q	1.71		
X'_q	0.228		
X''_q	0.2		

problem. In this model, a 600 MVA turbine generator is connected to two parallel connected transmission lines, one of which is series compensated. The rated frequency of the system is 60 Hz. The parameters of the two transmission lines are given on a 100 MVA power base and 500 kV voltage base and are reported in Table B.4. The reactances and time constants of the generator are given in Table B.5. Finally, parameters for the generator-shaft model are reported in Table B.6.

TABLE B.3: IEEE FBM Shaft Parameters.

Mass	Inertia	Shaft section	Spring constant
	H [s ⁻¹]		K [pu T/rad]
HP turbine	0.092897	HP-IP	19.303
IP turbine	0.155589	IP-LPA	34.929
LPA turbine	0.858670	LPA-LPB	52.038
LPB turbine	0.884215	LPB-GEN	70.858
Generator	0.868495	GEN-EX	2.82
Exciter	0.0342165		

B.2. IEEE Second Benchmark Model (SBM)

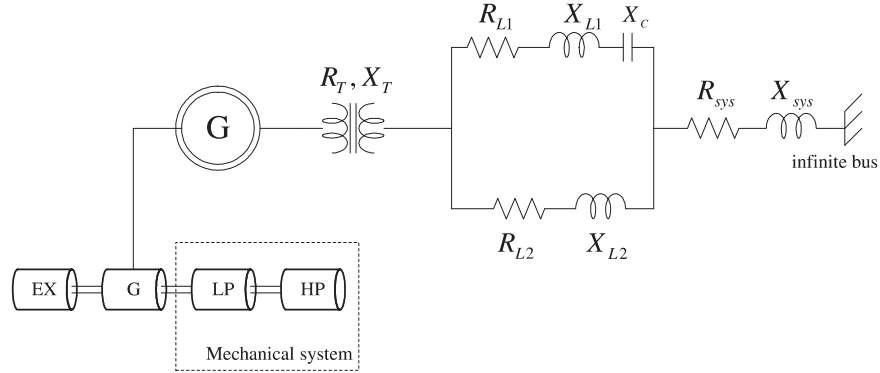


Fig. B.2 Single-line diagram of IEEE SBM.

TABLE B.4: IEEE SBM Network Parameters in per unit based on 100 MVA and 500 kV.

Transformer resistance	R_T	0.0002 pu
Transformer reactance	X_T	0.02 pu
Transformer ratio		22/500 kV
Line 1 resistance	R_{L1}	0.0074 pu
Line 1 reactance	X_{L1}	0.08 pu
Line 2 resistance	R_{L2}	0.0067 pu
Line 2 reactance	X_{L2}	0.0739 pu
Downstream system resistance	R_{sys}	0.0014 pu
Downstream system reactance	X_{sys}	0.03 pu

TABLE B.5: IEEE SBM Synchronous Machine Parameters in per unit based on 600 MVA and 22 kV.

Reactance	Value [pu]	Time constant	Value [sec]
$R_{a\sigma}$	0.0045	T'_{d0}	4.5
$X_{a\sigma}$	0.14	T''_{d0}	0.04
X_d	1.65	T'_{q0}	0.55
X'_d	0.25	T''_{q0}	0.09
X''_d	0.2		
X_q	1.59		
X'_q	0.46		
X''_q	0.2		

TABLE B.6: IEEE SBM Shaft Parameters.

Mass	Inertia		Damping	Shaft section	Spring constant
	H [lbm-ft ²]	D [lbf-ft-sec/rad]			
HP turbine	49912	155.2	HP-LP	$50.12 \cdot 10^6$	
LP turbine	310729	966.2	LP-GEN	$97.97 \cdot 10^6$	
Generator	176204	547.9	GEN-EX	$4.39 \cdot 10^6$	
Exciter	1383	4.3			

Appendix C

Selected Publications

Paper I

J. Svensson, M. Bongiorno and A. Sannino, "Practical Implementation of Delayed Signal Cancellation Method for Phase Sequence Separation," *IEEE Transactions on Power Delivery*, vol. 22, no. 1, pp. 18-26, Jan. 2007.



Paper II

M. Bongiorno, J. Svensson and A. Sannino, “Effect of Sampling Frequency and Harmonics on Delay-based Phase-sequence Estimation Method,” submitted to *IEEE Transactions on Power Delivery*.



Paper III

M. Bongiorno, J. Svensson and A. Sannino, "Dynamic Performance of Current Controllers for Grid-connected Voltage Source Converter Under Unbalanced Voltage Conditions," in *Proc. of IEEE Nordic Workshop on Power and Industrial Electronics (NorPIE'04)*.



Paper IV

M. Bongiorno, J. Svensson and A. Sannino, "Dynamic Performance of Vector Current Controllers for Grid-connected VSC under Voltage Dips," in *Proc. of 40th Annual IEEE Industry Applications Conference (IAS'05)*, vol. 2, Oct. 2005, pp. 904-909.



Paper V

M. Bongiorno, J. Svensson and A. Sannino, “An Advanced Cascade Controller for Series-connected VSC for Voltage Dip Mitigation,” to appear in *IEEE Transactions on Industrial Applications*.



Paper VI

M. Bongiorno and J. Svensson, “Voltage Dip Mitigation using Shunt-connected Voltage Source Converter,” to appear in *IEEE Transactions on Power Electronics*.



Paper VII

M. Bongiorno, J. Svensson and L. Ängquist, “Online Estimation of Subsynchronous Voltage Components in Power Systems,” to appear in *IEEE Transactions on Power Delivery*.



Paper VIII

M. Bongiorno, L. Ängquist and J. Svensson, “A Novel Control Strategy for Subsynchronous Resonance Mitigation Using SSSC,” to appear in *IEEE Transactions on Power Delivery*.



Paper IX

M. Bongiorno, J. Svensson and L. Ängquist, "On Control of Static Series Compensator for SSR Mitigation," in *Proc. of 38th Annual IEEE Power Electronics Specialists Conference (IEEE PESC'07)*.



Paper X

M. Bongiorno, J. Svensson and L. Ängquist, “Single-phase VSC Based SSSC for Sub-synchronous Resonance Damping,” to appear in *IEEE Transactions on Power Delivery*.



